Geodetic monitoring of surface deformation along the western shores of the Dead Sea using GPS and InSAR observations

Uri Schattner

This work was submitted as a M. Sc. Thesis to the Department of Geophysics and Planetary Sciences, Tel-Aviv University.

The study was carried out under the supervision of:
Dr. Daniel Wachs, Geological Survey of Israel.
And Dr. Shimon Wdowinski, the Department of Geophysics and Planetary Sciences, Tel-Aviv University.

Acknowledgments

Abstract

The development of surface subsidence and collapse features (i.e. sinkhole) along the Dead Sea shores has been observed for the last 30 years. During the last decade the phenomenon has accelerated both in the size and in number. Today there are about 600 sinkholes, and few thousands of square meters of subsurface subsidences, along the western shores of the Dead Sea alone. Sinkholes are a geo-hazard that endangers life, property and prevents the development of the area. The recent development of sinkholes was observed along both the eastern and the western shores of the Dead Sea; therefore, it might have more than a circumstantial connection to the continuous lowering of the Dead Sea water level. According to recent studies, the development of local surface subsidences is caused by irreversible compaction of the subsurface matrix fine-grained layers, whereas the development of sinkholes is triggered by the existence of underground cavities created by salt dissolution. The surface deformation reflects mainly the mechanical properties of the soil at shallow depths (mostly Alluvium). Recent studies provide a rough prediction for a future sinkhole's locations and its rate of formation.

This research was carried out in two levels – regional, along the western coast of the Dead Sea (between Z'ruya and Ze'elim alluvial fans), and local, at the northern part of Hever alluvial fan. The main research objective was quantitative characterization of vertical surface displacements induced by, or related to sinkhole activity, by using three geodetic methods: Global Positioning System (GPS), Interferometric synthetic aperture radar (InSAR) and Electronic Distance Measurement (EDM). The secondary objective was to develop a technique to investigate the surface displacements by combining between the three geodetic methods, and to provide tools for future researches. The GPS is very precise surveying technique (sub-centimeter level) for measuring position changes in specific locations. Most of the field measurements were carried out using kinematic GPS: in Real Time or Post processing modes. The geodetic data was used to create elevation maps of each measurement session, and to compare elevation changes between the sessions. The InSAR technique was used for measuring surface elevation changes in a wide spatial resolution. Seventeen InSAR scenes were acquired during a period 1992-1999, which was used to create change interferograms with spanning period of 2 to 71 months. The interferograms enables characterizing surface subsidence in the regional level. The EDM measurements give the distance of the measured points relative to the instrument (horizontal, vertical and angles). It was used as a complementary method to the GPS, therefore its results had limited contribution to the research.

The results of all these geodetic techniques, field observations and air photo scanning enables us to characterize surface deformation both in local and regional levels. In the local level - During a two-year period of field measurements (GPS, EDM) in the northern Hever alluvial fan, the number of sinkholes has risen from four to seven within the studied area, and some of them expanded. Furthermore, surface subsidences developed accompanied by concentric sets of joints around the sinkholes. In the regional level - Additional locations of surface subsidence were detected in InSAR interferograms, within the area between Z'ruya and Ze'elim alluvial fans respectively. The observed surface subsidence span on vast areas (hundreds of square meters) and develop in rates of up to 4 cm per year.

Table of content

List of figures

1. Introduction

1.1 Background

During the past 30 years few hundreds surface collapses (*sinkholes*) have occurred along the western shores of the Dead-Sea. Early reports indicated development of two sinkholes in the palm plantation of kibbutz En-Gedi during the 1960s and one in the delta of Mor creek, in 1978 (Raz, 1999a). In 1989 a sinkhole was formed on highway No. 90, near Neve-Zohar (Figure 1.1). Since then the surface collapses phenomenon has accelerated dramatically (sinkholes' size and numbers) accompanied with spacious surface subsidences, especially during the past five years. By now there are about 600 sinkholes, and few thousands of square meters of surface subsidences, along the western shores of the Dead Sea. The sinkholes are a geo-hazard that endangers people, damages property and prevents programs for the area development. The main concern is for people lives, which can be at risk due to infrastructure failure. All these result in a need to investigate the phenomenon. Since 1960, the Dead Sea level had declined in an average rate of 0.5 $^{m}/_{yr}$. Between 1981 and today this rate increased to 0.8 $^{m}/_{yr}$ (Wachs, 1999). The Dead Sea water level changes between 1920 and today are shown in Figure 1.2. Sinkholes developed along both the western and the eastern shores of the Dead Sea. The recent massive development of the sinkholes and the surface subsidences might have more than a circumstantial connection to the continuous lowering of the Dead Sea level through the last 30 years.
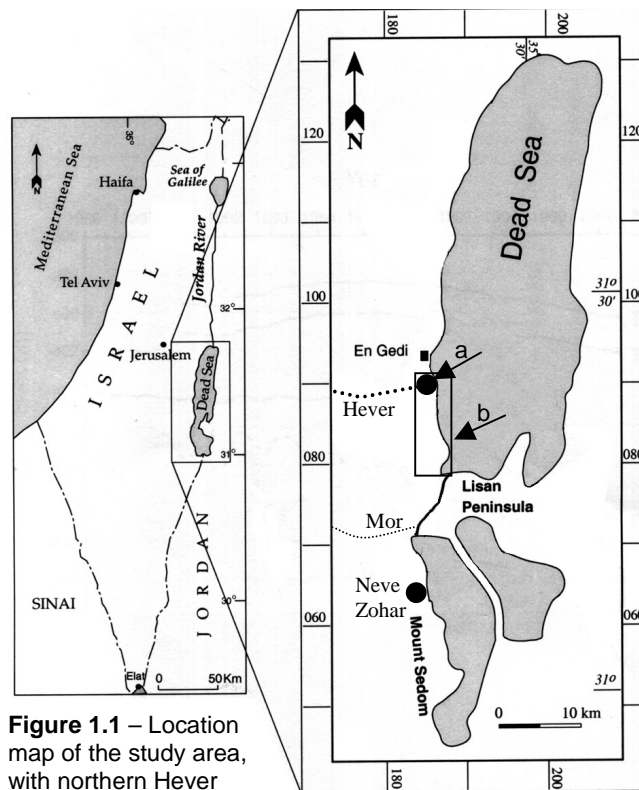
Figure 1.1 – Location map of the study area, with northern Hever sinkhole site (a), and Mezada plain (b).
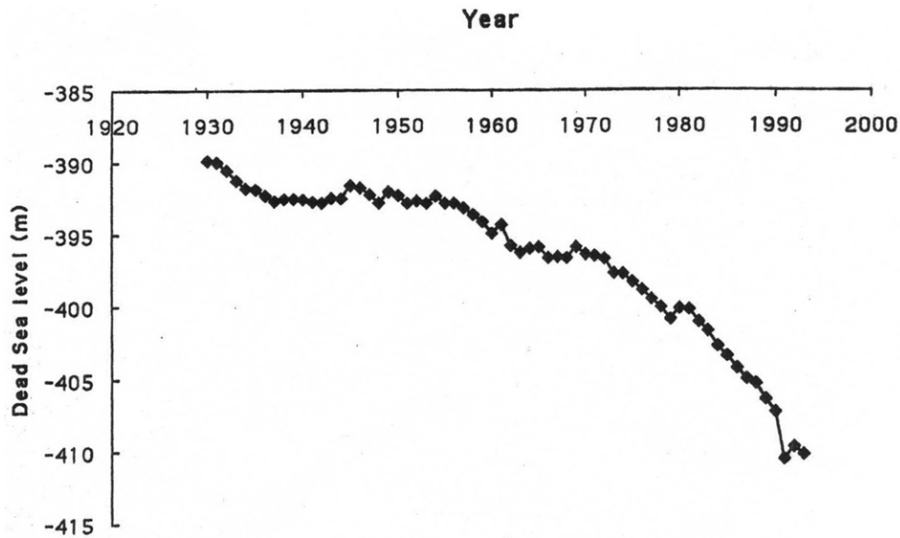
Figure 1.2 – The Dead Sea level, since the 1920' (Yechieli, 1999).

1.1.1 General description of sinkhole and surface subsidence

Sinkholes and surface subsidences are two aspects of vertical displacements of the ground that have different dimensions and different pace of development. These vertical displacements result from different processes. The term *sinkhole* (or *Doline*) describes a phenomenon that generally takes place in Karst terrain. A sinkhole is created by a sudden collapse of the ground into a subsurface cavity. The diameter of sinkholes span from sub-meter to few tens of meters (USGS, 2000). The cavity (or a group of cavities) is usually formed when a substance (e.g., Limestone, Gypsum or Salt) is dissolved at a shallow depth. The mass deficit changes the force balance of the covering soil layer and causes a gradual failure that appears at the surface as a pre-sinkhole differential subsidence with a concentric nature. The subsidence is usually bounded by concentric cracks that indicate the dimensions of the subsurface cavity and the margins of the surface failure. Each stage of the developing sinkhole is marked by cracks of bigger diameter (the subsidence diameter) with the increasing influence of the sub-surface cavity (the gradual surface failure). A complex variety of sinkhole with their bottoms at different levels, and sometimes depressions within depressions, is called *Uvala*.

There are two major sinkhole types (Figure 1.3). *Collapse Sinkhole* (Figure 1.3a) is formed by one rapid, usually single occurrence, downward movement of soil mass into the sub-surface cavity (Bögli, 1980) after the soil mass had reached its point of failure. *Solution Sinkhole* (or *solution depression*) (Figure 1.3b) is formed in a surface layer, which consists of cohesionless soil, covering a dissolvable matter that undergoes a process of cavitation. The cohesionless fine grains erode into small openings in the porous layer beneath, similarly to the flow of fine sand through the throat of a sand watch.

Pre-sinkhole subsidences, collapse sinkholes and solution sinkholes all have a circular shape at the surface. In general, the process of sinkhole formation can be divided into the two major stages: prior and after the soil failure. In the first stage, prior to the soil failure, a cavity or a beehive of voids initiates at the shallow sub-surface. The cavity mass deficit influences the surface by causing a gradual concentric sinking, which is bounded and is guided by concentric cracks. In the second stage, after the soil failure, a slow depression or a rapid collapse occurs. The

sinkhole's shape reflects the soil properties and the local sub-surface cavity dimensions.

The term *surface subsidence* describes a large-scale gradual settling of the ground. The vertical displacement of the surface subsidence span from few centimeters to few meters, whereas the subsiding area can reach thousands of square meters. Subsidences are caused by withdrawal of fluid or gas from the pores between the particles of the subsurface. As long as the pressure of the fluid (or gas) in the pores is sufficient to support the overlying sediments, no subsidence will occur at the surface. But, if fluids are withdrawn from below the surface, the fluid pressure decreases resulting in gradual subsidence at the surface. The two most important fluids that occur beneath the surface are water and petroleum (in the form of oil and natural gas) (USGS, 2000).

Subsidence can be caused by any process that results in lowering of the water table, like drought, dry seasons, and excessive pumping. Most of the subsidences occur as a result of hydrocompaction when water absorbed on and within clay minerals is removed by withdrawal or drying. Then the clays become more tightly compacted. Most hydrocompaction is a reversible elastic deformation process. Compaction, however, can become inelastic and therefore irreversible. The rate of subsidence is relative to rate of fluid withdrawal. In some cases the transition between elastic and inelastic compaction can be distinguished: normally, a large rate of fluid withdrawal accompanied with small rate of subsidence indicates elastic compaction. If, however, there is a large amount of subsidence with only small amounts of fluid withdrawal, inelastic compaction is likely occurring (Nelson, 2000).
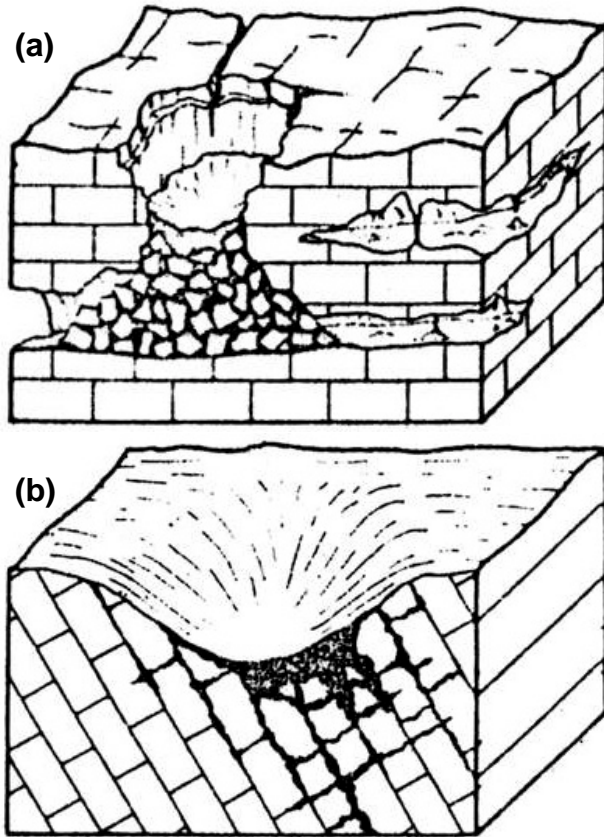
Figure 1.3 –Block diagrams showing a collapse sinkhole (a) and a solution sinkhole (b) (Ogden, 1984).

1.1.2 Geographic location.

The study area is located along the western shores of the Dead Sea, on the eastern part of Mezada plain, in a narrow strip (about 2km), sub-parallel to the recent shoreline (Figure 1.1). The strip lies south of Hever alluvial fan, and north of Ze'elim alluvial fan (Figure 1.7). The study was conducted in two scales of geodetic monitoring: (1) The whole shore strip was imaged by Synthetic Aperture Radar Interferometry, while a smaller area, (2), the northern part of Hever alluvial fan, was monitored by Global Positioning System (GPS) and Electronic Distance Measurement measurements (EDM) (marked as areas **a** and **b** on Figure 1.1, respectively).

1.1.3 Geologic and Geohydrologic background.

Tectonics - The Dead Sea is a rhomb-shaped pull-apart basin, located at the boundary between two tectonic plates: the Arabian plate and the Sinai-Israel sub-plate. The Dead Sea basin was formed between left-stepping fault strands, in a left lateral strike-slip fault system, during a late-Cenozoic breakup (Garfunkel, 1997). The Dead Sea is one of a series of intracontinental rhomb-shaped basins within the East African - Syrian rift system, and the terminal lake of the Jordan River (Niemi et al., 1997).

Sediments - The sediments in the study area (Mezada plain) are mainly composed of continental sediments of Quaternary age (Figure 1.4). The sediments are clastic (clay, sand and gravel), deposited in fan deltas, with some intercalations of lacustrine sediments (clay, gypsum and aragonite), belonging to the Lisan Formation (Sneh, 1979). In general, the sediments are of fine grain size close to the shore of the Dead Sea and in the upper part of the sedimentary column. The lower part of the stratigraphic column (and closer to the mountains) consists of relatively coarse detrital sediments and halite (Figure 1.4) (Yechieli and Gat, 1997; Kaufman et al., 1992).
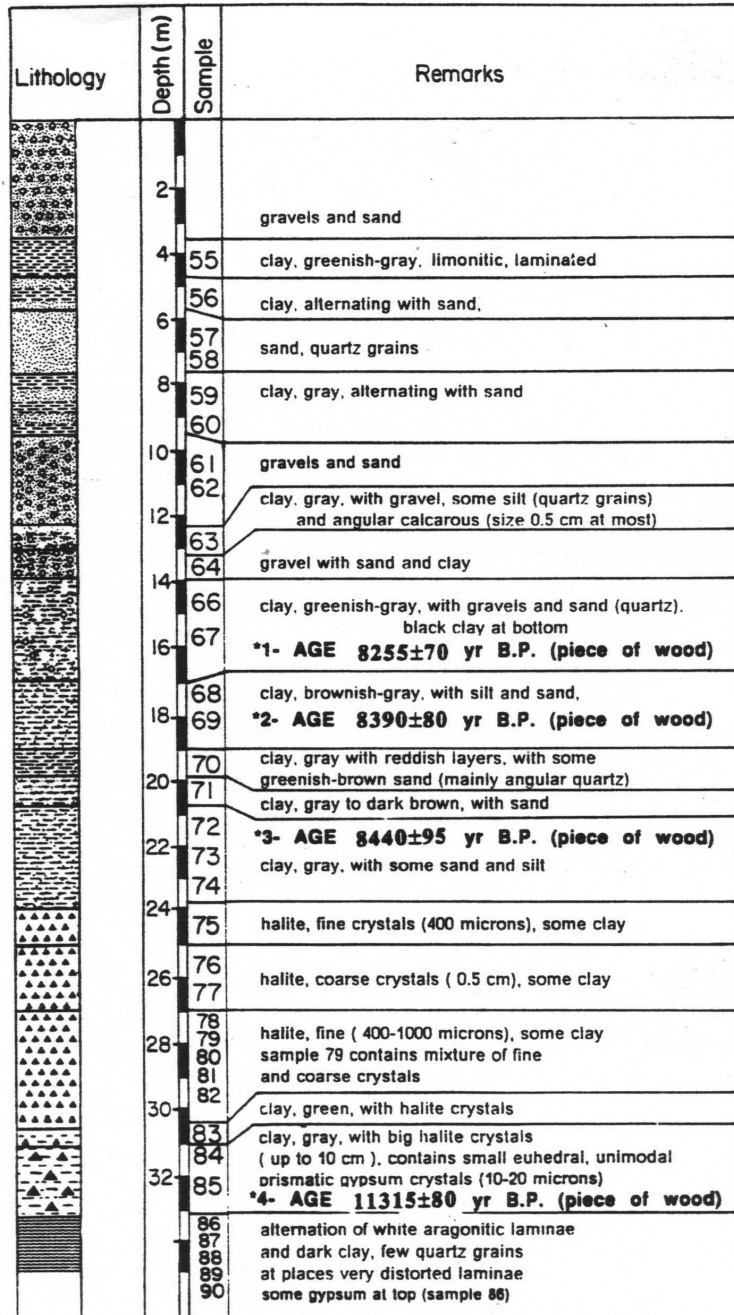
Figure 1.4 – Stratigraphic cross-section of the sediments from drillhole DSIF (Dead Sea Interface) including radiocarbon dates (Yechieli et al., 1993)

Past water level changes - The Dead Sea is the latest in a sequence of lakes that have filled the structural depression of the Dead Sea rift during the past 20 million years (Niemi, 1997). Lake Lisan was the precursor of the Dead Sea. Based on the observation of drainage systems presently underwater, the lake level dropped to approximately -700m during the transition between the Lisan Lake and the present Dead Sea (Figure 1.5) (Neev et al., 1967).

The salt layer - The latest lake level drop on the transition between the Lisan and the Dead Sea lakes is supported by massive salt beds deposited in the both the southern and the northern basins of the Dead Sea. These massive salt beds were dated prior to 9,850 14C yr B.P. on the southern basin (Neev, 1964), and between 11,300 and 8,400 14C yr B.P. (Yechieli et al., 1993) in the southern part of the northern basin (Figure 1.4 and 1.5). Based on these dates, the extremely dry event marking the end of Lake Lisan took place between 11,000 and 10,000 14C yr B.P. (Frumkin, 1997).
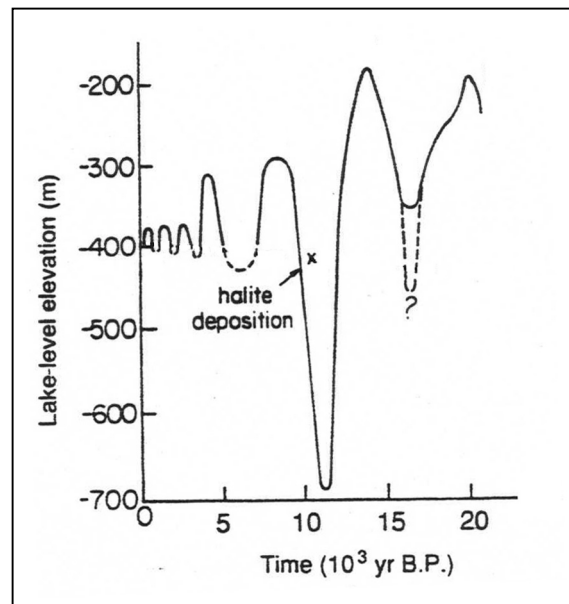
Figure 1.5 – Lake level elevation of the Dead Sea and its precursor Lake Lisan (Yechieli et al., 1993)

Recent water level changes - Since the early 1960s, large amounts of freshwater have been diverted from the Jordan River, the main water tributary of the Dead Sea. The decrease in input, combined with high evaporation rates, have resulted in a rapid dropping of the lake's level at a rate of about 0.5 m/yr between 1960 and 1980 (Klein, 1985) and by 0.8 m/yr between 1981 and 1989 (Anati et al., 1989; Yechieli et al., 1995) (Figure 1.2). In case of a similar climatological and hydrological conditions, the decrease is expected to continue, though at a lower rate, until a new equilibrium in the water balance is reached, in about 400 years, at 100-150 m below the present water level (Yechieli et al., 1998; Yechieli and Gavrieli, 1999).

Terra Nova - With the lowering of the lake's water level, shores which were covered by the Dead Sea 10-40 years ago are now exposed (Yechieli and Gavrieli, 1999). This new land, the *Terra Nova*, is partially drained but also subjected to processes resulting from exposure to the new atmospheric and hydrological environment. The extent of the area exposed by the regression of the lake depends on the gradient of the coast. (Yechieli and Gat, 1997).

Shore characteristics - The newly exposed western coast of the Dead Sea can be characterized according to three coastal types, which differ in their hydrological settings. The first type, which is found mainly in the northern section of the coastline, e.g. En-Feshkha and Turiebe (Qane-Samar) areas, is characterized by springs discharge domination. The second type is characterized by creek discharge zones, in

which both surface and subsurface flow are prominent on a wide area basis. And the third type is characterized by elevated areas between the major Creeks (Yechieli and Gat, 1997).

Ground water and hydrological setting - Due to its location below sea level, the Dead Sea basin is the hydrological outlet for the eastern slopes of the Judean Mountains. The runoff pattern is created by flash floods that occur in the large creeks several times a year during the winter, and by subsurface drainage in the aquifers. The subsurface drainage is springing above and below the surface of the lake. The depth of groundwater level increases according to the distance from the Dead Sea, from few meters in the lake's vicinity (up to 500m from the lake), to a few tens of meters farther from the shore and toward the mountains (distance of 0.5-1.5 km) (Yechieli and Gat, 1997).

Fresh-saline water interface - The regression of the lake is also accompanied by the migration and re-configuration of the fresh-saline water interface. The fresh-saline water interface is the transition zone between the fresh and the saline aquifers. This interface changes its position as the water level of the lake decreases and migrates eastwards and downwards. The main mechanism that controls the migration is drainage of the original Dead Sea solutions eastwards. Meanwhile, the fresh groundwater penetrate former saline water areas by either lateral inflow or by upflow of water through fault planes (Yechieli and Gat, 1997). The exact depths of the fresh-saline water interface below the western coastline of the Dead Sea are not known (Yechieli et al., 1998).

Aquifers - There are three main aquifers in the area around the Dead Sea (Naor et al., 1987). The deepest aquifer is located on the sandstone layers of Lower Cretaceous Kurnub Group. The second aquifer, above the first one, is built of limestone and dolomite of the Upper Cretaceous Judea Group. The third aquifer is the alluvial aquifer of Quaternary rocks, which is generally separated from the other two by the faults along the western margin of the Dead Sea Rift. The decrease in Dead Sea level result in the decrease in groundwater level in its vicinity (Yechieli and Gavrieli, 1999) (Figure 1.6).
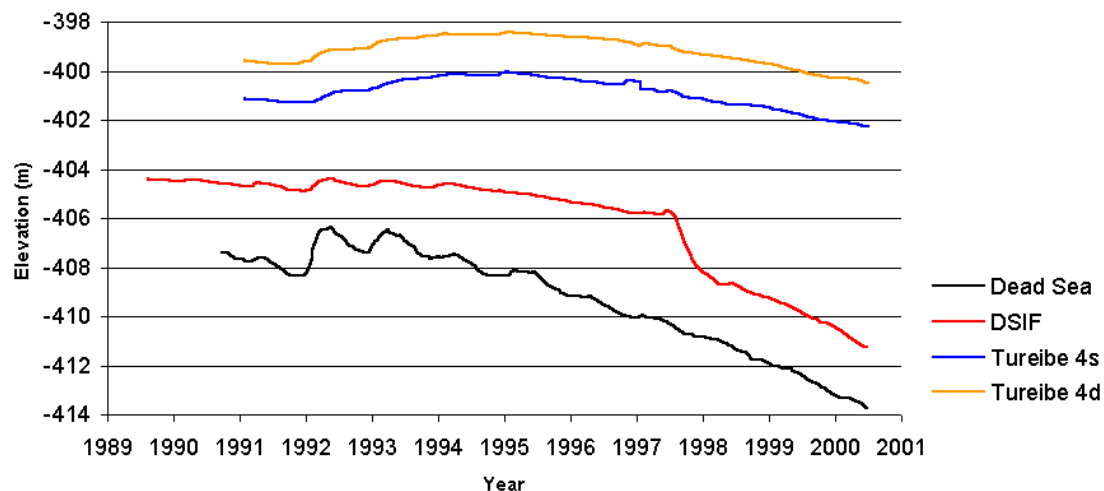
Figure 1.6 –Water level of the Dead Sea (black) and ground water level in three drill-holes along the Dead Sea shores, over a twelve years period (GSI, 2001).

1.2 Current and previous studies

Most of the studies on the formation of sinkholes along the Dead Sea shores were conducted in the last two years (1998-2000), by a combined team from the Geologic Survey of Israel and the Geophysical Institute of Israel. In earlier studies Arkin (1993) and Arkin and Michaeli (1995) described and explained surface subsidences and sinkholes formation.

The main geologic, hydrologic and engineering conditions in the region under investigation are used as the basis for the models suggested for the surface subsidences and sinkholes formation. The sinkholes are usually formed by a rapid collapse of the surface. Therefore, it is agreed that a subsurface cavity exists prior to the collapse. However, the subsurface cavity's properties (i.e., dimensions, depth and formation) are a disputable aspect (GSI, 1998). Two main models of sinkhole formation were proposed in the beginning of the project:

1. Subsurface flow of fine particles:

The suggested mechanism (Arkin and Michaeli [1995]) relates the formation of the subsurface cavities to disposal of fine-grained particles from under alluvial fans by water flowing through the alluvial fans. The water which flows above the water table, within the alluvial fan, also percolate downward during floods. The cavity develops upwards by piping as its roof collapses progressively in the alluvium. A sinkhole forms when the collapse levels reach the surface.

2. Deep salt layer dissolution (Wachs D. and Primerman D. (GSI, 1998)):

Salt layers were found to exist in the subsurface. Cavities are formed in the salt in places where unsaturated water (with respect to salt) reaches the layer and dissolve the salt from underneath it. The failure of the roof of such cavity begins a series of subsurface collapses. Eventually the collapses reach the surface and a sinkhole is formed.

The major difference between the two above mechanisms is the location of the initial cavity and the manner of its formation. In the first mechanism the initial cavity is formed by downward seepage of unsaturated water; the cavity is located in the alluvium, close to the surface; and the sinkhole is created only due to alluvium collapse. However, the second mechanism states that the initial cavity is located deeper, in a salt layer, and formed by upward percolation of unsaturated water that dissolve the salt beneath the alluvium (Ibid.).

In 1998 (the beginning of the Sinkholes Project formal research) neither of these mechanisms were preferable. Since then, the second one became more acceptable and is used as the basis model in the different studies, which are listed below. The assumptions of the salt dissolution model are:

1. There are **cavities in the subsurface**, both in deep salt layers and in shallow alluvium. The cavities are deficit in mass, which can be identified in a microgravity survey, and sometimes, when shallow, by Ground Penetrating Radar.
2. Cavities in the **deep salt layer** initiate a collapsing cascade. The salt layer spatial distribution (top of the salt layer) can be mapped by seismic refraction surveys, since the velocity of the seismic waves increases prominently in the alluvium-salt interface. A certain but local identification of the salt layer is made in drills.
3. The formation of the cavities in the salt is caused by its contact with **unsaturated water** (with respect to NaCl). Electric and Electromagnetic methods (i.e., FDEM, TDEM, DC and NMR) can locate these unsaturated water bodies, which differ from their surrounding in their electric conductivity.
4. Sinkholes appear in clusters that, in places, have a **rough linear appearance** in a plain view. The sinkhole distribution in time and space can be mapped in the field

and seen in air photos. The linear appearance may correspond to subsurface fractures. These fractures can be identified in seismic reflection surveys as systematic discontinuities in reflectors.

From the beginning of the sinkhole research near the Dead Sea it was clear to the researchers that the sinkhole phenomena is a complicated engineering-geological problem. Therefore, attitude of the studies were interdisciplinary, combining geomorphology, engineering geology and geophysics (Wachs, 1999). The sinkholes' formation in different lithologies led to the thought that their initiation is located deeper than the upper few meters of the subsurface. The research is conducted in three main levels: 1) Collecting all the information available from fieldwork, air-photos and previous published reports. 2) Learning the geology, through the stratigraphic, structural, hydrological and engineering aspects. This is done using several geological, geophysical and photogrametrical methods, which are specify below. 3) Developing geophysical means for detection of sinkholes' precursors, i.e. micrograviometry, electromagnetic and ground penetrating radar.

1.2.1 Mapping

Raz (1999 a and b) mapped sinkholes along Dead Sea shores. Itamar and Reizmann (2000) analyzed air photos of the Dead Sea shore from 1990 to 1999. According to both studies the sinkholes are formed along most of the western shores of the Dead Sea, from Mor site, the southernmost group of sinkholes to Dekalim site, the northernmost (Figure 1.7). The first sinkholes were formed before 1982 along the shores of the southern basin of the Dead Sea. The sinkholes of the northern basin began to appear in 1993. According to Itamar and Reizmann (2000), The earlier formation along the southern basin is an outcome of the moderate slopes of the shores. These southern shores expose more areas for every sea level lowering than the steeper shores in the northern basin. Therefore, the sinkholes are distributed over larger areas (and farther away from the recent shoreline) along the southern basin shores. The air photo analysis showed that in most of the sinkhole sites (7 out of 13) the sinkholes are not aligned along linear features.
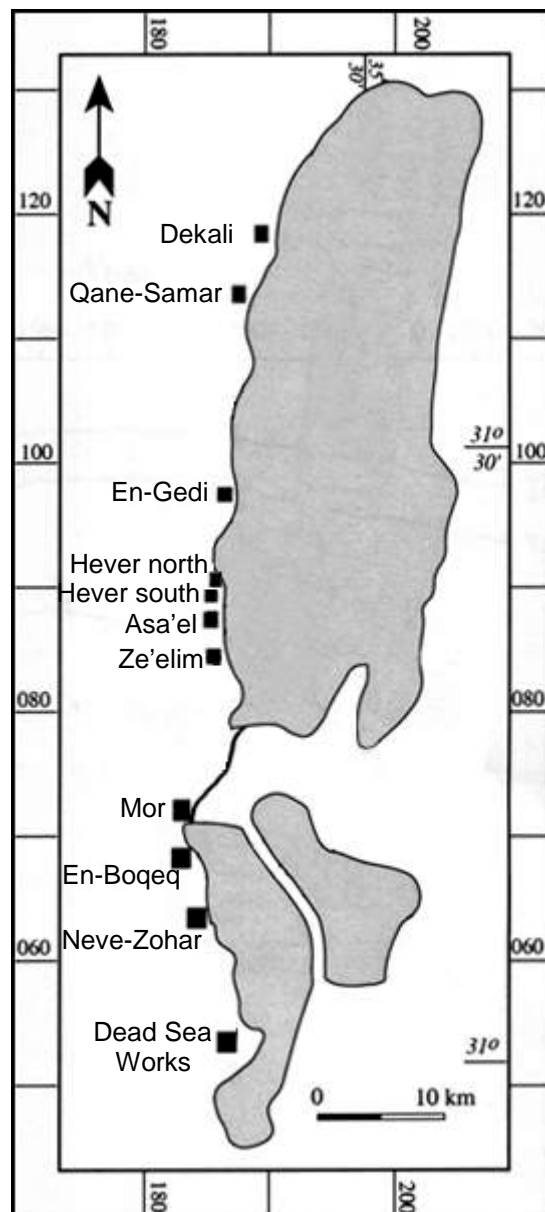
Figure 1.7 – Location map of the different research sites, based on Itamar and Reizmann (2000).

1.2.2 Geophysical studies

Several geophysical studies using various methods were conducted, in sinkhole areas along the Dead Sea shores (Shtivelman, 2000a) at the Newe Zohar (Ronen, 1997; Shtivelman, 1998; Shtivelman et al., 1994), En Boqeq (Beck and Ronen, 1994; Ronen and Ezersky, 1998; Ronen et al., 1992), Hever (Shtivelman, 2000a; Shtivelman, 2000b; Shtivelman et al., 1999), and En Gedi (Ronen and Beck, 1997; Ronen and Ezersky, 1997) (Figure 1.7). The results of these surveys are summarized below:

Seismic reflection surveys were conducted in the Newe Zohar (in 1994) and Hever (in 1999) sites. These surveys were planned to provide structural and stratigraphic information on the shallow subsurface at a depth range of 80-200m. Several anomalous zones were detected on the sections in which the reflectors are disturbed systematically. These anomalies were interpreted as shallow faults which cross the section. The anomalous zones at depth are roughly located beneath the sinkholes at the surface. Shtivelman (1999) suggests that these seismic anomalies may serve as an indicator for areas of potential sinkhole's development.

Several **seismic refraction surveys** carried out along the Dead Sea shores indicate the presence of a relatively shallow high velocity layer. Shtivelman (2000a) suggests that this high velocity layer relates to a salt unit. In the southern part of the Dead Sea coast (Newe Zohar) the P waves velocity in the layer is about 3500-3700 $^m/_{sec.}$ In the northern coasts this velocity varies between 2600-3000 $^m/_{sec.}$ The salt layer extends from the southern coasts, roughly until Qane creek (Figure 1.7) in the northern basin of the Dead Sea. No evidence was found for the salt layer north of Qane creek (GSI, 1998). In the En Gedi area, the salt layer extends at least 300m west of the main road.

Ground Penetrating Radar (GPR) surveys were carried out at Newe Zohar (Shtivelman et al., 1994) and in the camping site of En Gedi (Arkin et al., 2000). According to Shtivelman et al. (1999) in places where the subsurface has high conductivity, the maximum penetration depth of the GPR is about 5m. Arkin et al. (2000), state that the data obtained by the GPR in alluvial fans environment is reliable. Whether reliable or not, the GPR gives information only about the shallow subsurface (the upper 5m), and therefore currently is seldom used as an indicator for potential sinkholes occurrence, which are believed to initiate at depths grater than 5m.

Frequency Domain ElectroMagnetic (FDEM) surveys were carried out in En Boqeq (Ronen et al., 1992), Hever (Shtivelman et al., 1999), and En Gedi (Ronen and Beck, 1997) sites (Figure 1.7). In general, the conductivity in the subsurface is very high near the Dead Sea coastline and decreases westwards. These conditions limited the penetration depth of the FDEM surveys to very shallow depth (few meters). Few anomalous high resistivities were detected in places, but their relationship with sinkholes is yet unclear.

Time Domain ElectroMagnetic (TDEM) measurements provide more reliable information on the distribution of resistivities up to a depth of 100m, although the lateral resolution is somewhat lower (15m). Saline water saturated lithologies have extremely low resistivity values. Two main resistivity units were clearly detected in all profiles in Shtivelman et al. (1999). Shtivelman et al. (1999) s surveyed at the Hever site, the upper unit had a generally high resistivity complicated by local low resistivity anomalies. The lower unit was characterized by very low resistivities complicated by relatively high resistive anomalies. The later anomalies, which are widespread throughout the Dead Sea coastal aquifer (Kafri et al., 1997), indicate that the aquifer is a multiple system, in which brine saturated layers can be underlain by

relatively low salinity waters.

        Microgravity surveys were conducted in the Dead Sea Works (Rybakov et al., 1999), Hever (Rybakov et al., 1998), Newe Zohar, En Gedi, and Mineral beach sites (Rybakov and Goldsmidt, 1999) (Figure 1.7). The microgravity technique is the only surface geophysical method that can locate a subsurface cavity regardless of its shape or fill material, as long as there is a sufficient density contrast, and as the volume of anomaly detected is big with respect to its depth. A large and complicated negative gravity anomaly (reaching –0.08mGal) was found in the 'Hever south' site, covering four out of five sinkholes exposed at the surface. The interpretation of this anomaly as a subsurface cavity was confirmed in two drill wells.

1.2.3 Summary

        The results from the refraction surveys and the drills that were done confirmed the existence of a salt layer in the subsurface. The salt layer extends laterally along the Dead Sea shores. Locally, the salt layer extends up to a kilometer westwards from the shore. The upper surface of the salt layer is located at depths of 20-30m, and its thickness is more than 10m. According to drill data, several meters thick clay layers confine the salt layer from both above and below. The electromagnetic surveys show evidences for the existence of water with low conductivity (unsaturated with respect to NaCl) below the salt layer, at the southern Hever sinkhole site. Microgravity surveys that were conducted at Hever south site and southwards, at Asa'el site (Figure 1.7), showed that sinkhole areas are associated with negative gravity anomalies. These anomalies reflect mass deficit at the subsurface, suggesting that cavities exist at depths of several tens of meters. The salt layer was found to be highly permeable with a thickness of 11m and at depth of 24m (its top) in the drill at Hever south sinkhole site. The dimensions of the cavities in the salt layer are not known.

1.3 Objectives

        The fast expansion of the sinkhole phenomenon, since 1995, had arisen the need for developing methods that will detect its precursors and diminish the risk. Together with field observations, combinations of geophysical methods were practiced in sinkhole sites, i.e. seismic methods, electromagnetic methods, and microgravimetry measurements. Nevertheless, the surface behavior around the sinkholes (deformations in small and large area scale) had not been examined so far. If sinkhole formation is accompanied by any regional surface deformation, like surface subsidences, then tracking such changes and correlating them with observed sinkholes can provide an additional method for estimating the potential of an area to develop sinkholes. In this research three geodetic methods (two space-based positioning methods and one visual-based positioning method) were used for monitoring the small-scale elevation changes: 1) The **G**lobal **P**ositioning **S**ystem (GPS) technique, which is very accurate for measuring position changes in specific locations; 2) The **I**nterferometric **S**ynthetic **A**perture **R**adar (InSAR), which measures surface elevation changes in a wide spatial resolution; and 3) The **E**lectronic **D**istance **M**easurement (EDM), which give the distance of the measured points relative to the instrument. The GPS and the EDM measurements are used for monitoring the sinkhole site at the northern part of Hever alluvial fan, on the western coast of the Dead Sea, while the InSAR will focus on a larger area, the Mezada plain.

2. Sinkholes and land subsidence - Description of the phenomena

2.1 Basic definition of sinkhole

Sinkholes are "enclosed hollows of moderate dimensions" originating due to dissolution of the underlying bedrock (Monroe, 1970). More specifically, sinkholes are surficial landform, found in *Karst* areas and consist of an internally drained topographic depression that is generally (but not in all cases) circular, or elliptical in plain view, with typically bowel, funnel, or cylindrical shape. Although the circular plan view and funnel shape are ideal forms for a sinkhole, they may coalesce into irregular groups or have shapes that are much more complex (Wilson, 1995). The terms *sinkhole* and *Doline* are synonymous.

Surface depressions and collapses in Karst terrain are formed as a result of dissolution of carbonatious rocks. Along the Dead Sea shores the carbonatious rocks are located several thousand meters below the surface. Therefore the subsurface voids related to the depressions are termed *PseudoKarst* instead of Karst. Nevertheless the surface depressions and collapses characteristics fall within the definition of sinkholes.

2.2 Sinkhole types

2.2.1 Solution Sinkhole

A Solution Sinkhole (or *solution depressions*) forms above a favorable point, such as a joint intersection (Beck, 1984). In the subsurface, the joint intersection increases the permeability of the rocks. As a result, the rocks (e.g. limestone, gypsum or salt) are dissolved away from beneath a soil covering layer (Terzaghi, 1913). A cavitation process propagates through a cohesionless soil layer covering the dissolved matter. The consolidated, coarse grained, covering soil layer becomes porous as its finer grains are filtered downwards into the widening interstices of the layer below. This coarser grained layer has the direct influence on the subsidence at the surface. The cohesionless fine grains erode into small openings in the porous layer, similar to the flow of fine sand through the throat a sand watch (Figure 2.1). When aided by downward water percolation, a rather narrow erosion channel develops and propagates almost vertically upwards. Eventually, a funnel-shaped sinkhole develops at the ground surface with uniform side slopes of repose sand angle, typically 30 to 35 degrees (Sowers, 1996).

Figure 2.1 – Development of a (b) funnel-shaped sinkhole from (a) the initial stage (Sowers, 1996).
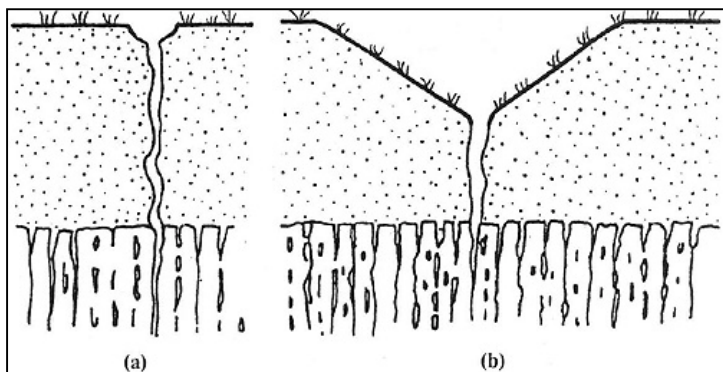
2.2.2 Collapse Sinkhole

A ***Collapse Sinkhole*** is formed by a rapid, usually single occurrence, downward movement of soil mass into a sub-surface cavity (Bögli, 1980), after its roof had reached its failure point. A slow downward movement of the surface (***Subsidence Sinkhole***) precedes the collapse. The collapse appearance at the surface is circular (Figure 1.3).

2.2.3 Sinkhole like phenomena

Karst processes create closed karst and pseudokarst cavities, which initiate indirectly sinkhole-like phenomena, by subsidence and collapse into the underground cavities. The main forms are sinkholes (or doline), ***Cenotes***, ***Karst window***, and ***Karst gulf***. There are also numerous atypical karst basins of various sizes that do not fall into any of those categories (Ibid.). The most suitable definition describing the studied pits along the Dead Sea is 'sinkhole'. Here are definitions of the other phenomenon noted above:

Cenotes are collapse doline above a high karst water surface. Its diameter to depth ratio is below one. Their walls are vertical and occasionally overhanging (Figure 2.2a). Neighboring cenotes, as a rule, show the same water level height. A ***karst window*** is a large funnel-shaped doline, at depths of which a short stretch of a cave river is visible. Karst window can reach a diameter of 130 m and depth of 20m, as found in Spring Mill State Park (USA) (Figure 2.2b). A ***karst gulf*** is created by the collapse of a broad cavity, which is located close to the surface. Later extensions follow when corrosion cuts back under the overhang, and lateral breakdown occurs (Figure 2.2c) (Bögli, 1980).
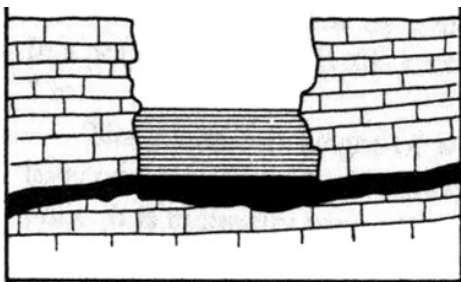
Figure 2.2a – Cenote (Bögli, 1980).
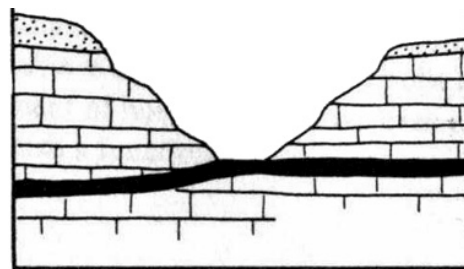
Figure 2.2b – Cross-section of Karst window (Bögli, 1980).
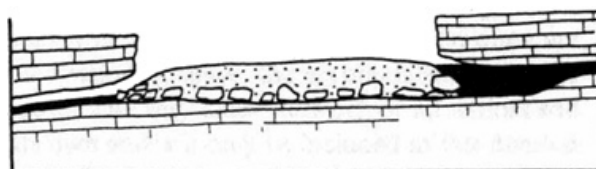
Figure 2.2c – Cross-section of karst gulf (Bögli, 1980).

2.2.4 Short sinkhole terminology

Term	Definition A summary of sinkhole definition and terminology according to Fairbridge (1968), Sweeting (1973), and Sowers (1996).
Doline	A solution depression or a sinkhole. A circular or elliptical or irregular-shaped depression in the ground surface.
Cutter	A solution-enlarged fissure or *slot*.
Epikarst	The soft zone of unconsolidated residual soil located immediately above the rock surface, and in the dipper slots between the solutioned *pinnacles*.
Pinnacle	The narrow rock remaining between wide slots.
Polje	An extremely wide or valley like, flat bottomed solution depression.
Pit	A more or less vertical shaft, usually a rounded solution enlarged intersectioning fissure system.
Slot	A solution-enlarged steep or vertical fissure.
Solution shaft	A near vertical, almost cylindrical holes, formed by stope activity or by falling water.
Swallow hole	A sinkhole in or adjacent to a stream into which the stream's flow disappears.
Uvala	A complex assortment of solution depressions or sinkholes, with their bottoms at different levels and sometimes depressions within depressions.

2.3 Sinkhole Formation and development in evaporite rocks

One of the most important ingredients in the formation of a sinkhole is the underground cavity (the *receptacle* (Newton, 1984)). The receptacle is formed when unsaturated groundwater percolate through evaporite rocks (e.g. salt) and dissolve them. The dissolution of evaporites is attributed to one or more of the following principles: (1) centripetal flow of unsaturated waters from the basin margins, towards the basin; (2) centrifugal flow of unsaturated groundwater from the basin interior towards its margins; and (3) regional fracturing in the subsurface (Anderson and Knapp, 1993). Once a cavern is formed, surface subsidence can take place slowly or rapidly. In the former case a sand-watch like solution depression forms at the surface (Figure 2.1). In case of rapid or sudden subsidence, a collapse sinkhole develops (Myers, 1962). Most collapses forming sinkholes result from cavity roof failures in unconsolidated deposits overlying the bedrock (carbonate or evaporite rocks) (Newton, 1984).

2.3.1 Water table level changes effects

Fluctuations in the level of the water table, on the margins of a basin, are consequent to water level changes in the basin itself. The water level changes of the basin have two major effects, a chemical and a physical one. The physical effect - the fresh-saline water interface changes its position and migrates towards the basin (*centripetal flow* (Ibid.)). This change in the hydrological settings may confront unsaturated water (with respect to salt) with highly soluble evaporite sediments (e.g. halite and gypsum), that may exist in the subsurface. As a consequence evaporites may dissolve away (the chemical effect).

Two additional processes subsequent the water table fluctuations of a basin margin: changes in the volume of the aquifer skeleton and artesian water seepage. The effective stress principle, first proposed by Terzaghi (1925), claims that the interstitial water, which fill the pores of the aquifer skeleton bear the weight around them by the effective stress. Hence, when ground water level is decreased, support previously provided by pore fluid pressure is transferred to the skeleton of the aquifer system. As a result the aquifer skeleton undergoes compaction. Contrariwise, when ground water level rises, pore pressure increases and the aquifer skeleton expands. These fluctuations (compaction and expansion) create only small elastic deformation of the

aquifer system and small displacements at the surface, in the level of centimeters. Another effect of the water table level decrease is relieving the normal pressure from confined water horizons, enabling upward water seepage by artesian pressures.

Centrifugal flow

Sediments in the shallow subsurface of a subsiding basin are subjected to diagenesis. Many aspects of diagenesis involve the expulsion of interstitial waters of various origins (e.g., physical compaction of sediments, dehydration of clay minerals) (Anderson and Knapp, 1993). According to Perrodon (1983), the interstitial water of sediments subjected to normal pressures are progressively expelled. The interstitial water are first expelled from the deepest zones, which are subjected to higher pressures, and migrates towards zones with a weaker pressure (laterally towards the edges and vertically through the beds into the surface layers). Generally, as a result of electrofiltration, the expelled waters are less saline than the interstitial waters that remain. In this way the outward flow of unsaturated interstitial waters in response to burial under the sediments of the lake, can reach evaporite layers in the subsurface and dissolve them (Anderson and Knapp, 1993).

2.3.2 Subsurface cavity formation and evolution

Karstifiable rocks

The formation of karst landscape and karst hydrography is related to the existence of specific rocks group types: evaporites (e.g. gypsum, anhydrite, and salt); carbonates (e.g. limestone and dolomite); and quartzite (only under conditions of extreme tropic humidity). An additional prerequisite for the formation of an underground cavity is drainage of the soluble matter. In other words, if the soluble matter is not drained the system reaches saturation and the dissolving stops (Bögli, 1980).

The cavity dome

The propagation of the cavity dome is generated by a combination of progressively upward slaking, ravelling, slab falls, and erosion of the upper soil layer into an open the rock below (Figure 2.3). Changes in the water content of the clayed soil above the fissured bedrock may initiate a *slaking* process – a sudden expansion and softening of relatively dry or partially saturated soils. The slaking, which takes place on the soil-water interface, initiates the formation of subsurface cavity. After a cavity in the soil is present the *ravelling* occurs when thin fragments of soil separate from the mass and fall out, to enlarge the cavity. The soil fragments and slabs fall into the bottom of the soil cavity and accumulate in irregular mounds (Sowers, 1996).

Generally, the dome enlarges outward and upward towards the ground surface. In cases where a source of infiltration exists, such as a leaking pipe, the upward propagation of the dome will deviate toward that source. The shape of the dome varies with the nature of the overburden layer, in which wider domes is more likely to develope in a more cohesive soil. The ratio between the diameter of the cavity and the hole below (in the bedrock) varies largely, even beyond 100. The dome is usually widest near its top with the shape of an inverted teardrop (Figure 2.3a). In cases where the cavity reaches a relatively more cohesive layer during its propagation, the roof of the cavity tends to widen laterally (Ibid.).
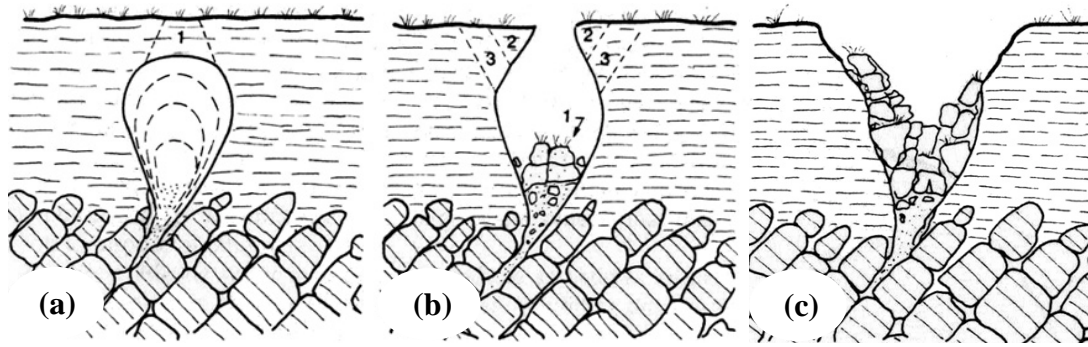
Figure 2.3 – Collapse of an erosion dome into a inverted tear-drop shaped subsurface cavity: (a) the subsurface cavity and its potential dropout roof; (b) initial roof dropout, while the rim is still hanging; (c) final rim collapse (Sowers, 1996).

2.3.3 Surface sinking and collapse

As long as the soil of the receptacle is strong enough to support an arch over the opening, there may be no obvious reflection of the dome at the surface. However, if the roof of the dome is not sufficiently strong, a gentle sink may develop at the surface. The sinking is accompanied by the formation of circular tension fissures. The circular tension fissures are centered above the dome. Their diameter is usually smaller than the dome's largest diameter.

When the roof of the dome becomes thin enough or the dome becomes wide enough the shear stresses in the soil's roof exceed the soil strength. A truncated cone of (intact) soil drops downward into the cavity below, leaving a near circular hole whose sides slope outwards with increasing depth (bell shaped) (Figure 2.3b). With time, the overhanging walls of the hole slide into the opening below, increasing the ground surface diameter of the hole. Eventually, the hole becomes funnel-shaped, more or less centered over the rock hole below.

2.4 Land subsidence

Land subsidence is a gradual settling of the ground, usually induced by lowering of the ground water. Land subsidence may stretch laterally up to an area of a few square kilometers, while the vertical displacement is the order of few centimeters. The main reason for the gradual ground settling stems from changes of the granular structure in the subsurface, the skeleton (Figure 2.4b). Water of the aquifer system occupies the pores and cracks of the skeleton, and supports its structure. The aquifer system is not fixed, and any lowering in the ground water level decreases the pore pressure of the water, and thus decreases the support for the overlaying material. Both the aquifer and aquitards that constitute the aquifer system deform, but in different magnitude.

The reversibility of the skeleton deformation depends upon the combination of many components. The two most important components are ground composition and ground water level change. Unconsolidated rocks are more vulnerable for changes in the pore pressure. Furthermore, the degree of compliance of the unconsolidated rock's skeleton is directly related to its percentage of clays. Hence, the deformation of unconsolidated rocks with large percentage of clays is irreversible (Figure 2.4c). As long as ground water level fluctuates with small amplitude, the skeleton can bear such small changes in the pore pressure. Such fluctuations are usually daily or seasonal. In this case the deformation of the skeleton, and hence the subsidence of the surface, is

reversible. When the change in the ground water level is a long-term continuous decline, then the pore pressure decreases significantly, resulting in an inelastic compaction of the skeleton. The result on the surface is an irreversible land subsidence (Figure 2.4).

Land surface

Sand and gravel

Clay and silt (Aquitards)

(a)

(b)

Land surface

(c)

(d)

1 – Reversible surface subsidence (the subsurface deformation is elastic)

2 – Irreversible surface subsidence (the subsurface deformation is inelastic)

Figure 2.4 – When the ground water level drops, the pore pressure decreases between the particles of the skeleton. If the ground water level is seasonal or daily ((c)1) the surface subsidence will be reversible. If the water lowering is continuous ((c) 2) the subsidence will be irreversible, and the skeleton will collapse (d).

Figure 2.4– while the ground water level is high the water fill the pores between the different particles of the ground (a). The pore pressure of the fluid, between the particles bears part of the weight of the ground above it (b).

3. Work methods

This research monitors and characterizes the vertical surface displacement induced by, or related to sinkhole activity along the western shore of the Dead Sea, in the following locations: (1) in the eastern part of the Mezada plain (between Hever alluvial fan, in the north and Ze'elim alluvial fan in the south); and, (2) at the northern part of Hever alluvial fan (Figures 1.1 and 1.7). The measurements were conducted using three types of geodetic techniques: space-based GPS and InSAR, and terrestrial-based positioning EDM. Most of the field measurements were carried out using Global Positioning System (GPS) equipment, in both real time and post processing modes, at the Hever site. The obtained data provides four-dimensional (three in space and one in time) point positioning, in a global reference frame. The Real Time Kinematics (RTK) technique provides the surveyor instantaneous accurate positioning in the field. The RTK system enables viewing and arranging the data in the field. The regular post processing kinematic GPS also enables positioning calculations and arranging the data, but after the fieldwork is over. Both kinematic techniques provide very accurate positioning, with uncertainty level of 1cm in the horizontal components and 3cm in the vertical component. Additional observations were made using the **I**nterferometric **S**ynthetic **A**perture **R**adar (InSAR) on the Mezada-plain site. The InSAR technique compares SAR images obtained at various time periods (days to years) to detect local and regional surface movements. Both the vertical and the horizontal accuracies of the method are in the level of 0.5 centimeters. In general, the accuracy is limited to by the wavelength of the satellite signals. Hence, a pixel of the InSAR image has the dimensions of 20X4 meters in the field. Additional measurements were carried out with Electronic Distance Measurement (EDM), at the Hever site. The EDM measures precise distance (horizontal, vertical and angles) between specific points. The GPS and the EDM techniques provide discrete positioning data, which is used in the chapter 6 (Results) to generate various map types.

3.1 GPS

3.1.1 What is GPS?

The Global Positioning System is a navigation system that provides its users with a 24-hours space-based three-dimensional positioning and timing information. This information is obtained from a set of 28 satellites, which operate simultaneously. Today the GPS is deployed and operated by the US Department of Defense (DOD). The development of the system began in the early 1960s, when NASA and the US military started pushing towards space-based positioning. In 1993 the **N**avigation **S**atellite **T**iming and **R**anging (NAVSTAR) **G**lobal

Figure 3.1 - GPS satellite (SNDC, 1997).

Positioning **S**ystem (GPS) became fully operational. During its developmental and experimental stages, the GPS served a variety of positioning needs (military as well as civilian), such as: navigation on land, sea, air, and space; guidance of robots and other machines; and high precision geodetic surveys (Leick, 1995). The GPS consists of three interacting components: space, control and user segments. The **Space Segment**

consists of satellites that orbit the earth and emit signals. The **Control Segment** consists of control stations that track all GPS satellites computes their orbits, and update the satellite orbit and ephemeris. The **User Segment** consists of receivers that receive the transmissions of the satellites and calculate receiver's absolute position, or relative position with respect to other receivers.

3.1.1.1 Space Segment

The space segment consists of 28 GPS satellites that communicate with the other two segments by emitting and receiving signals. The satellites orbit the earth in 6 planes, each of them orbits the earth once every $11^h 56^m$ hours (Figure 3.2). The orbit altitude above the earth surface is about 20,200 km. The number of **S**pace **V**ehicles (SV) that circle the earth in each orbital plane is either four or five. The orbital planes are equally spaced, 60° apart, and inclined at about 55° with respect to the equatorial plane (Leick, 1995). The constellation of the satellites (Figure 3.2) provides the user with at least six space vehicles visible from any point on the earth (NSWU, 1999).
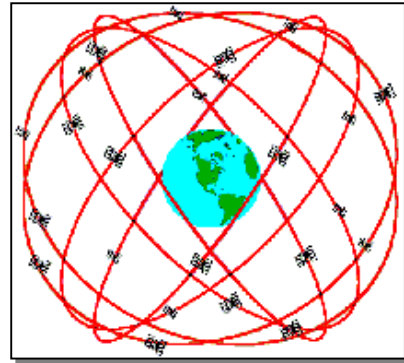
Figure 3.2 - GPS satellites constellation (Dana, 1999).

3.1.1.2 Control Segment

The control segment is responsible for operating the GPS system. It is comprised of a master control facility, located at Schriever Air Force base in Colorado, and six monitoring stations, distributed around the world (Leick, 1995). The stations monitor the signals emitted from the satellites (Figure 3.3). The signals include the precise orbital data (ephemeris) and clock correction parameters for each satellite. The information of each satellite is formatted, at the Master Control station, into updated navigation messages, (USCG, 2000).

GPS SV

Control station   Receiver
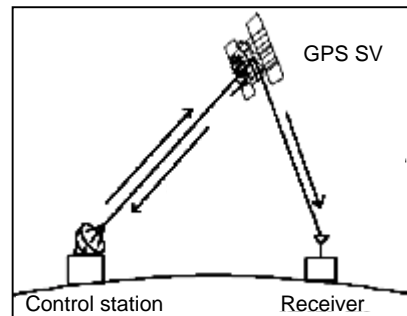
Figure 3.3 - The control segment (Dana, 1999).

3.1.1.3 User Segment

The GPS User Segment consists of the receivers, processors, and antennas that allow the users community to receive the GPS satellite broadcasts and compute precise position, velocity and time. Three-dimensional navigation is the primary function of the GPS, and it is used to support a wide variety of applications, i.e.: land, sea, and airborne navigation, surveying, geophysical exploration, mapping and geodesy, vehicle location systems (USCG, 2000). The relative positioning method provides precise positioning by cross-correcting data from two receivers that are synchronized and work simultaneously.

3.1.2 How GPS works

In order to estimate their position, GPS receivers observe two types of satellite transmissions: the **PseudoRange** and the **Carrier Phase.** The pseudorange is a measure of the distance between the antenna of the receiver and the satellite, at a

given time. The observed phase is the difference between the carrier phase (received from the satellite) and the phase of the internal receiver oscillator. Most of the GPS navigation receivers use the pseudorange, together with the satellite position estimates, for determining their position. However, in high-precision surveying, the carrier phase is favored (Leick, 1995). Tracking the carrier phase signal requires that at least two receivers, used at the same time. The three-dimensional positioning of the receiver is computed from the intersection spheres, whose radii are the pseudoranges of the satellites. The three-dimensional receiver velocity is calculated from the principle of Doppler effect in the received signal. The minimal number of satellites required for standard navigation is four, in order to get the forth dimension, time. More satellites in view can increase the positioning credibility, and under certain circumstances, can allow detection of out-of-tolerance signals (Dana, 1999). GPS satellite signals are also used for correcting the receiver clock offsets, allowing the use of an inexpensive receiver clock.

The **position** in **E**arth **C**entered, **E**arth **F**ixed **XYZ** (ECEF XYZ) coordinates (Figure 3.5) is converted within the receiver to geodetic latitude, longitude and height above the ellipsoid (or any other geodetic coordinate system). The latitude and longitude are provided in the geodetic datum that was configured in the GPS receiver, i.e. WGS-84. Using wrong datum can result in position offsets of hundreds of meters, or more.
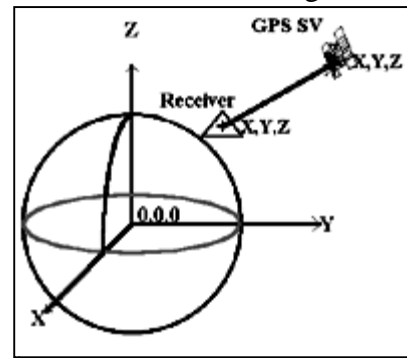
Figure 3.4 - Earth Centered, Fixed X, Y, Z coordinate system (Dana, 1999).

3.1.2.1 <u>Satellite transmissions</u>

All satellite transmissions are derived from the basic frequency of 10.23 MHz. Two carrier waves transmitted from the GPS satellites are multiples of the fundamental frequency: the L1 is at 1575.42 MHz and the L2 is 1227.6 at MHz. These frequencies are modulated with two types of codes (C/A-code and P-code) and with a navigation message. The chipping rate of the P-code is 10.23 MHz, whereas the chipping rate of the C/A-code is 1.023 MHz. The navigation message is modulated both on L1 and L2 carriers at a chipping rate of 50 bps. Different types of receivers make use of different parts of the GPS Signal Structure (see also Figure 3.6) and achieve different accuracy levels.
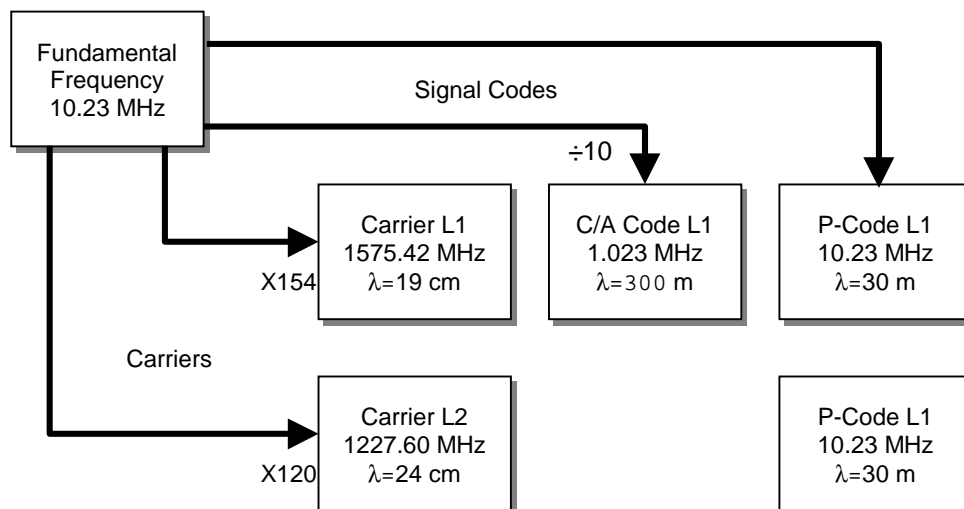
Figure 3.5 - GPS signal structure (λ represents wavelength).

All satellites transmit on the same carrier frequency, and yet are distinguished. Superimposing the P-code (precision code) with the carrier waves creates the **P**seudo**R**andom **N**oise (PRN) code, which attains distinction between the different satellites. Even though each week the PRN of a satellite changes it does not repeat itself for 37 weeks. Hence, the GPS week is the major time unit used, as all the codes are initialized every Saturday's midnight. The P-code is modulated on both L1 and L2 carriers.

The C/A-code (coarse/ acquisition) can be modulated on the L1 carrier or the L2 carrier as a ground-controlled option. Each satellite transmits a different set of C/A-codes. It can be easily distinguished by the ground receivers and therefore received simultaneously from different satellites. The navigation message contains information on the ephemerides of the satellites, GPS time, clock behavior, and system status messages (Leick, 1995).

3.1.3 Differential GPS (DGPS)

In standard navigation, a single GPS receiver observes the satellites in order to determine its geocentric position. However, surveying and other geodetic applications of the GPS require higher-accuracy positioning. Differential positioning (also called relative positioning) uses transmitted corrections between two or more receivers for better estimating pseudoranges. The receivers share the same celestial cap, and therefore track the same satellites. One of the receivers is static, and defined as the reference receiver, or **base station.** Its function is to compute the corrections for each satellite signals**.** Another receiver, the **rover station**, measures different locations in the field. The data obtained by the reference receiver is utilized to correct the measurements of the roving receiver. In this way, many of the common mode errors cancel or significantly reduced. The corrections are made in the field, in **real-time,** or after the end of the measurements, in **post-processing**. Other error sources can be reduced by placing the receivers in a static position, observing over a certain period of time (Leick, 1995). The accuracy of the measurements is limited by the relevant wavelength observed in the satellite transmissions. In differential navigation the pseudorange is used for positioning, hence, the accuracy reaches several meters level. The **K**inematic technique utilizes the carriers waves L1 and L2, which have short wavelength (Figure 3.6), as observables, to produces more accurate positioning than the DGPS.

3.1.3.1 Kinematic GPS

Kinematic-type GPS surveys are procedures whereby the position of a roving receiver is calculated relative to a stationary receiver (situated at a known geodetic mark) utilizing the carrier phases, of the satellite signals. In **R**eal-**T**ime **K**inematic (RTK) GPS the corrections are made in the field, as the receivers communicate through radio transmissions (i.e., VHF or UHF radio, and FM radio sub-carrier). In this technique only three station parameters need to be estimated. This is achieved by resolving the doubly differenced phase ambiguities on each epoch (Genrich and Bock, 1992). In order to achieve centimeter-level accuracies the RTK surveys should only be initialized. Locating the rover receiver over a known point for a few seconds makes the initialization of a single frequency receiver. Dual frequency receivers can be initialized by locating the rover over an unknown location for a short period. Once initialized, the system must track continuously at least four satellites in order to maintain accuracy (NSWU, 1999).

3.1.4 GPS Error Sources

Imprecise determination of the receiver position originates from systemic (e.g. noise and bias) and non-systemic (e.g. blunders) errors. **Noise errors** are the combined effect of errors in the pseudorandom noise (PRN) code and inaccurate function of the receiver. The noise errors may affect the positioning solution in imprecision of several meters (Dana, 1999). **Bias errors** result from Satellite clock errors, Ephemeris data errors, Selective Availability, Tropospheric and Ionosphere delays, Multipath, and Satellite geometry (Dilution of Precision factors), can result in errors in the order of several to tens of meters. **Blunders** may result from several sources: computer errors or human mistakes in the control segment can cause result in positioning errors ranging from one meter to hundreds of kilometers; user mistakes, (i.e. incorrect geodetic datum selection) can cause errors from several to hundreds of meters; and receiver errors (i.e. software or hardware failures) can cause blunder errors of any size (Dana, 1999).

3.2 Interferometric Synthetic Aperture Radar (InSAR)

The Interferometric Synthetic Aperture Radar (InSAR) technique is used for detecting horizontal and vertical changes in the ground surface of a definite area (usually 100X100 km), over a finite period of time. One of the by-products of the technique is a topographic model of the imaged area. The data is acquired by the ERS-1 and ERS-2 satellites that orbit the earth in an altitude of 725 km. Each satellite transmits signals along ray-paths pointed 90° clockwise to the trajectory at an average angle of 23° from the vertical (Figure 3.7) (Massonnet and Feigl, 1998). The basic idea of the INSAR technique is to use the phase of the reflected signal, in two or more images, to calculate the difference in ranges from two SAR antennas (that have a slightly different viewing geometry) to targets on the ground. The natural resolution of an orbiting radar instrument is a direct consequence of the ratio of wavelength to aperture, which is about 10^{-3}. Therefore, although observing from about 1000 km above the ground the primary resolution is about 10 km on the ground. To improve the resolution, the InSAR technique focuses the image, by emitting signals in a high

Figure 3.6 – The ERS satellite emits signals towards the ground surface, and receives their echo as it travels through its trajectory. The size of the satellite antenna limits the spatial resolution to about 5km on the ground. In the Synthetic Aperture Radar the signals acquisition technique "synthesize" a 5km long antenna. This increases the ground resolution about 150 times (based on Curlander and McDonough, 1985).
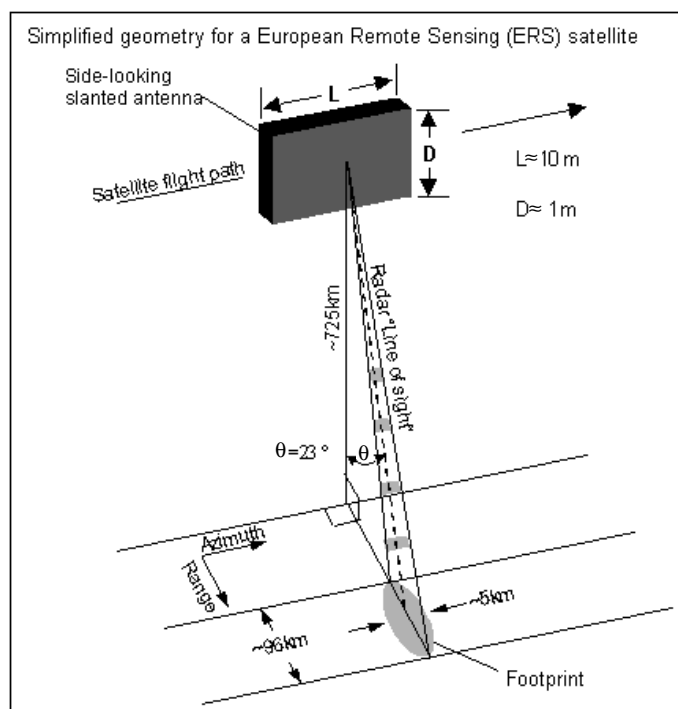
frequency (about 1 kHz) and receiving them along its trajectory. The received data is sorted in a technique similar to tomography, called synthetic aperture processing. The result resolution is improved by a thousand, equivalent to using an imaginary antenna with a synthetic aperture of 20 km (Massonnet and Feigl, 1998). Thus each pixel in the image is 20x4 meters in the field.

Each SAR image is a map of the ground reflectivity sorted by range (the distance between the radar antenna and the ground). The phase of each 4 by 20 m pixel measures both the range and the phase shift of the waves reflected from the ground. An interferogram (phase difference map) is made from two SAR images, taken at different times. The interferogram show fringes corresponding to contours of equal change in satellite-to-ground range (Massonnet and Feigl, 1998). The phase differences in the interferogram contain information of three sources: (a) relative orbital positions, (b) topography as seen in parallax by the satellites from slightly different orbits, and (c) changes in the position of the ground. In order to detect only the ground change, both orbit parameters of the different satellites are calculated as if they passed in the same height above the ground. Further adjustments are made for secant trajectories. The topography may be eliminated by subtracting a previously existing digital elevation model. Or, as in this study, the topography model is created through the work process (see below), and then subtracted from the interferogram.

To successfully image ground change, the interferometric technique requires four elements: data availability, suitable orbits, an elevation model, and good correlation (Ibid.). The base for the elevation model is the "Gtopo30" model of the USGS, which gives the elevation of points in a grid spacing of 1km. Upon this grid, an interferogram is made for two orbits with the shortest time difference available, with preference for a tandem (time difference of one day) (Figure 5.6). For finer elevation model, an additional interferogram is added, again with the shortest time difference, but with a greater baseline (the range in space between the orbits). For usable fringes to appear in the interferogram, the radar returns in the two images must be sufficiently correlated. If not, the interferogram breaks down into incoherent noise. Such noise can arise from changes in the characteristics of the reflecting surface, i.e. tilled fields, changes in the vegetation cover of the ground, and regression of the sea (like in the Dead Sea case).

4. Study areas

4.1 Location

The study was carried out along the western shores of the Dead Sea, on the eastern part of Mezada plain. The area was monitored in two levels of scale (see location maps, in Figure 4.1): **Area1** - A narrow strip of land was imaged by the InSAR technique. The strip, which is 13 km long and about 4 km wide, is sub-parallel to the current shoreline. It stretches between Hever alluvial fan, in the north (18600/09200), and Mezada alluvial fan in the south (18600/08000). **Area 2** -A smaller area (Figure 4.1) was monitored using the GPS and EDM techniques. Area 2 is located northwest of the Hever alluvial fan, in the northern part of area 1, about 1 km southeast of kibbutz En Gedi, between the coordinate (1) 18660/09125; (2) 18670/09140; (3) 18700/09120; and 18690/09105).
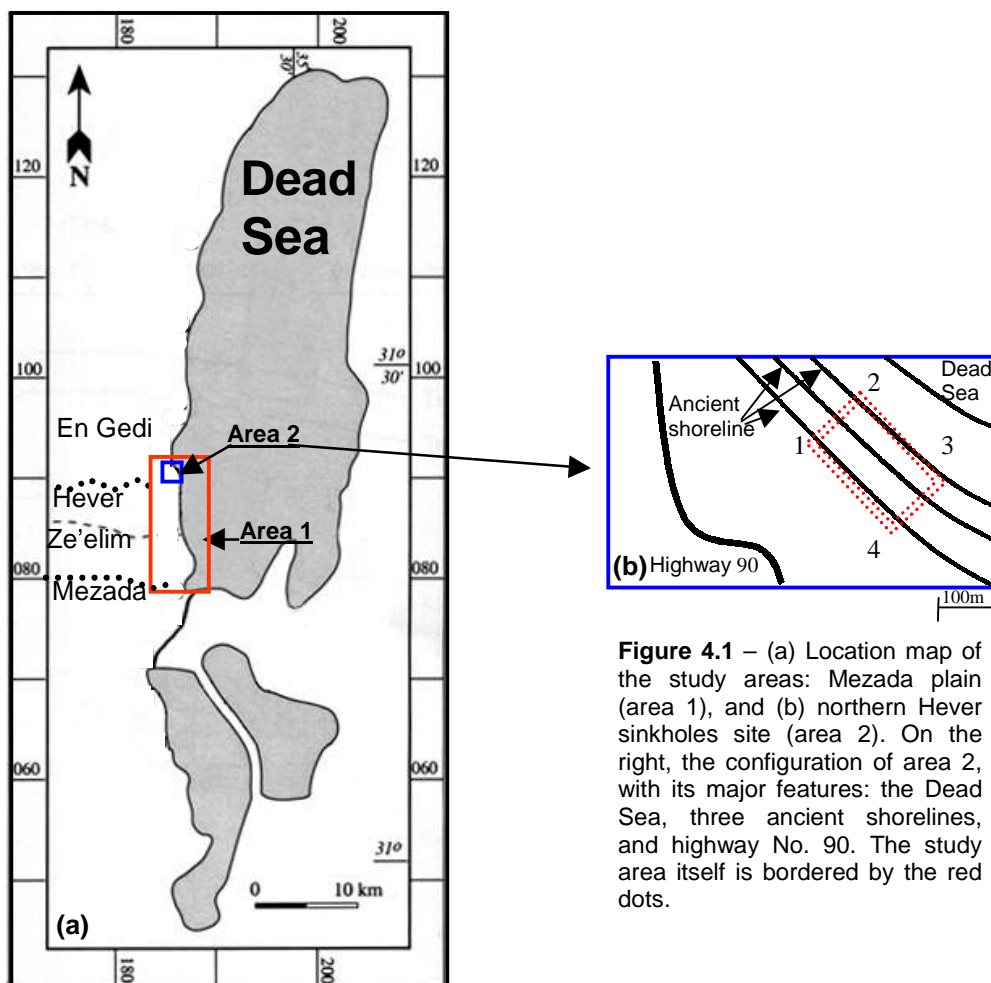

Figure 4.1 – (a) Location map of the study areas: Mezada plain (area 1), and (b) northern Hever sinkholes site (area 2). On the right, the configuration of area 2, with its major features: the Dead Sea, three ancient shorelines, and highway No. 90. The study area itself is bordered by the red dots.

Focusing on area 2, its northeastern and southwestern boundaries are sub-parallel to the current shoreline. These boundaries follow ancient shorelines. The northeastern boundary is distant from the current shoreline by 300m. The southwestern boundary is located 500 m northeast of highway No. 90 (Figure 4.1b). On the last field observation (January 2001), seven sinkholes were identified in area 2 – four of them are solitary and the other five are arranged in two complexes (Uvala). Two of the sinkholes are separate and distinct from the other seven. Each complex consists of a major sinkhole which is tangent, secant or even includes a few smaller sinkholes (Figure 4.2). The sinkholes of area 2 are discussed in further details in section 4.5. (Sinkholes in the studied area).
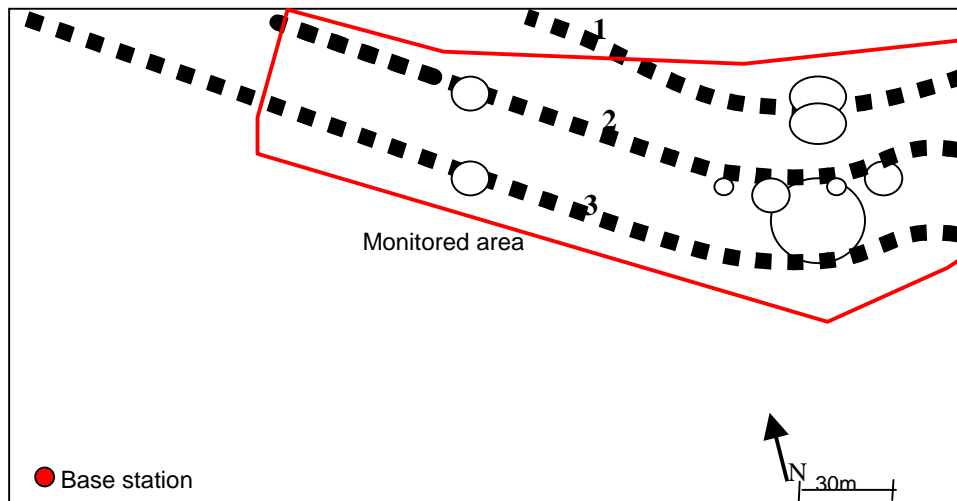
Figure 4.2 - A schematic reference map of the sinkholes (ellipses) and shorelines (thick dashed lines) in area 2. The position of the base station and the boundaries of the monitored area are marked in red.

4.2 Morphology of the area

The elevation of the study area ranges from 14 to 19 meters above the Dead Sea Level, which was measured on December 1999 as –413.18 (DSL99). The elevation of the study area (areas 1 and 2) with respect to the ellipsoid, using the WGS geodetic datum, is between the values (-377) and (-382) meters (measured on 17/01/2000). The monitoring survey measurements were conducted within area 2, but the reference benchmark (the base station) was located outside area 2, on an ancient shoreline, 23 meters above the DSL99.

The relief of the area is inclined moderately, at about 3°, towards the Dead Sea (due north-northeast). The sediments of the ancient shorelines are mounded laterally upon the general slope, exceeding the smooth relief by about a meter. Area 2 covers three of these ancient shorelines (Figure 4.2). Up-slope, between the central shoreline (marked as shoreline 2 in Figure 4.2) and the southwestern one (shoreline 3), the surface is covered by angular pebbles. Between shoreline 2 and the northeastern one (shoreline 1) the slope maintains the same inclination and pebble cover, except to some limited areas were the cover changes to clay and cobbles. These limited areas, which are topographically lower than their surroundings, may reflect dry ponds. The ancient shorelines consist mostly of well-rounded and well-sorted pebbles, in a void-bound honeycombed structure. In places, aragonite laminas cover pebble layers and strengthens the loose structure.

4.3 Local climate

The study areas are located in an extreme arid climate with an annual average precipitation of $70^{mm}/_{yr}$. The annual average temperature is about $24^{o}C$, but in the summer it can exceed $40^{o}C$. The main water contributors are floods, which flash occasionally in the wintertime, and groundwater, which follow the routes of the local aquifers. The low precipitation, low humidity and high temperature impede occurrence of long-lasting standing water.

4.4 Anthropogenic influences

The sinkhole and surface subsidence sites along the Dead Sea shores are subjected to anthropogenic influences in different extent. The anthropogenic influences range from infrastructures (e.g. buildings, fresh water pipes, sewage pipes and roads) to people walking freely on the beach. The study areas (eastern Mezada plain), and area 2 in particular, were chosen to be studied, because of the combination of obvious occurrence of sinkholes and land subsidences as well as minor direct human influences in its vicinity. Other sinkhole sites, like the camping site of Kibbutz En-Gedi, were not included here due to human activities (e.g. gardening and leaking pipes) that directly affect the evolution of the sinkholes. The nearest infrastructures to study area 2, are abandoned greenhouses distant about 200 m southwestern of area 2. These greenhouses were never used, and more important, they do not obtain any watering system. The main road passes about 500 m southwest of area 2, and crosses area 1 trending south. En Gedi Hot Springs are situated about 1 km northwest of study area 2, in the same elevation. Therefore, excess water from the Hot Springs are not likely to reach area 2 as runoffs nor subsurface flow. Another infrastructure, which is located 2 km west of the southern end of study area 1, is the Mezada tourist complex. The influence of the tourist complex, in water means, is limited to a narrow strip that stretches eastwards as Mezada Stream and its surroundings (Figure 4.1). Throughout the two years of field observations, new man made or vehicle made traces, were rarely seen in study area 2. Therefore, the development sinkholes and land subsidence in the study area is mainly due to natural cause. The main parameters that control the sinkholes and land subsidence development are geologic (lithology and tectonic frameworks), hydrogeologic (water horizons and subsurface drainage) and engineering (soil mechanics) influences, whereas the climatic conditions contribute more to the preservation of the area. In this manner, the lowering of the Dead Sea water level, is the only indirect anthropogenic influence.

4.5 Sinkholes in the studied area

In an air photo of the Northern Hever sinkhole site, from 1999 (Itamar and Reizmann, 2000) (Figure 4.3), two sets of sinkholes were identified: a western set and an eastern one. The sinkholes in the western set are aligned with a few sinkholes north of area 2 (two of them appear in Figure 4.3). The alignment of the western set is almost perpendicular to the current shoreline. On the contrary, the eastern sinkhole set shows no alignment with sinkholes outside area 2.

The evolution of sinkholes in area 2 was traced from a series of air photos. Air photos from 1990 and 1992 (Figures 4.4 and 4.5 respectively) show the earliest stages of development in the northern Hever sinkhole site. The beginning of the linear
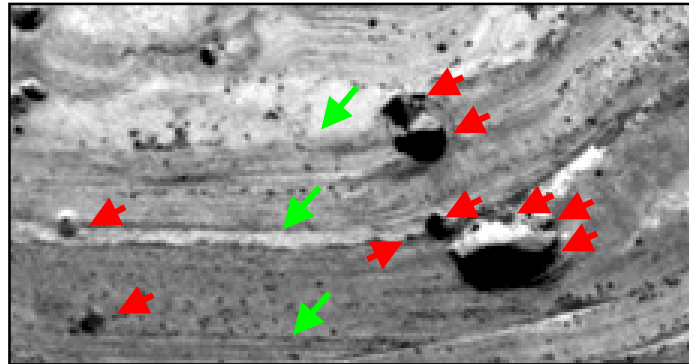
Figure 4.3 - Above: An air photo of area 2, taken on 12/02/1999. The prominent features in the photo are the sinkholes (marked by red arrows) and the ancient shorelines (marked by green arrows). **Below:** A schematic reference map of the sinkholes and shorelines as seen in the air photo above. The characters and numbers given in the map are used as the nomenclature of the sinkholes and shorelines respectively in the next sections.

sinkhole trend can be seen in Figure 4.8, which was taken at 1993. An air photo from 1995 (Figure 4.7) shows sinkholes distribution very similar to the 1999 distribution (Figure 4.8); although the 1995 sinkholes are smaller and fewer then the 1999 ones. A more detailed description of the sinkhole evolution with time, according to air photos and field observations, is given in the next section.

4.5.1 Sinkhole evolution in area 2 according to air photo analysis

The development of the sinkholes in the northern Hever sinkhole site (area 2) as detected by air photos is described in the next pages. The description is given in five stages, from 1990 till 1999. In each page two Figures are presented – the upper one (larger) shows the whole northern Hever sinkhole site (referred as **the northern Hever site**), whereas the lower Figure shows an enlargement of area 2 (referred as **area 2**). All the air photos (Figures 4.4-4.13) are from Itamar and Reizmann (2000). Throughout the five development stages the sinkholes of area 2, have evolved exterior to the Hever alluvial fan. The dark and light elongated features, which cross the air photo sub-parallel to the current shoreline, are ancient shorelines. The ancient shorelines are generally linear in most of the photo, except on the east part where they curve around the alluvial fan.

4.5.1.1 <u>Air photo: 31/08/1990</u>

Northern Hever site
Six immature sinkholes appear in the air photo, two of them in area 2 (Figure 4.4a).
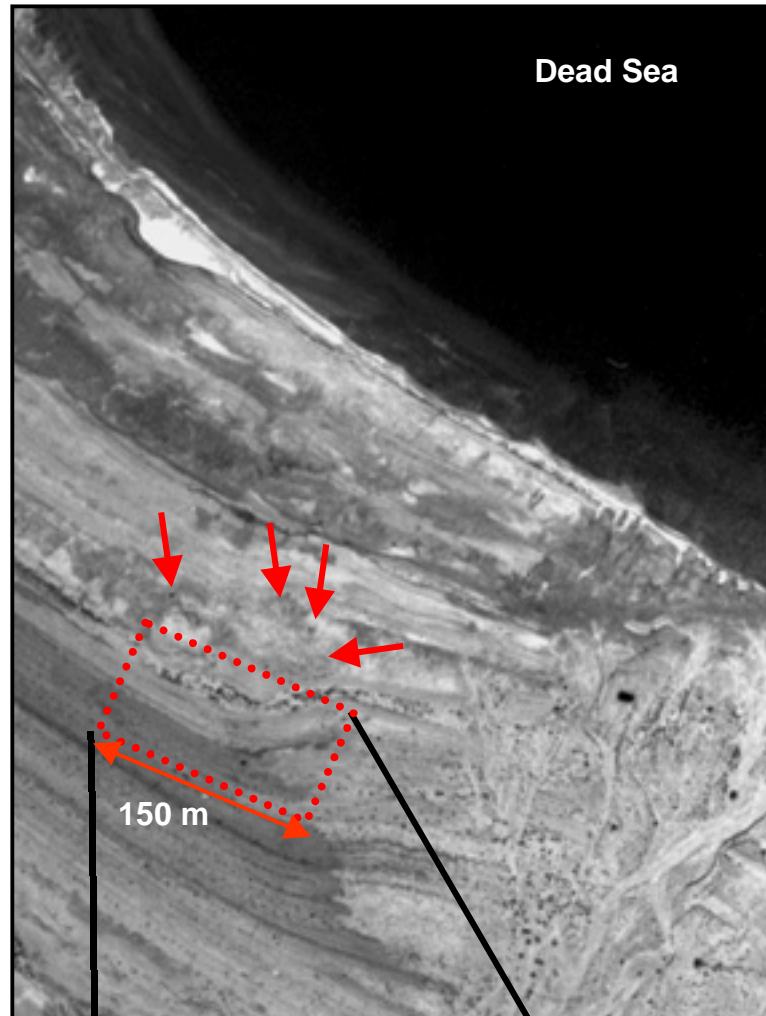
Figure 4.4a - Air photo of the northern Hever sinkhole site, taken at 31/8/1990.

Figure 4.4b –Zooming into study area 2. The red circles mark sinkhole locations.

Area 2
Two of the sinkholes are located in the area 2. These sinkholes, A and G (Figure 4.4b), Are the first ones on the eastern group. They are located along the western margin of the alluvial fan.
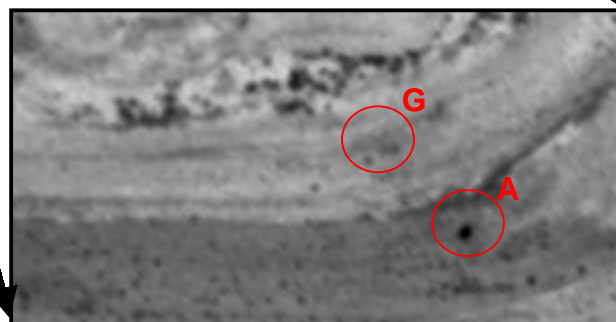
4.5.1.2 <u>Air photo: 26/09/1992</u>

Northern Hever site

A western group of 4 sinkholes starts to develop north of the northwestern border of area 2 (Figure 4.5a). Three of them are aligned (red arrows) and one is located west of the line (blue arrow) Two new sinkholes evolved in the eastern group, north of area 2. The new sinkholes are marked with red arrows.

Shoreline

The shoreline migrated inland by about 15 m, probably as a result of the rainy winter of 1991/1992. The transgressed strip is not completely covered by the Dead Sea water.
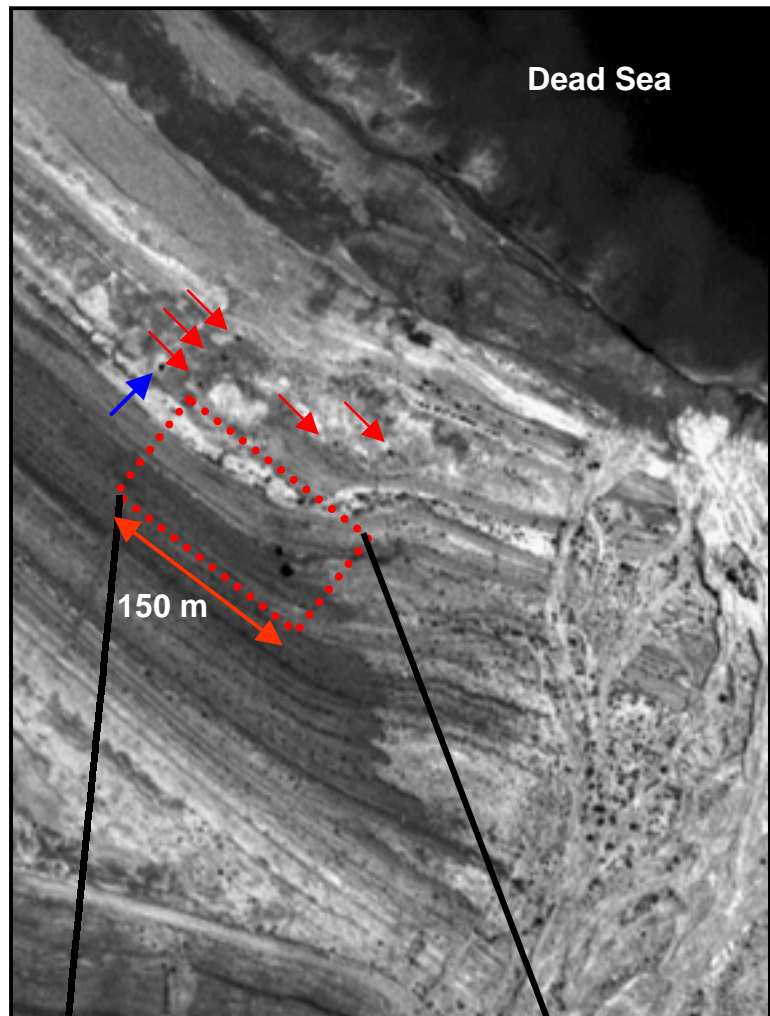
Figure 4.5a - Air photo of the northern Hever sinkhole site, taken at 26/9/1992.

Area 2

Two new sinkholes (C and D) appeared on the western and eastern sides of sinkhole A, respectively (Figure 4.5b). Both sinkholes C and D developed tangent to shoreline 2 along its southern side. A possible surface subsidence is detected around sinkhole G.

Figure 4.5b – Area 2 in 1992, with circles around the sinkholes.
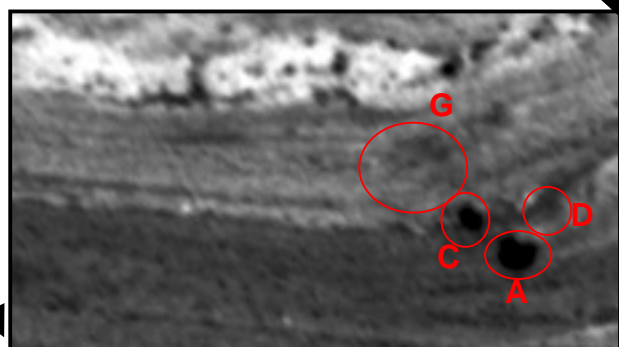
4.5.1.3 Air photo: 26/03/1993

Northern Hever site

Three new sinkholes were formed in the eastern group (red arrows in Figure 4.6a). One sinkhole, on the western group, became smaller, maybe as a result of collapse (blue arrow). The previously detected sinkholes are marked with red circles.

Shoreline

Dead Sea shoreline continues to migrate westward and the transgressing strip is completely covered by the Dead Sea water.
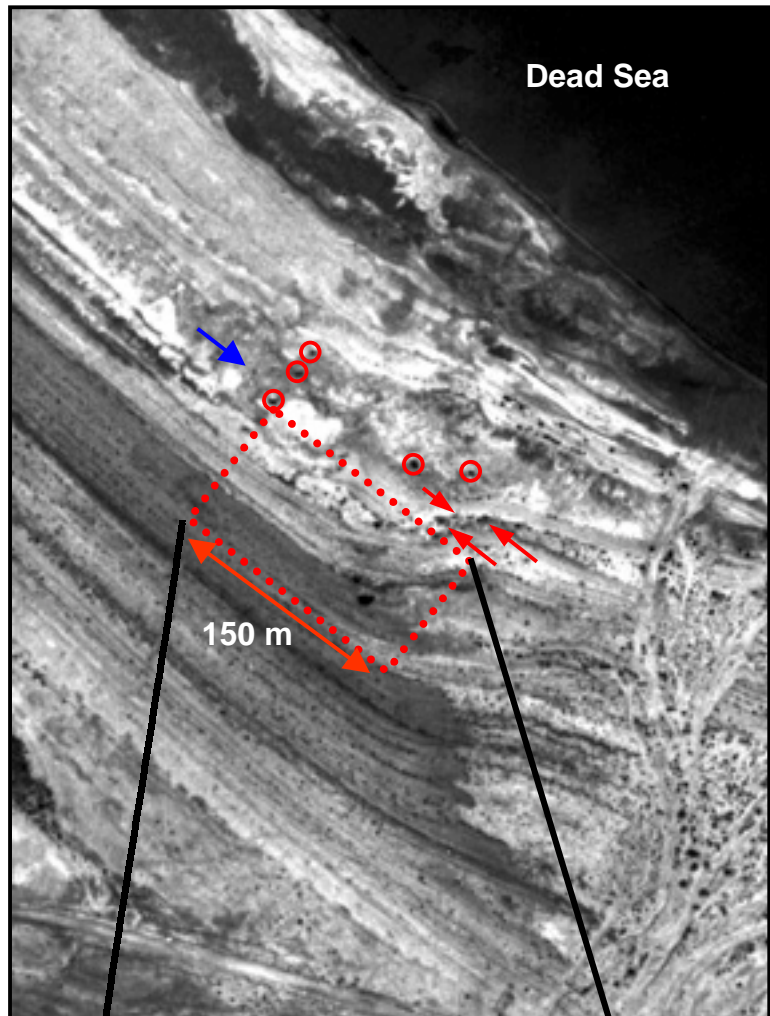
Figure 4.6a - Air photo of the northern Hever sinkhole site, taken at 26/3/1993.

Area 2

The size of Sinkhole D increased (Figure 4.6b). The subsiding area around sinkhole G continues to grow. Another sinkhole, I, had joined the western group, on the same shoreline as sinkhole A, shoreline 2.

Figure 4.6b – Area 2 at 1993, with circles around the sinkholes.
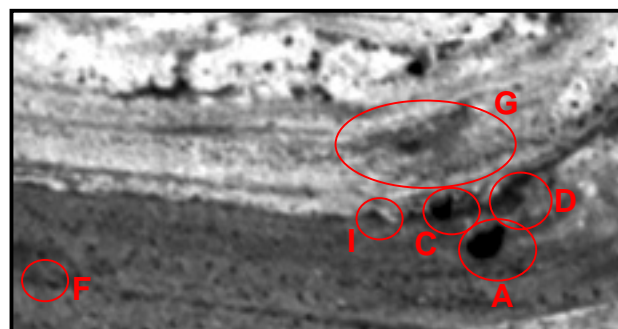
4.5.1.4 <u>Air photo: 22/12/1995</u>

Northern Hever site
In the two years since 1993 the site has developed considerably: In the western group the size of all the sinkholes increased. In the eastern group new sinkholes were formed, and the old ones widened (Figure 4.7a).

150 m
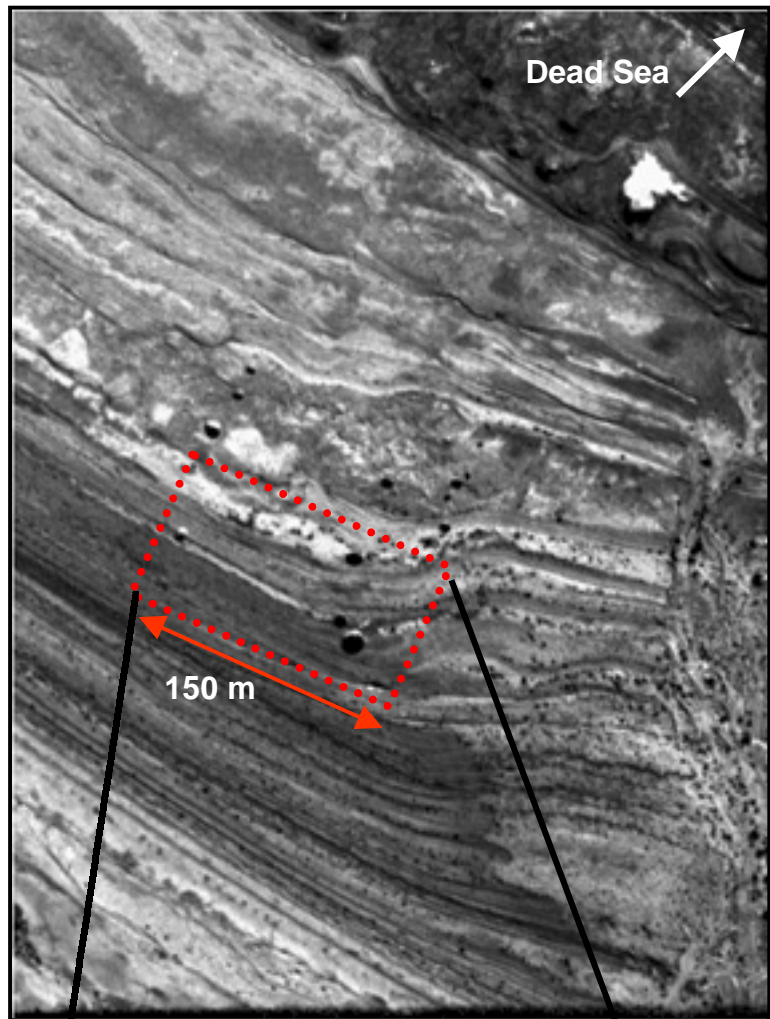
Figure 4.7a - Air photo of the northern Hever sinkhole site, taken at 22/12/1995.

Figure 4.7b - Area 2 at 1995, with circles and arrows pointing at the sinkholes.

Area 2
All the sinkholes grew larger (Figure 4.7b). Two new sinkholes were formed: F, in the western group, along shoreline 3 (the southernmost), and B, in the eastern group, between shorelines 1 and 2 (the northernmost and the central).
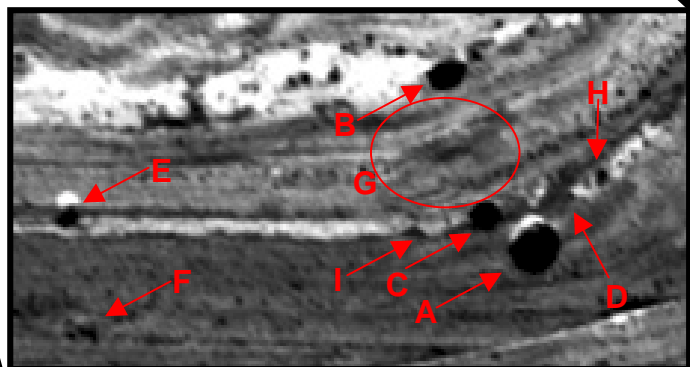
4.5.1.5 <u>Air photo: 12/02/1999</u>

Northern Hever site
Three new sinkholes
evolved, two in the western
group (Figure 4.8a). The
former sinkholes continued
to develop. Two sinkholes
were united in the western
group. The sinkholes in the
northern part of the eastern
group enlarged, and some
of them had united.
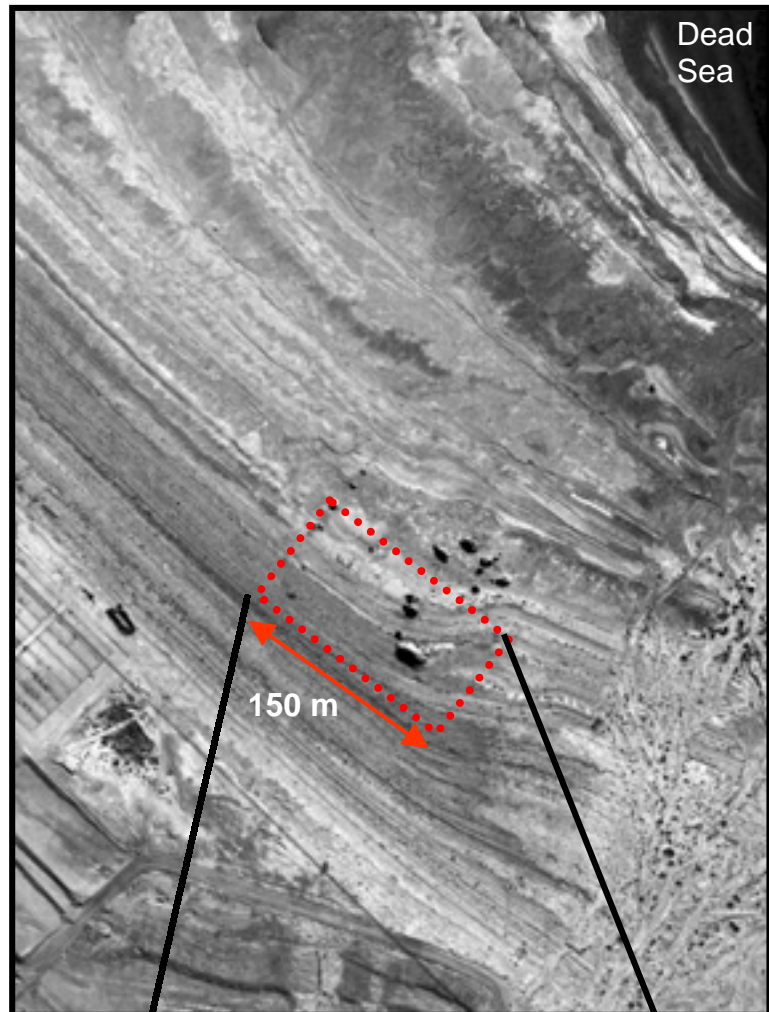
Figure 4.8a - Air photo of the northern Hever sinkhole site, taken at 12/2/1999.

Area 2
The old sinkholes continue
to grow, while new ones
were formed (Figure 4.8b):
Sinkhole H was formed in
the eastern group, east of
sinkhole A, on the same
side of shoreline 2.
Sinkholes B and G were
joined, and together form
the shape of the Figure 8.
Sinkhole A is joined with D
and tangent to C. The
surface subsides around
sinkhole A.

Figure 4.8b – Area 2 at 1999, with arrows pointing at the sinkholes.
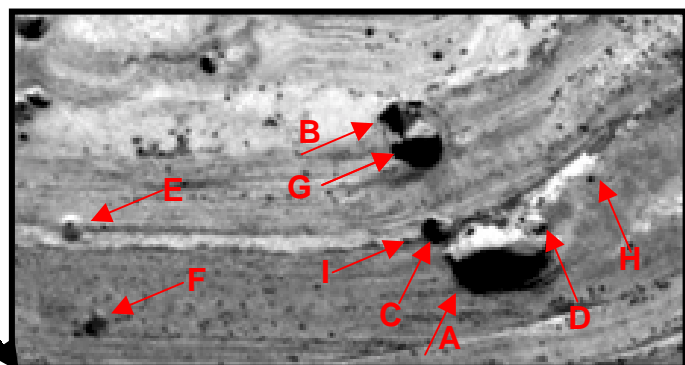
4.5.1.6 <u>Summary of sinkhole evolution in area 2 according to air photo analysis</u>

During the ten years, between 1990-1999, the northern Hever sinkhole site evolved considerably (Figure 4.9). The majority of the sinkholes increased their size since their initial formation (sinkholes I, C, A, D, H, B, and G), although some of the sinkholes had collapsed and stopped developing (sinkholes E and F). Some of the sinkholes were united (C-A-D and B-G complexes). Most of the sinkholes evolved during the latest 5 years, arranged in two sets (an eastern and a western). Surface subsidence occurred around few of the complexes.
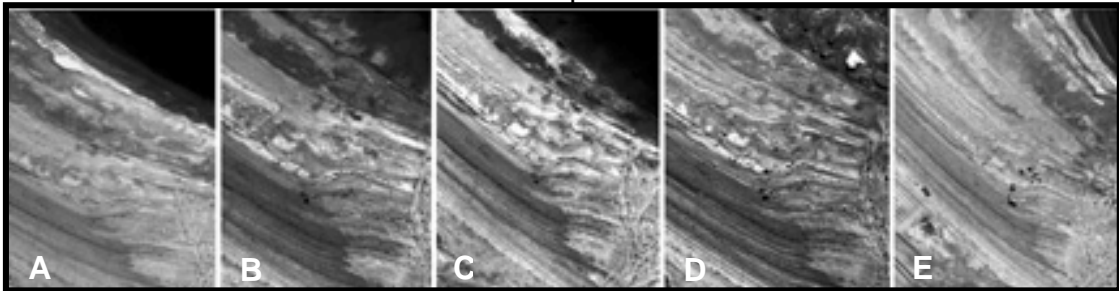
Figure 4.9 - Northern Hever sinkhole site evolution through a 10 yeas period, from 1990 (A), 1992 (B), 1993 (C), 1995 (D), and 1999 (E). The five air photos are presented in the same scale. The most prominent feature is the regression and transgression of the Dead Sea.

4.5.2 Sinkhole evolution according to field observations

Field observations were conducted in study area 2 during a two-year period, between October 1998 and June 2000. Two major features were given extra attention - the sinkholes and the surface behavior. The number, size, and shape of the sinkholes was examined as well as their distribution in the area. The surface behavior was examined in an area as far as 100 m from the sinkholes, on ancient shorelines. More detailed observations were made on the surface behavior around the sinkholes, in search of topographic changes and for fractures.

4.5.2.1 <u>Primary observations – October 1998</u>

There are 7 sinkholes in area 2 clustered in two groups separated by about 100 m from one another (Figure 4.10). The eastern group includes 5 sinkholes: A, B, C, D, and G. The other sinkholes, E and F, comprise the western group.
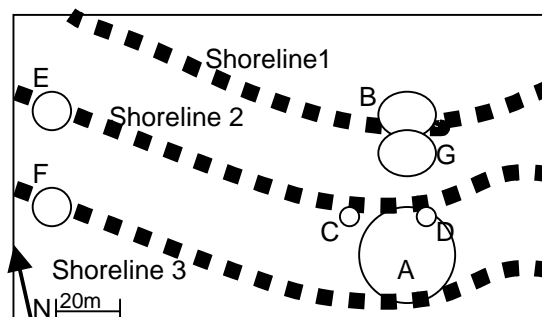
Figure 4.10 – A map showing area 2, in October 1998, with 3 ancient shorelines (dashed lines) and 7 sinkholes (circles).

B-G complex

Sinkholes B and G are secant to each other, and form a complex that looks like the Figure 8 in a plain view. The complex is 13 m in diameter. The joint area is located on shoreline 1, whereas sinkhole B lies north and sinkhole G lies south of the shoreline 1. The surface elevation subsides around B-G complex. The subsidence is accompanied by concentric cracks that appear up to 5 m from the edges of the sinkhole. Some cracks, of small radius, cut through the waists of the complex waists (Figure 4.11). The center of the complex and the imaginary center of the cracks are the same. In places, where the cracks profile is revealed on the walls of the sinkhole, they reach depth of 3 m. Sinkholes B and G are very similar in their steep wall morphology (up to 90°), and in the debris that is mounded on their bottom (which is about 4 m deep).
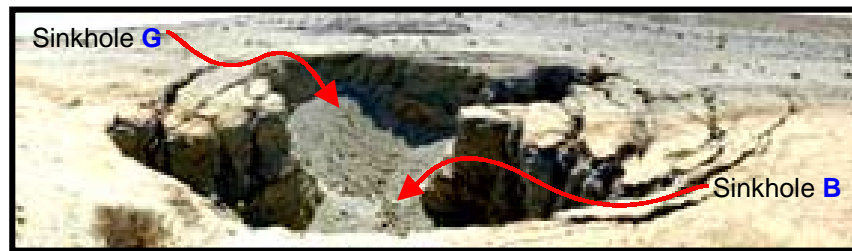
Figure 4.11 - The '8'-shaped B-G complex with concentric cracks cutting through its waists.

C-A-D complex

Sinkhole A is the biggest and most dominant sinkhole in study area 2. It has a bowl shape with a 26 m diameter of (Figure 4.15). It appears round in a plain view, and its northern margin erodes shoreline 2. A schematic cross-section of sinkhole A is shown in Figure 4.12. The morphology of half of the sinkhole (from one of its edges down to its bottom), can be described as a landslide: The toe of the slide lays at the center of the sinkhole, on its bottom, while the head of the slide is at the surface. Therefore, the three-dimensional sinkhole can be described as an axisymmetric rotational landslide.

Sinkhole D was identified in the air photo from 1995 as an independent sinkhole. In the following air photo (from 1999) sinkhole D was united with sinkhole A (Figure 4.12), although their bottoms are not at the same level (sinkhole A is about 3 times deeper than sinkhole D). Relicts of the bordering edge of sinkhole D separate it from sinkhole A.
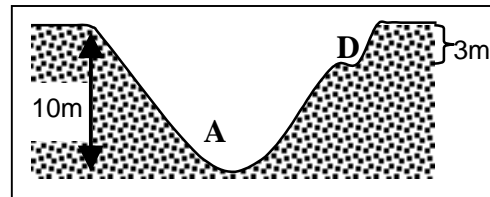
Figure 4.12 - Schematic cross-section of the united A and D sinkholes, in which their bottoms are in different depths.

Sinkhole C is secant to shoreline 2 from the south (upslope). It is a chimney-shaped sinkhole with a 3m diameter. Its depth is about the same as the depth of sinkhole A. Although sinkholes C, A, and D are regarded as a sinkhole complex (Uvala), their interrelations differ. Sinkhole D is united with sinkhole A throughout its entire depth, whereas sinkhole C shares only its upper 2m with sinkhole A.

The western group (sinkholes E and F)

The western group is located about 150 m westward of the western margins of the Hever alluvial fan. It is comprised of two sinkholes (E and F), that are distant 10m

from one another. Sinkholes E and F are located on shorelines 2 and 3, respectively. Both sinkholes are sandglass-shaped, with a diameter of 2.5 m and depth of 2 m. Their walls, which are slanted in an angle between 30°-35°, may be described as an axisymmetric dune slope.

4.5.2.2 <u>Observations – August 1999</u>

Western group
    Sinkholes E and F evolved in a similar way. Their depth increased by 1m, yet, their circular plain view shape, their diameter, and their sandglass appearance remained.

Figure 4.13 – A map showing area 2, in August 1999. Concentric cracks appeared around the western complexes (marked by red dashed lined circles). Sinkholes H and I were formed (marked by red circles).

Eastern group
    Two new sinkholes, H and I, were formed in the eastern group, both south to shoreline 2 (Figure 4.13). **Sinkhole I** is round in a plain view, and is located west of sinkhole A. It is a sandglass-shaped sinkhole, with a diameter and depth of 1.5m. **Sinkhole H** is also round in a plain view, 1.5m in diameter, but is located 5m eastwards to sinkhole A (Figure 4.13). It is a bell-shaped sinkhole and 3 m deep (Figure 4.14).

    An elliptic-shaped surface subsidence had developed around the C-A-D and B-G complexes. The subsidence around C-A-D complex is bounded by cracks and located up to 10m from the edges of sinkhole A. Sinkhole H is located within the subsiding area. The eastern edge of sinkhole H is tangent to the elliptic crack with the largest radius that bounds the surface subsidence. The surrounding cracks around the B-G complex and at its waists continued to deepen and open, while the size of the sinkholes themselves did not change.

Figure 4.14 -A schematic cross-section of a bell-shaped sinkhole (sinkhole H).

    In order to quantify the sinkhole development, a circle of red dots was marked around each of the sinkholes. The marks were painted at a constant distance from the sinkhole edge (10cm-40cm in all the sinkholes except 1.5m around sinkhole H).
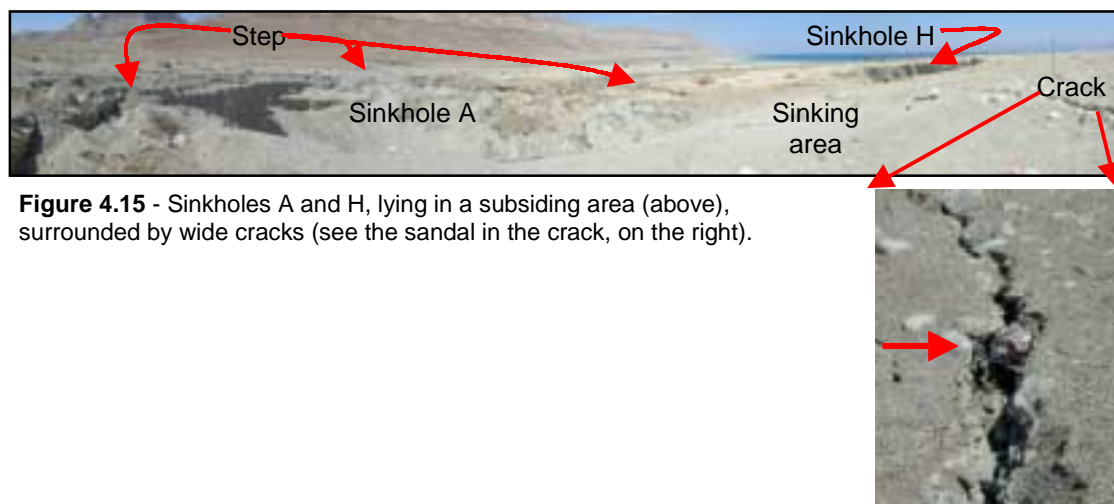
Figure 4.15 - Sinkholes A and H, lying in a subsiding area (above), surrounded by wide cracks (see the sandal in the crack, on the right).

4.5.2.3 <u>Observations – April 2000</u>

Western group
  As in 1999, sinkholes E and F changed their shape in a similar way. The upper 50cm section of their walls had collapsed. As a consequence, the upper 50cm of each sinkhole wall became steeper, whereas the lower section became more moderate in slope (Figure 4.16).
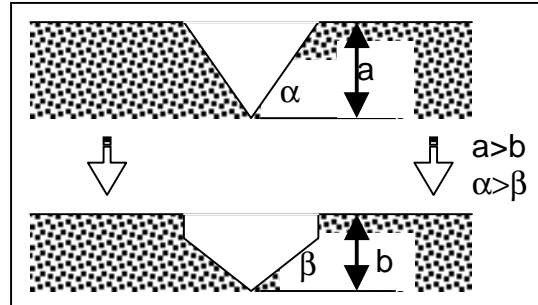
Figure 4.16 - Changes in the shape of the sinkholes E and F.

Eastern group
  The diameter of **Sinkhole A** increased. Along its margins, a 1m step was formed. The subsiding area around the sinkhole extended, and the surrounding cracks extend up to 15 m from the edges of the sinkhole. Crack width exceeds 30 cm in some locations (Figure 4.15).
  Sinkhole H changed its shape from bell-like to a cylinder (Figure 4.17) after its ceiling collapsed. As a result, the depth of the sinkhole decreased. The red marks that were marked 1.5m from the its margins in 1999 fell into the sinkhole. The eastern margins of sinkhole H are located on the circumferential cracks of sinkhole A. Hence, the plain view of sinkhole H is similar to the letter D, with a 4m diameter, and not circular as the other sinkholes. Sinkhole H lies within the subsiding area around sinkhole A, nevertheless, a 1m wide strip between them is uplifted from its surrounding by 30cm.
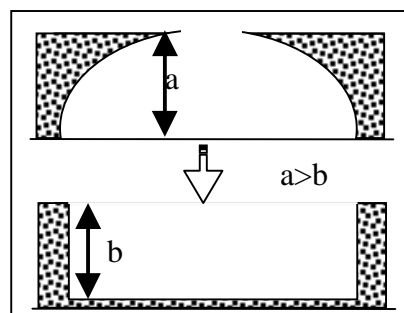
Figure 4.17 - The bell-shaped sinkhole, sinkhole H, collapses and becomes cylinder-shaped.

B-G complex
  Sinkholes B and G grew up to 50 cm around most of their edges, due to collapses. On the southern margin, a 1.5m wide area collapsed. The width of the surrounding cracks widened, and in places new ones appeared, up to 10m from the margins of the sinkholes. Some of these cracks coincide with the concentric cracks of sinkhole A. No new sinkholes had evolved since August 1999, nevertheless, the

existing ones showed development.

4.5.2.3 Summary

During the two years of field measurements (1998-2000), the sinkholes in area 2 evolved in two clusters (eastern and western), separated by 100m of undeformed area. The eastern cluster developed faster both in dimensions of the sinkholes (sinkholes E, F, C-A-D complex, and B-G complex) and in their number (sinkholes H and I were formed).

Field observations indicate that each sinkhole affects its surrounding area in the form of cracks and surface subsidence. Different sinkholes influence their surroundings at different extent (vertical and horizontal). Nevertheless, the deformed area surrounds the open of the sinkhole at the surface – deformation ring (Figure 4.18). The deformation ring is hardly observed around the western sinkholes (E and F), contrary to its prominent appearance around the eastern cluster. On the western cluster, the deformation rings partially overlap in places. These interactions complicate the nature of the surface deformation, and forms uplifted zones within sinking areas.
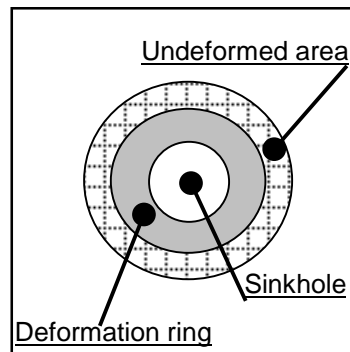
Figure 4.18 – A schematic plain view of a sinkhole surrounded by a deformation ring. The width of the deformation ring varies in different sinkholes.

5. Data collection and processing

In this research we monitored and characterized the surface deformation along the Mezada plain, on the western shore of the Dead Sea. The features in focus are surface deformation induced by sinkhole activity in the northern Hever alluvial fan (area 2), and wide surface subsidence across the Mezada plain (area 1). Sinkhole activity in area 2 was monitored in six measurement sessions, using two types of geodetic techniques: space-based positioning (GPS) and terrestrial-based positioning (EDM) (see Table 5.1). Four sessions of the field measurements were carried out using kinematic GPS, both in real time and post processing modes. Two additional sessions were carried out with the **E**lectronic **D**istance **M**easurement (**EDM**). The two work methods provide elevation data for discrete points in the field. The elevation data was used in chapter 6 to surface deformation in the study area 2. The surface subsidence, in area 1, was monitored using the InSAR technique. Twelve (12) scenes were selected, spanning periods of 3 to 71 months between 1992 and 1999. The scenes are about 100x100 km^2 each taken from the InSAR descending track frame of 2979.

Date	Measurement points	Measurement type	Equipment
4/5/1999	415	GPS-RTK	Trimble 4000 receivers
22/12/1999	355	GPS-Post Process	Z-12 and Z-surveyor
17/1/2000	460		receivers
26/6/2000	357		
27/2/1999	28	EDM	SET2CII (Sokkia)
19/3/2000	28		

Table 5.1 – Summary of the technical details of the six measurement sessions conducted in study area 2.

5.1 Measurements with GPS and EDM

One of the problems that arise during a geodetic survey with GPS or EDM equipment is locating the measured points in an array that will give the highest accuracy while producing the map. Therefore, in order to measure the surface in a way that all its features will be pronounced, an array of points was selected to be measured, according to the observations on the surface deformation. Some open questions led to the decision where to measure: (1) Does a sinkhole influence its surrounding topography? (2) If there is such an influence, how does the surface deform near a sinkhole? (3) What is the width of the deformed area? (4) Are ancient shorelines leveled as they are supposed to be? and (5) Is there any topography changes in the areas that seem to be undeformed in the air photos and in the field observations?

The surface features that received extra attention during the measurements were: **sinkholes** – their circumference and surroundings; **ancient shorelines** – along the three ancient shorelines in the
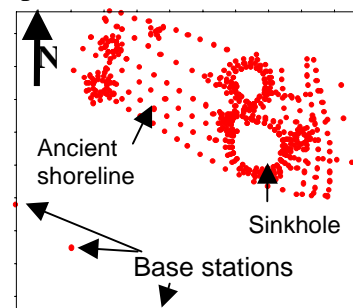
Figure 5.1 – Map showing the 415 points measured with the RTK system, on 4/5/1999. The measurements were made from the most western base station. The other two were used for calibration.

study area; and **the intermediate zone** – between the two clusters of sinkholes (Figure 5.1).

In order to achieve a high level of measurement, repeatability some benchmarks were built in the study area (area 2). Small flags marked the margins of the study area and 28 fixed points were built by placing pipes in the ground. The pipes, each 50 cm long, were placed vertically in the ground in a cross pattern across each of the four major sinkholes (Figure 5.2). Red dots were marked on the surface around each sinkhole, at a constant distance from the sinkhole margins (Figure 5.3). The 28 fixed points were used during the EDM sessions as the only measured points and during the GPS sessions as reference points. Additional points were measured during the GPS sessions around the sinkholes, along the ancient shorelines and between them. The rest of the GPS measured points were chosen during the session.

Figure 5.2 - location of the fixed **EDM** measurement points (the stars) relatively to a sinkhole and an ancient shoreline (the dotted line).

Both geodetic systems, GPS and EDM, require the utilization of a base station with a fixed and stabled location. The base station location was established 300m away from the study area, 5m uphill, on an ancient shoreline. It was fixed by inserting a 1m-iron rod into the ground. Two additional secondary base stations were established 50m and 100m away from the first one, along the same ancient shoreline (Figure 5.1). The secondary base stations were established in the same method as the first one and were used for calibration at the beginning of each measurement session.

EDM

The 28 fixed points measured by EDM were placed at distances of 2m and 4m from the edge of major sinkholes. Half of these points are located on ancient shorelines (Figure 5.2).

GPS

A typical GPS measurement session includes the measurement of about 400 points. The measurements were made in three circles around each sinkhole. The smallest circle is the red dots, which are marked on the ground near the margins of the sinkhole. Two additional circles were measured 2m and 4m away from the margins (Figure 5.3). Each of the three ancient shorelines in the area 2 was measured with at least one series of points, distant 10m from one another. Measurements were made also, between the clusters of the sinkholes and the ancient shorelines, in roughly equally spaced points.

Figure 5.3 - Schematic map showing the location of the **GPS** measurement points (the dots) relatively to a sinkhole.

5.1.1 Surveying with Kinematic GPS

Four GPS campaigns were conducted during the two-year period of this work, from October 1998 till June 2000. The first session of measurement was carried out on 4/5/1998, using the TRIMBLE 4000 RTK system of the Geophysical Institute of Israel (GII). The raw data was downloaded from the receivers with the TRIMAP software in the GII. The three other sessions were carried out in the post-processed kinematic technique on 22/12/99, 17/1/2000 and on 26/6/2000. In these measurements two type of ASHTECH receivers were used, the Z-12 and the Z-surveyor, which belong to Tel Aviv University and to Mr. Shmuel Grossman, respectively. The raw data was downloaded fr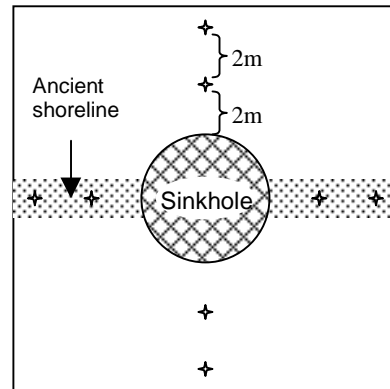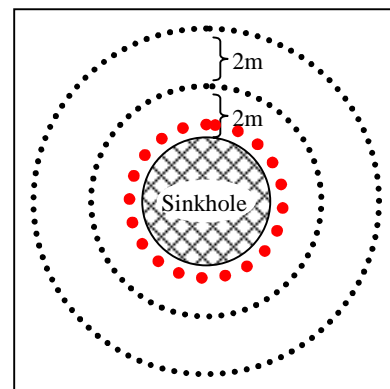om the Z-12 receiver with the CGHOSE software and from the Z-surveyor receiver by the Ashtech software. Data processing was conducted using the Ashtech software of Mr. Grossman.

A surveying typical day comprised of several procedures, i.e., emplacement and initialization of the reference station, initialization of the roving receiver, and surveying. Usually, the measurements did not go smooth due to technical problems. Nevertheless, at the end of the surveying day, the collated data was ready for the computer processing. The following paragraphs describe these components in more details, noting some differences between the RTK GPS and the Post Processed Kinematic (PPK) GPS.

5.1.1.1 Receivers Initializing

At the beginning of a surveying session both the base and the rover receivers should be initialized in order to work synchronically.

Base station

The basic components of the reference station, whether using the RTK or the PPK system, are the base receiver and a geodetic GPS antenna. **The GPS antenna** is emplaced upon a leveled Tripod and Tribrach, which are located exactly above a previously measured geodetic benchmark. After the antenna is mounted its slanted height is measured from the benchmark. After connecting **the base receiver** to a power source (a car battery in this case) and turning it on, some details should be configured in order to define the surveying type that will be practiced. The configurations consider the system components and the data processing. **The system components** defined are the parameters of the antenna: its type, height and position (the previously known geodetic benchmark). In **the data processing** configurations some selections should be made. The surveying technique is defined as post processed or real time, and whether it will be Static, Kinematic or Differential. Then the geodetic datum, on which the positioning calculations will be based, is defined. After choosing the units (metric system or other) for the measurements, some limit values are for the receiver readings. The maximum **GDOP** (the constellation of the satellites is sight), still reliable, is usually is set to value 4. The elevation **Mask** is the minimum angle above the horizon to receive readings from the satellites. This value is usually between 10°-13°. The period of time in which the receiver acquires transmissions from the satellites before it marks a reading is the **Epoch interval.** Epoch interval values can range from 0.5-900 seconds.

With these configurations the post-processed base station is initialized, while the RTK base station lack some components. During an RTK survey, a constant radio contact should be maintained between the base and the roving stations. Therefore the additional equipment in the RTK base station is a radio antenna, a radio

transmitter/receiver, an amplifier for the radio transmissions, and an additional Power source. Special cables interconnect the components of the base station.

Rover station

In both systems, the RTK and the post processed kinematic, the initialization steps and the components of the rover station are very much similar to those of the base station. The base and the rover stations of the RTK system communicate continuously during the survey, through radio link. Therefore, the epoch intervals of the measurements are synchronized. This is not the case in the post-processed system, were the two stations work independently in the field. Hence, the base and rover stations must be initialized with the same defined epoch interval.

The difference between the base and rover stations lays in their component's size and weight. Most of the

Figure 5.4 - The GPS rover receiver (Ashtech's Z-surveyor) carried on a strip during the measurements (from ASHTECH website).

components of the rover are smaller and lighter, in order to ease their portability. The GPS antenna is attached to a pole, rather than to a tripod. The pole can be carried by hand and located at each measured spot. It can also be attached to a backpack while roving with the RTK system. The GPS receiver is placed in the backpack (RTK), or on a strip (Post Processed) (Figure 5.4). The receiver batteries are placed in the backpack. The RTK rover station has additional radio equipment. The radio transmitter/receiver and its power source are placed in a backpack, to which the antenna is attached, on a pole. Special cables interconnect the components of the base station.

5.1.1.2 Surveying

The survey itself is the simplest part of the job. The measurements are preformed as follow: The surveyor arrives to the location that will be measured and places the GPS antenna on the spot. When the antenna is leveled, the surveyor stands still and punches the button on the receiver that starts the measurement. The receiver collects the signals from the satellites along a previously defined time interval (few epochs), and tags the measured spot with a serial number. When the measurement epochs end, the receiver signals the surveyor to move to the next spot, where the same procedure is repeated. The receiver calculates the position not only in the specific points, labeled by the surveyor, but also along the trail between them. The data about the trails can be used, in a post processing calculation, to give additional information about the studied area.

Measuring points with running serial numbers is one of the basic options of system. The RTK system has additional navigation and geodetic options, such as navigation to specific points; calculating the intersection between two different vectors; calculating intersections between two different circles, given their center location and radius. In addition, several shapes can be defined, by marking equally spaced points on the surface, i.e. a line, an arc, a slope, and a grid of points.

5.1.1.3 Typical problems during the field work

During a typical fieldwork the surveyor is confronted with some problems. The problems can originate from user errors, technical errors of the instruments, and external obstacles. **User errors** can be technical, i.e. connecting the system components wrongly, or measuring while the GPS antenna is not properly leveled. Operational user errors can originate from imprecise initialization of the receivers, i.e. defining the wrong geodetic datum; defining the wrong height for the GPS antennas; choosing the wrong surveying technique (differential, kinematic, or static); unsynchronized operation of the post-processed receivers, by defining different epoch intervals for the base and rover stations. **Instrumental problems** can usually arise from the technical conditions of the equipment. The problems can originate either from weak batteries, providing voltage below the needed threshold, shaky cable connections, or that the memory disk of the receiver had reached its full capacity already. **External problems**, which affect the GPS and the transmissions, usually originate from either poor GDOP, or bad visibility of the satellites, and radio disturbances (in the RTK operation).

5.1.2 Surveying with EDM

Two EDM sessions were conducted, using the SET2CII (Sokkia) of the Geological survey of Israel (GSI). The first measurement session was carried out on 27/2/1999 and the second session on 19/3/2000. The raw data was written in the field in a notebook.

5.1.2.1 Setting up the instrument

The EDM apparatus is placed on a leveled tripod, which is located exactly above a previously measured spot (the base station). After the apparatus is switched on, it is initialized by a horizontal and a vertical turn. Some pre-surveying measurements should be conducted in the beginning of every session. These measurements directly affect the accuracy of the EDM. **The Height** of the EDM and the reflector above the ground is configured as well as the **weather conditions** - the barometric pressure and the temperature of the air.

5.1.2.2 Placing the reflector

The EDM measurements were conducted above 28 fixed points. A 50cm long and 10cm wide pipe was placed in each point, for enabling measurement repeatability (see section 5.1). 10 cm of the pipe was left above the ground. The reflector was screwed in the center of a plastic cup, filled with glue (Figure 5.5). During the measurements the reflector gadget was placed, leveled, on each pipe, facing the EDM.

Figure 5.5 - the reflector placed on one of the pipes.

5.2 InSAR processing (based on Baer et al., 1999)

InSAR data in this study was processed in a few steps. At first, the raw data (acquired by the ERS satellites) was sorted and the frame that covers the western shores of the Dead Sea was chosen. Then a topographic model was calculated from a basic reference topography model, and at least two InSAR images (of short time interval). This model was used for producing topography-free interferograms, which are the final product.

Twelve images were chosen from the frame 2979, for the study (Figure 5.6). The images were taken in dates that span from 11/6/1992 until 21/3/1999, in descending track orbits. Twelve of them image an area of 112x100 km^2, and one images only 100x100 km^2. Generating interferograms from a group of images demands sub-pixel correlation between all images. To achieve such correlation, a reference ("master") image was chosen from the group (the red triangle in Figure 5.6); the rest of the images were correlated to the master image. The master image is located, roughly, in the center of the group, according to the orbital location of the satellites. The perpendicular baseline is the vertical difference between the master and
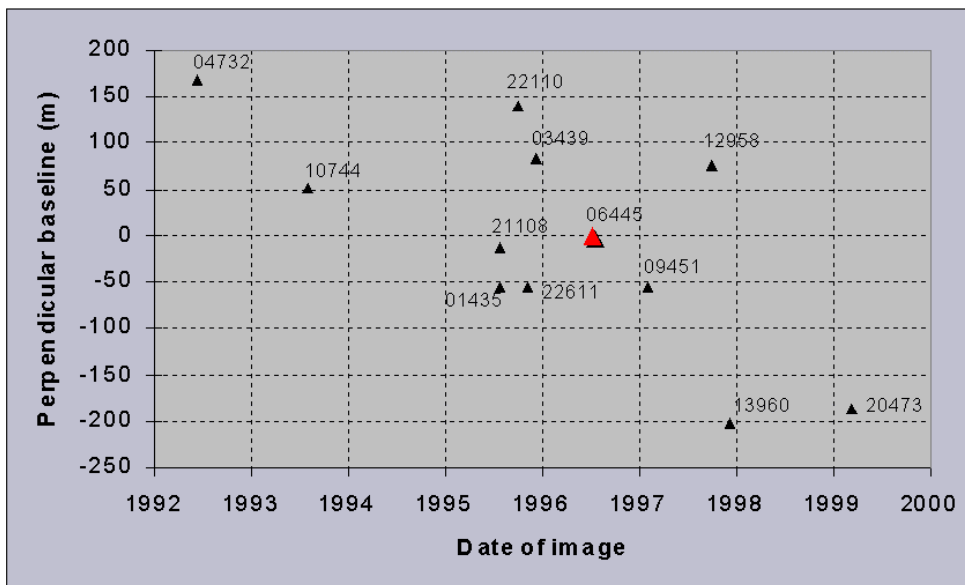
Figure 5.6 – Twelve orbits of the two ERS satellites, used for creating the 2979 frame. Each orbit is marked by a triangle and its serial number. The master image (06445) is marked by a red triangle. The horizontal axis represents the time when the image was taken. The vertical axis represents the offset between the different orbits, in meters, parallel to the earth surface (Baer et al., 1999).

the slave image trajectories. All the perpendicular baselines between the satellite orbits, were calculated with respect to the master image (orbit 06445), hence the master's perpendicular baseline is zero. By finding the azimuth and range of three points that appear on all the images, and calculating their offset from the master image, the images were matched. The calculations were made by using an algorithm that is part of the Stanford/Jet Propulsion Laboratory Interferometry processing package. The result is a complex image whose phase component appears in the interferogram. The phase appears in 2π cycles of colors ("wrapped"), without any absolute value (Figure 5.7).

Figure 5.7 – One cycle (fringe) of colors, standing for one cycle of the phase change (2π).

The topographic model for the specific frame of work is calculated, based on the Gtopo30 Digital Elevation Model (DEM) of the USGS. This DEM is a 1km grid of points on the earth, in a three-dimensional positioning, on a global reference frame. To produce a finer topographic model, interferometric pairs are stacked on the DEM. The most suitable pairs of images for the topography model are those that have the longest perpendicular baseline (Figure 5.6) that still enables the phase unwrapping (resolving the integer number of 2π cycles). The perpendicular baseline difference between the two orbits that form the topographic interferogram, is inversely proportional to the ambiguity height (the elevation change required to alter the phase difference by one cycle). Therefore the pairs with longer perpendicular baseline are more sensitive to topography (Rosen et al., 1996). Moreover, Tandem pairs, taken only 1 day apart, are preferred because they include minimal surface deformation.

Topographic effects may obscure surface deformation on the change interferograms. In order to reduce the topographic effects the pairs with the shortest perpendicular baselines are chosen. Figure 5.6 shows the perpendicular baselines and the satellite orbits that were used in this study. Figure 5.8 shows the selected change pairs on a time scale, showing that different interferograms span over different time periods (discussed in the Results chapter). To form topography-free double-differenced interferograms the topography model is subtracted from the change interferograms. The subtraction is done after both the topography interferogram and the change interferograms are scaled by the ratio of their perpendicular baselines to 100. The result is rewrapped to get the double-differenced interferogram. The selected frame (2979) images a rugged area, with a topography that extends from below –400m and exceeds 1600m. Fortunately, the study area lies on the Dead Sea shores, where the elevation difference is less than a hundred meters. Therefore, the study area is regarded free of topographic influences.

2979 frame
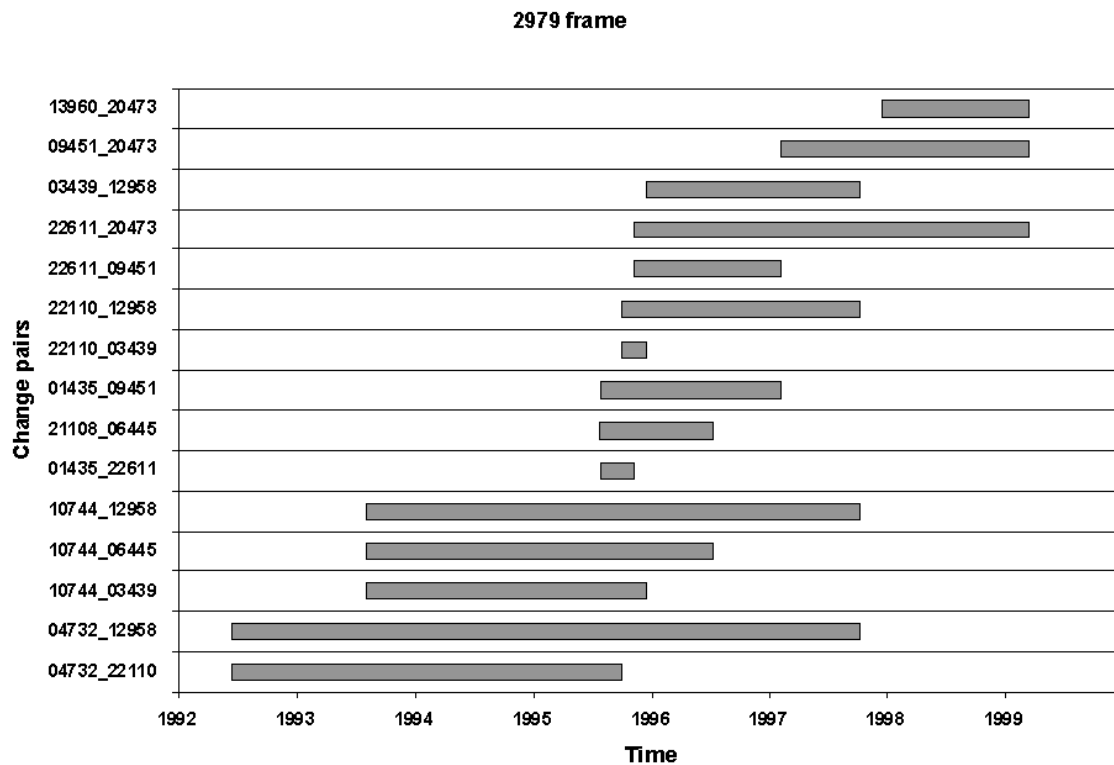
Figure 5.8 - The selected change pairs of the interferograms, on a time scale.

6. Results

In the following pages the results of the different geodetic methods are presented from the large-scale area (the InSAR measurements) to the small-scale area (the GPS measurements); also included are the EDM calibration measurements of the GPS.

6.1 InSAR results

Following the above procedures described, 13 interferograms were selected from the 2979 frame. This frame was imaged by both the ERS satellites in a descending orbit (from the north southwards) that covers most of the Dead Sea shores (Figure 6.1). For generating the topography model, the following two pairs of images were stacked on the Gtopo30: (1) an interferogram made from orbits 21108_2979 and 01435_2979, imaged one days apart, with a perpendicular baseline of 42 m; and (2) an interferogram made from orbits 22611_2979 and 03439_2979, imaged 35 days apart, with a perpendicular baseline of 138.74 m (Figure 5.6).

The thirteen double-differenced (topography free) interferograms were generated by unwrapping, scaling, and subtracting the topography model. The interferograms cover different time periods between 11/6/1992 and 21/3/1999. While choosing the pairs for the double differenced interferograms, short baselines were preferred, in order to reduce topographic influences (shorter than those of the topography model pairs).
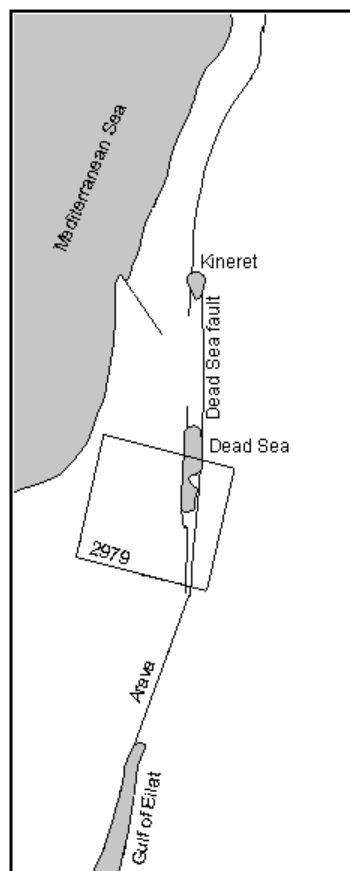
Figure 6.1 – Location map of the 2979 frame.
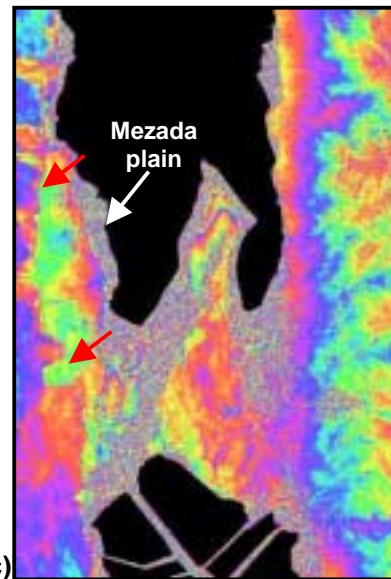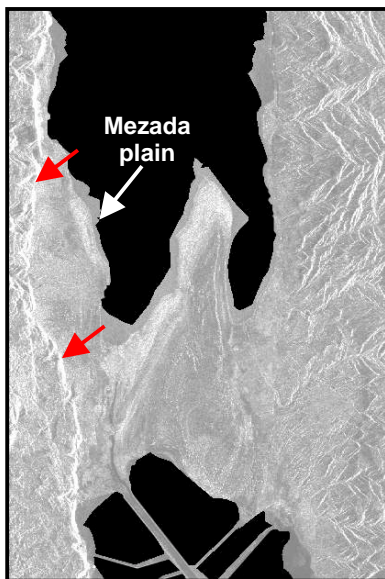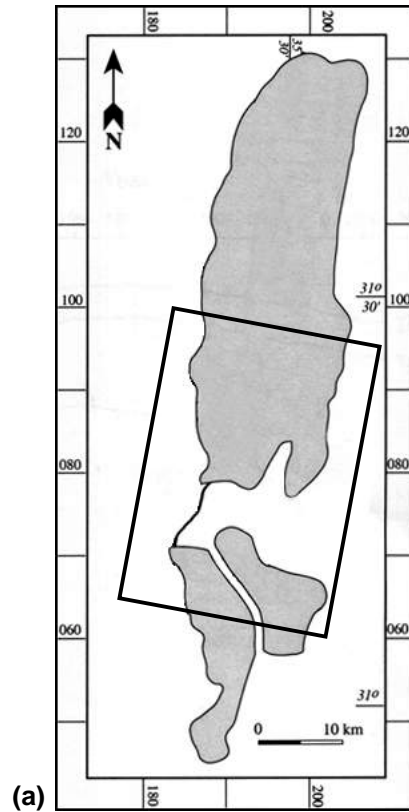
Figure 6.2 – (a) Location map of part of the 2979 frame that covers the central section of the Dead Sea. (b) Average amplitude image generated for the same section of the Dead Sea. The land shows in grayscale colors, and the Dead Sea is blackened. Although the amplitude image is not a topographic map, prominent topographic features can be identified. One of these features is the cliff (marked with red arrows) on the western shores of the Dead Sea. The cliff can be distinguished on the 13960_20473 interferogram (Figure c), despite the topographic corrections that were done during the data processing. Fortunately, the studied area 1 lies east of the cliff, in the Mezada plain, which is almost free of topographic changes.

Some areas on the 2979 frame are characterized by very high topographic gradient, i.e. the cliffs and mountains both east and west of the Dead Sea shores. In some of the double differenced interferograms these topographic features were not diminished (Figure 6.2). However, the topography of the studied area is almost flat, with elevation differences less than 100m. Hence, the observed interferometric fringes are mostly due to surface movements.

The possibility of horizontal movements was examined by comparing the interferograms generated by the eastward-viewing ascending path orbits with those generated by the westward-viewing descending path orbits (Baer et al., 2000). In all cases, the color order within the deformation fringes in a certain area, is similar for the two paths, inferring that the InSAR-detected deformation is primarily due to vertical movements. Taking into account the radar wavelength (56.5 mm) and incidence angle (23º), one fringe cycle represents about 31mm vertical displacement.

This part of the research focuses on the eastern margins of Mezada plain, a wide and elongated coastal strip between Hever creek in the north and Mezada creek in the south (Figure 4.1). The interferograms of study area 1 were analyzed in order to detect the position of the ground surface. The analysis was intended to identify changes in three of the sinkhole sites that were documented by Itamar and Reizmann (2000), (Hever north, Asa'el and Ze'elim). An additional subsidence site that was identified at the tip of the Hever alluvial fan - the Hever delta site (Figure 6.3). Part of the analyzed interferograms are presented in Figure 6.4. The interferograms show the changes of the surface elevation in six different time ranges, spanning between 1992 and 1997.All the interferograms presented here are comprised of both on land and off shore areas. The area on the left-hand side of the interferogram is the Dead Sea shores that is the main focus of this study. On the right-hand side, the Dead Sea surface came out decorrelated in the original interferograms. Meaning that in areas where the surface had changed dramatically (e.g. the Dead Sea surface or the *terra nova*) between the two images that make the interferogram the comparison is impossible. Therefore the Dead Sea surface was blackened. The

Figure 6.3 – Location map of the subsiding area identified in the Mezada plain.

blackening was done according to the correlation border of the 'slave' image of each of the interferometric pair. The red line represents the shoreline on 21/3/99, the most recent shoreline that was imaged (based on the image 20473_2979).

In general, the wide coastal strip of study area 1 looks from the interferograms, as a series of local surface depressions. More detailed analysis of the major surface depressions in four sites is provided in the following paragraphs. The depressions were analyzed from the north southwards: Hever north, Hever delta, Asa'el and Ze'elim (Figure 6.3).

6.1.1 Northern Hever site

The northern Hever subsidence site is located on the northern Hever alluvial fan, stretching parallel to the shoreline, in an east-west direction (figure 6.5). The subsidence site is about 700m long and 400m wide, bordered by the En-Gedi SPA in the northwest and the northern Hever alluvial fan in the southeast. The northern Hever sinkhole site is located along the margins of the surface subsidence, on its eastern end. The whole area is subsiding northwards, towards the Dead Sea. The northern part of the area is subsiding faster than its southern part. The total subsidence reaches values of 3cm (Figures 6.4a and 6.4b, over 3 and 15 months respectively). However, on the rest of the interferograms in Figure 6.4 the entire site is decorrelated, and therefore no information can be inferred.

6.1.2 Hever Delta site

The Hever delta subsidence area is located in the center of Hever alluvial fan (Figure 6.5). The subsidence has a bull's-eye shape, stretching along the shoreline. The center of the subsidence is almost round, with a radius of about 100m, (best
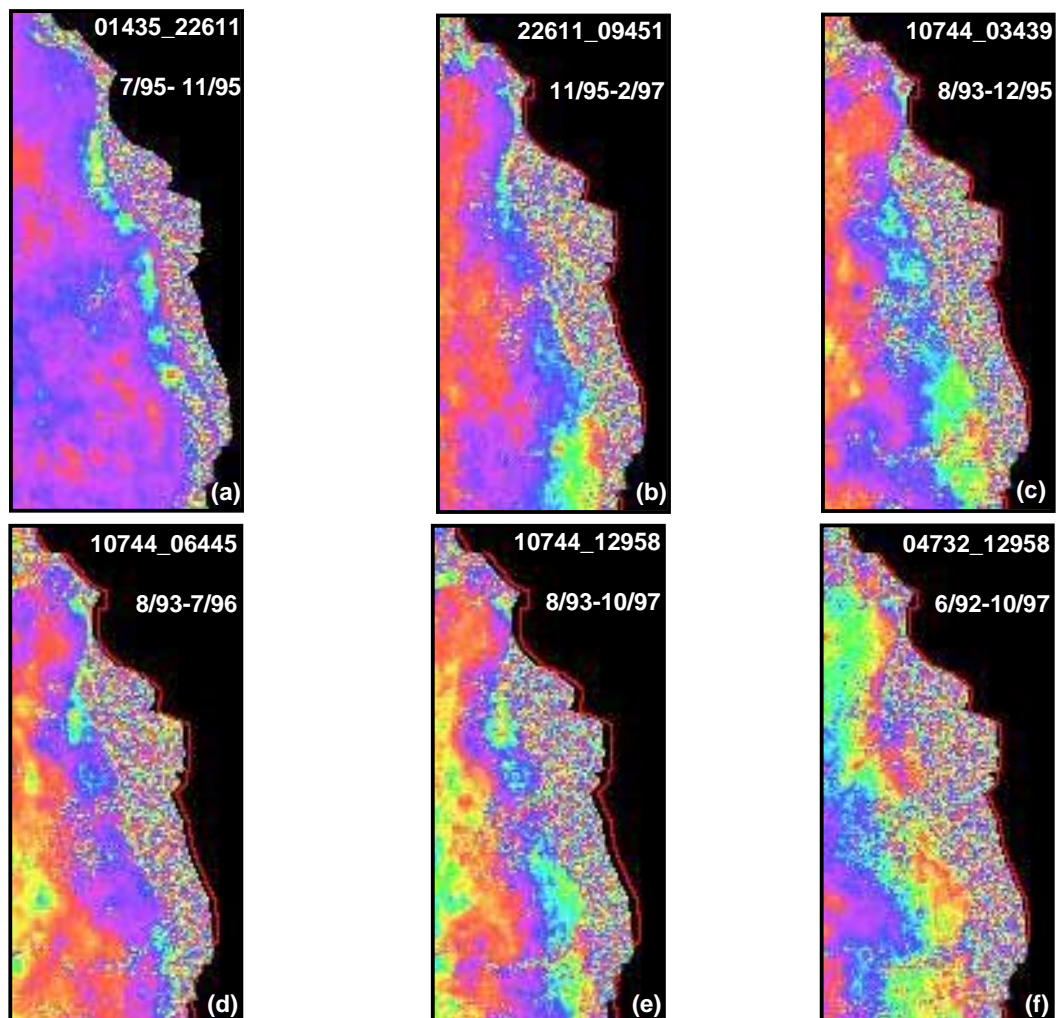
Figure 6.4 – The Mezada plain in six of the scanned interferograms. The interferograms span between 1992 and 1999 on different time periods: 3.42 months (a), 15 months (b), 28.41 months (c), 35 months (d), 50 months (e), and 64 months (f). Each of the six interferograms is subdivided into three areas: on the right (east) the Dead Sea, in black; on the left (west) the correlated area; and between them the decorrelated area.

viewed on Figure 6.4c, an interferogram over 28.41 months). This subsidence was identified in all the interferograms, with he same center location (the same pixel). In most of the interferograms the subsidence is concentric except on Figure 6.4f where the eastern side of the subsidence is in decorrelated. In some of the interferograms (e.g. Figure 6.4d) the subsidence is wider along its western side.

The amount of the subsidence varies between the different interferograms. In Figure 6.5, which shows an interferogram spanning 3.42 months, the subsidence is almost insignificant – about 0.5cm. However, Figure 6.4c, which shows an interferogram spanning 28.41 months, a concentric subsidence of 3cm is detected. The full comparison between the amount of subsidence and the interferogram spanning periods is given in Figure 6.6.

6.1.3 Asa'el site

The Asa'el site is a wide strip (about 400m) that stretches parallel to the shoreline, south to the Hever alluvial fan. Asa'el dry creek crosses the subsidence site at its midst. The Asa'el subsidence site includes the southern Hever sinkhole site on its north. The southern Hever sinkhole site is located south to the southern margins of Hever alluvial fan (Figure 6.3). The subsidence appears in all the 13 interferograms, but in varying paces. Typically the subsidence is divided into two sections – northern and southern. In most interferograms the northern section subsides about 1cm faster than the southern one. In short spanning period interferograms (Figure 6.4a, over 3.42 months) no subsidence is identified along the shore. However, in longer spanning period interferograms, the subsidence pattern is clear (2cm in Figure 6.4f, over 64 months) in spite of the decorrelated strip along the shore. The Asa'el site shows almost an equal rate of subsidence in different interferograms: 0.5cm in 15 months (Figure 6.4b), 1cm in 28.41 months (Figure 6.4c), and 2cm in 64 months (Figure 6.4f). Full comparison between the amount of subsidence and interferogram spanning period is given in Figure 6.6.

Figure 6.5 – Change interferogram 01435_22611, over 3.42 months, showing the four surface subsidence sites: northern Hever, Hever delta, Asa'el and Ze'elim.

6.1.4 Ze'elim site

The site is located on the alluvial fan of Ze'elim dry creek. The decorrelated area on the eastern margins of the subsiding area varies between the different interferograms, but most of the site is correlated. The surface subsidence has a triangular shape. The base of the triangle is parallel to the shoreline and its vertex lies about 500m eastward. Similarly to subsidence sites north of Ze'elim site, the amount of subsidence is greater along its eastern side. In some interferograms the site is divided into two subsiding areas, separated by the trace of Ze'elim creek (Figure 6.4c). The rate of subsidence varies between the different interferograms No subsidence is identified in the 3 months interferogram (Figure 6.5). However, in the 28.41 months and the 64 months interferograms (Figure 6.4c and 6.4f), there are subsidences of 2.5cm and 3cm, respectively, in the same location.
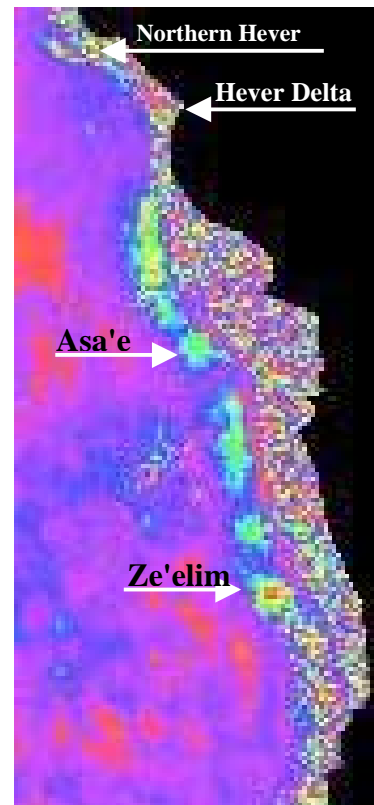
Figure 6.6 – Total subsidence in the four sites, over thirteen spanning periods – the thirteen interferograms analyzed. The estimated subsidence was calculated by counting the color fringes in each site.

6.2 GPS results

Six sessions of GPS measurements were carried out through the two-year duration of this study, between 1999 and 2000, at the northern Hever sinkhole site. Two of the measurement sessions were not successful, due to technical problems. The four successful sessions, carried out on 4/5/1999, 22/12/1999, 17/1/2000, and 26/6/2000 are presented here, focusing on the middle ones. The raw data was processed to form point distribution plots, elevation maps, isogradient maps, shoreline profiles, cross sinkhole profiles, and a map of the differences between two sessions.

6.2.1 4/5/1999 measurement session

Figure 6.7 shows the elevation map of study area 2, as calculated according to the distribution of the 521 locations measured on 4/5/1999. The contours of the elevation map represent 20cm elevation difference. Most of the measured locations are situated on the northern part of the map, except three locations, on the southwest corner of the map. The later three locations were measured on an elevated ancient shoreline, distinct from the mapped area itself, where most of the locations were measured. The westernmost measured point of the three was used as the base station throughout all the measurement sessions. The other two locations, on the same elevation, were used for base station calibration. The majority of the measured locations are distributed in the mapped area in a way that reflects the surface features. Circles of points were measured around the seven major sinkholes in the area. Elongated feature of points trending generally due northwest was measured along the ancient shorelines. Another cluster of points was measured on the northern part of the map, on a suspected local surface depression. The contours that are drawn inside the

Figure 6.7 – location map of the 521 points (red dots) measured at 4/5/1999 in local coordinates. An elevation map (black contours) was drawn according to these locations.

circles of points ("inside the sinkholes") were marked by the software as an interpolation.

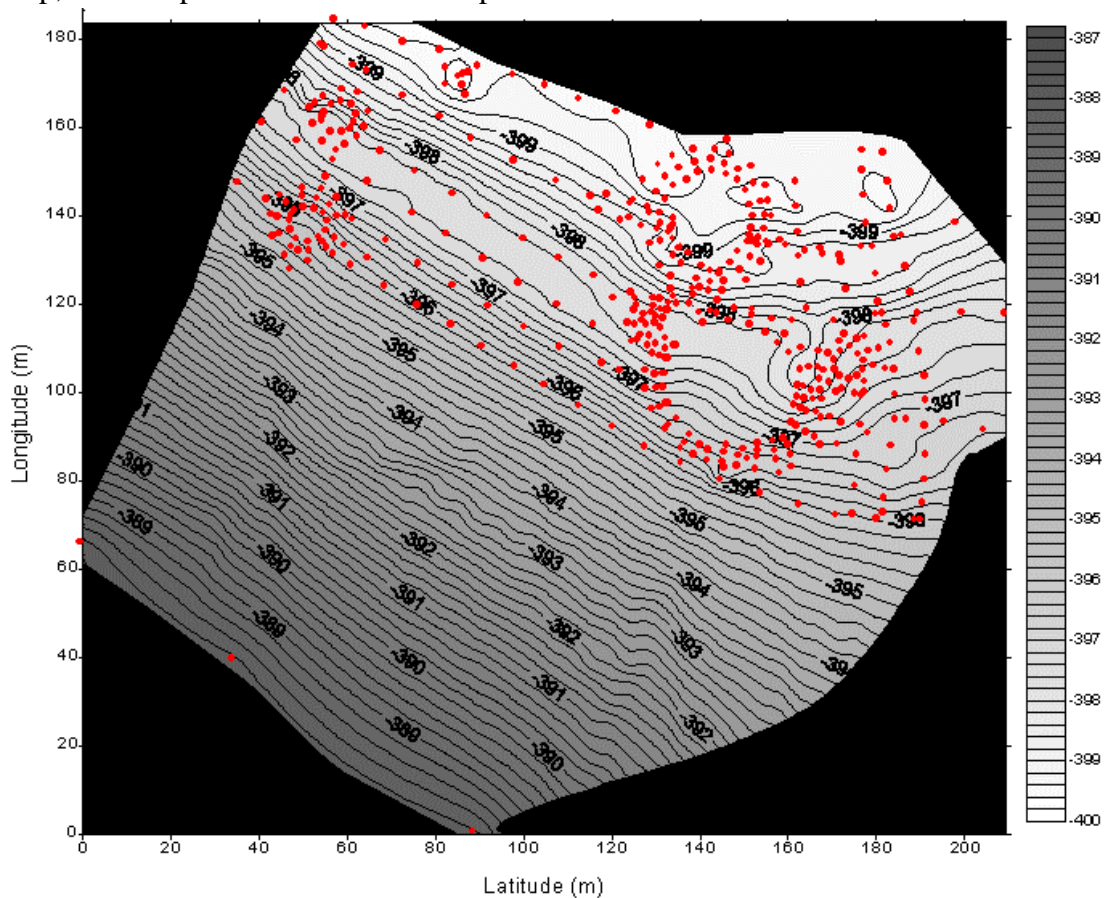Figure 6.8 shows a map of the elevation's isogradient contours. The contours in this map connect nodes of equal elevation gradient. The numbers on the map and the color scale represent the steepness, in degrees. Features, like different slopes, that were identified on the elevation map are more pronounced on the map of isogradient lines. If we look at the map from the lower left corner (southwest) towards the upper right (northeast) we can see that between the three base points and the cluster of the majority of the measured locations (the mapped area) lies a slanted hillside, in slope values up to 5 degrees from the horizon. The gradient map emphasizes the surface morphology that alters between two slope types, moderate and steep, trending due northeast (downhill). The western group of sinkholes is located in an area where the slope is around 5 degrees (the maximum slope in the map). However, the eastern group of sinkholes is located in an area of shallow slope. The southernmost sinkhole on the eastern group is surrounded by slopes that are moderating towards its center.

Figure 6.8 –Map of isogradient contours from 4/5/1999. The slope is given in degrees below the horizon.

6.2.2 22/12/1999 measurement session

Figure 6.9 shows the elevation map overlapped by the distribution of the 768 points measured on 22/12/1999. 357 of the points on the map were measured manually, and the rest 411 were measured automatically, while roving between the manual measurements. The distribution of the measured locations is very similar to that of the previous session, and includes four trails of measurements along ancient shorelines, and seven trails of measurements around sinkholes. However the different range of elevation between the measurement sessions is discussed in the Discussion (next chapter). The blackened areas are areas were no measurements have been made.

The elevation map (Figure 6.9) shows the same division to four sub-slopes, as in the previous session In the area between the two sinkhole groups – a steep slope was observed in the southwest. The slope becomes shallower in the locations trending northeastwards. The group of contours, ranging between –366m and –367m border the eastern sinkhole group from the south. This group of contours curves around the southern sinkhole of the eastern group, and almost surround it, indicating that the

sinkhole complex is situated in a topographic depression. Further north, but still within the eastern sinkhole group, the shoreline morphology between the two sinkhole complexes (northern and southern) is build of a line of small hills (20-30cm). The northern sinkhole complex is situated in a topographic depression, surrounded by elevation contours from the west, south and east.
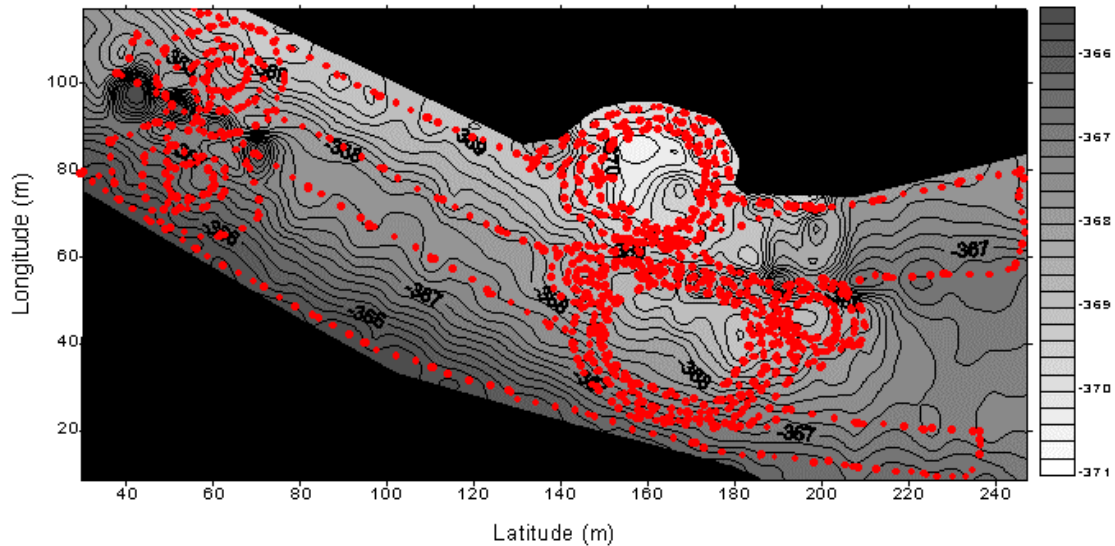
Figure 6.9 – 768 points from the 22/12/1999 (red dots) measurement in local coordinates. An elevation map was drawn according to these locations. The elevation map underlies the locations.

The general picture emerges from the elevation map is of a moderate northward trending slope, with some topographic depressions. The topographic depressions are concentrated on the eastern side of the slope, bordered by "L" shaped elevation contours.

The map of maximum slopes (isogradient lines), Figure 6.10, shows the two major features in the mapped area: (1) the slope between the two sinkhole group is subdivided to four slopes, with alternating steepness; and (2) each of the sinkhole is located within a surface depression, especially the eastern ones.

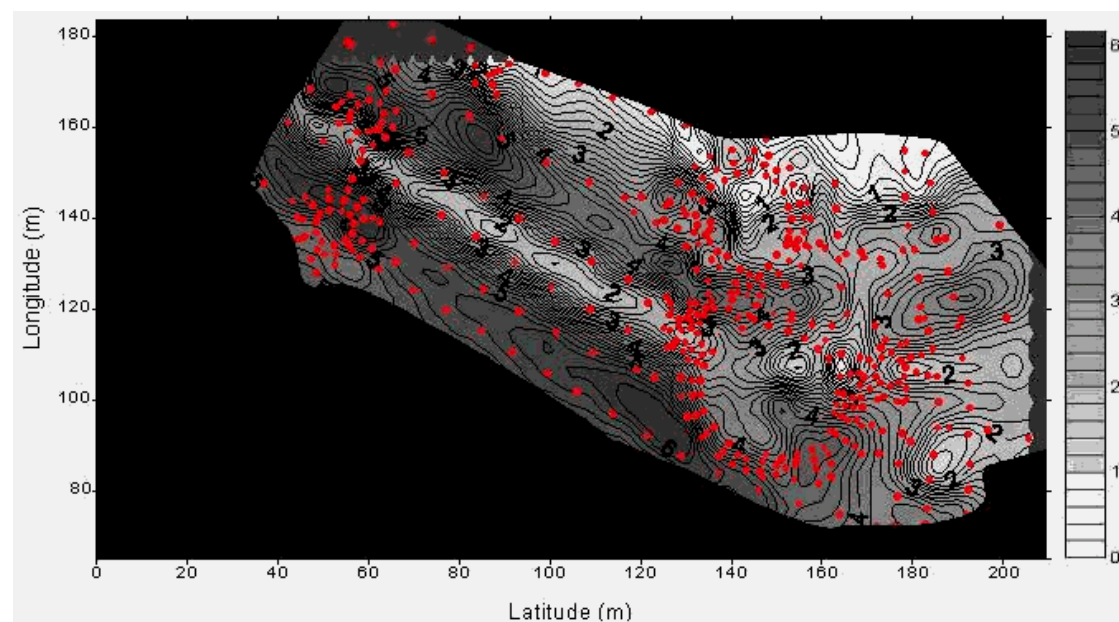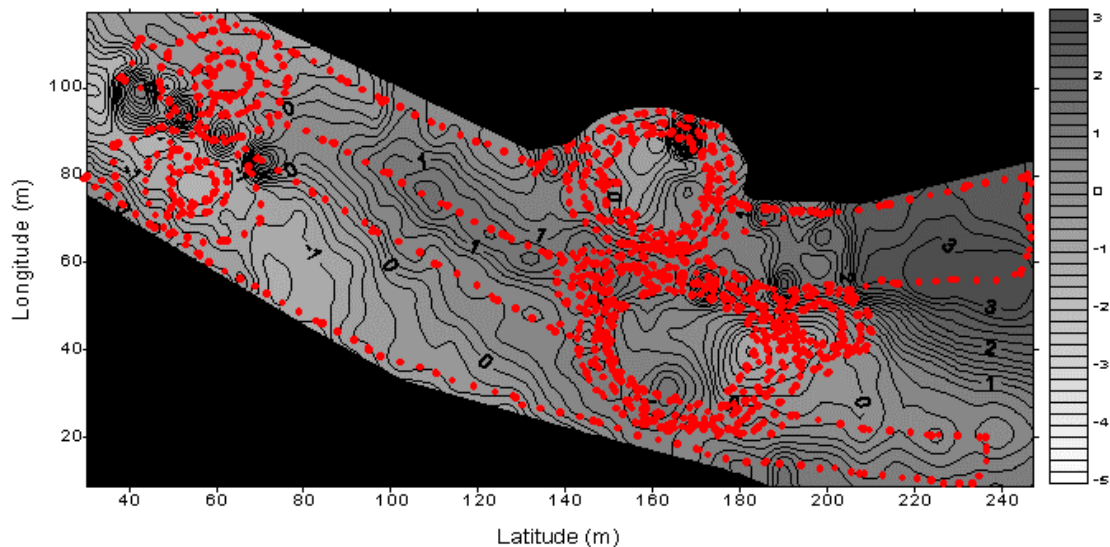**Figure 6.10** –Map of isogradient contours from 22/12/1999. The slope is given in degrees below the horizon.

6.2.3 17/1/2000 measurement session

Figure 6.11 shows the distribution of the 454 measured locations (the red dots), which are distributed in two main patterns: circular and elongated. The circular pattern represent the three round trails of measurements around each sinkhole. The elongated pattern represents measurements that were obtained along ancient shorelines. The black dots in Figure 6.11 are interpolated grid points that were sampled to create topographic profiles of two shorelines (1 and 2) and two cross-sinkholes lines (eastern and western groups). These grid points are use to compare shoreline elevation between different measurement sessions (17/1/2000 and 26/6/2000). The profiles are shown in Figures 6.14 and 6.15 respectively. The location of the base station of the measurements defines the origin (0,0) of coordinate system.
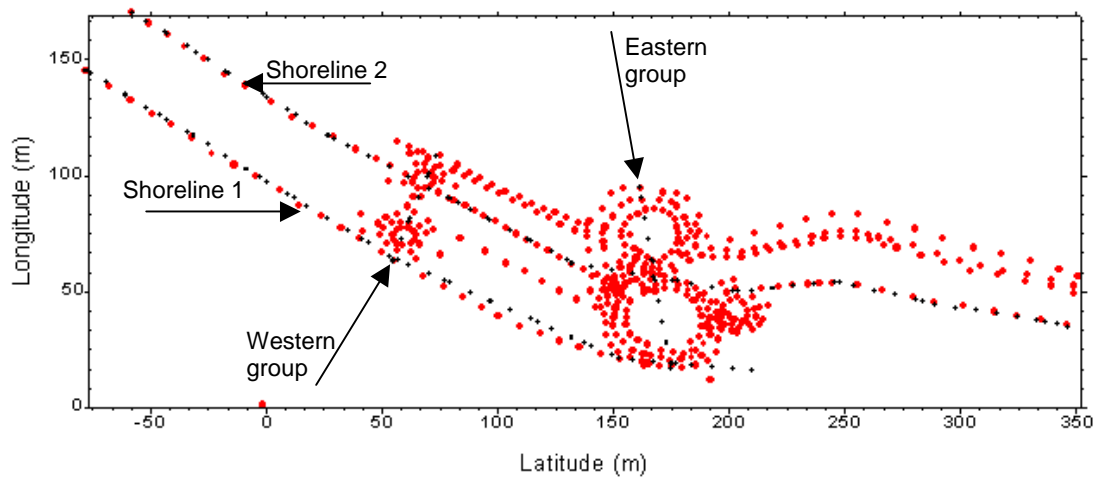
Figure 6.11 - Distribution map of the 454 measured locations (the red dots) on 17/1/2000. The black dots were sampled to form four profiles (Figures 6.14 and 6.15).

The elevation map (Figure 6.12) was sketch according to each of the measured locations (longitude, latitude and height). Yet, not all the rectangular area of the map consists of measured locations. These areas were blackened due to the low reliability of the elevation contours extrapolation. The elevation contours are marked every 20cm, and range from –383m (white) to –377.4m (black). The elevation values are absolute, therefore marked with minus sign. The eight red circles, marked on the map, represent the location of the sinkholes.
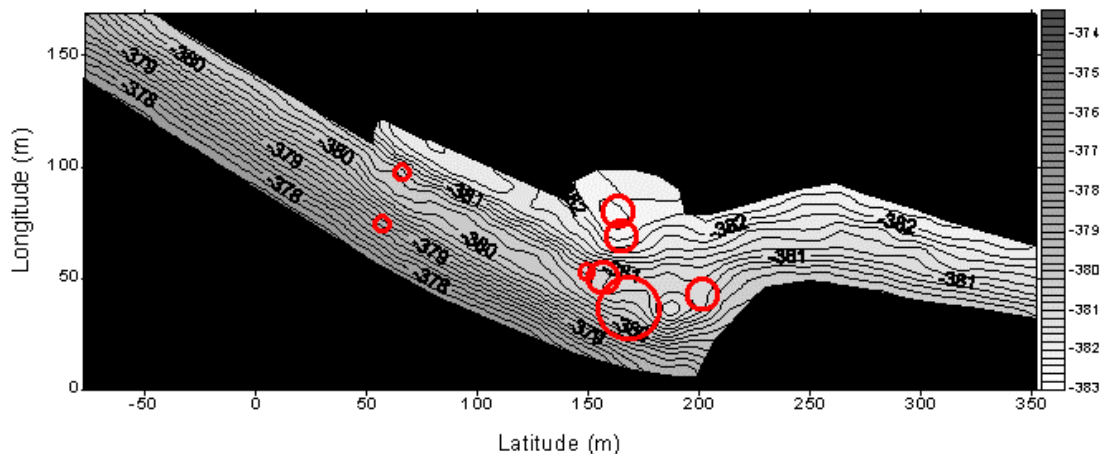
Figure 6.12 – elevation map, based on the measurements from 17/1/2000, with eight circles marking the sinkhole positions.

The elevation contours are sub-parallel throughout the whole mapped area, trending in a general direction southeastward. Between the latitudes of 200m and 250m the general trend changes and the contours are twisted: the southern contours in this area trend northeastward, while the northern ones trend eastwards. This trend change gives the contours the shape of the letter S (rotated counterclockwise), borders the eastern end of the eastern sinkhole group. If we focus on the area between the latitudes 50m and 200m (the sinkholed area) we can divide the northeast sloping hillside into four sub-slopes (from SW to NE). The slope changes from a relatively steep one between the elevations –377.8m and –379.8 (slope a), then become moderate between –379.8m and –380.6m (slope b), between –380.6m and –381.4m it becomes steeper again (slope c), and the rest of the slope is moderate –381.4m and –382.4 (slope d). Most of the sinkholes are located on the moderate slopes (b and d). The slope upon which the eastern group of sinkholes is located is not only moderate but also wider than the same sub-slope in the western group area. Furthermore, the area between the two southern sinkholes of the eastern group is lower by more than 40cm than its surroundings.

The different sub-slopes can be identified in the elevation map (Figure 6.12), but can be seen more easily on the map of isogradient contour map (Figure 6.13). The later map displays longitude and latitude range, in which blackened area represent areas where no measurements were done; and the sinkhole locations. The shorelines and their subdivision of steepness are emphasized by alteration of the elongated strips of high and low steepness. The lying "S" shape of the shorelines is identified, as well as an area of zero gradient between the two southern sinkholes of the eastern group.
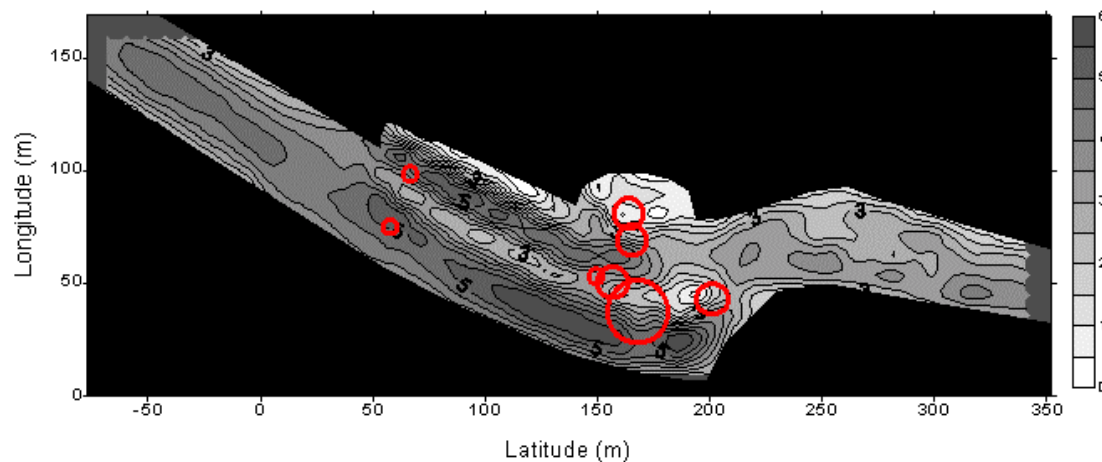
Figure 6.13 –Map of isogradient contours, based on the measurements from 17/1/2000, with eight circles marking the sinkhole positions. The slope is given in degrees below the horizon.

Based on the elevation map (Figure 6.12), four topographic profiles were drawn. The profiles were sampled along two shorelines, and across each of the sinkhole groups. 51 grid points were interpolated to calculate the shoreline 1 profile, and 71 locations for shoreline 2. He sampled points appear with error bars of +-10cm. The location of the profiles is marked in Figure 6.11 by black dots. The next two paragraphs describe the two profiles.

Figure 6.14 shows the two topographic profiles along shorelines 1 and 2. Shoreline 1 is situated south of shoreline 2, as can be seen in the map in Figure 6.12. Furthermore, shoreline 1 is topographically higher than shoreline 2, hence its elevation in the topographic profiles is higher. The profiles of both shorelines show topographic depressions in two areas. The elevation on both sides of the depressions has similar values (-387.8m on shoreline 1 and –380 on shoreline 2). The location of

these topographic depressions is in accordance with the location of the two sinkhole groups (eastern and western).

The profile of shoreline 2 is longer than the profile of shoreline 1 in the horizontal dimension (435m compared with 320m), and represent a wider sampling area on both sides of the sinkhole groups. The sub horizontal red line marks the slope of shoreline 1 in the areas beyond the segments 1, 2 and 3. The slope is 0.3^0 below the horizon. Segments 1 and 3 label the western and the eastern groups of sinkholes, respectively. These segments are topographically lower than the red slope line (the mean surface) by 40cm (segments 1) and 1m, (segments 3). Moreover, the area between the sinkhole groups, segment 2, is lower by 30cm from the red slope line surroundings.

Shoreline 1 shows only part of the picture seen on shoreline 2. There are two topographic depressions in the two locations labeled 1 and 3. The western subsidence is lower by 35cm from its surroundings, whereas the eastern subsidence is lower by 1.6m. The area between the two depressions is lower by 50cm from the area that exceed the two depressions. The area southeast (right) to the eastern subsidence (segment 3) doses not appear on shoreline 1 because no points were measured there.

Two additional topographic profiles (Figure 6.15) were drawn normal to the shoreline profiles, across each of the sinkhole groups (Figure 6.11). The profiles were calculated from the elevation map. The two profiles range between similar elevation values: -381.66m to –377.98 on the western profile, and –382.13 to –379.13 on the eastern profile. The western profile is shorter (50m long) and steeper than the eastern one (80m long), as can be seen in Figure 6.15, as well as in the elevation map (Figure 6.12). Four elevation depressions were identified along the profiles (two in each). The topography inside the sinkholes is not presented in the profiles because it was not measured. The profiles were interpolated in the locations of the sinkholes, and appear as three depressions in Figure 6.15, in accordance with the major sinkholes.
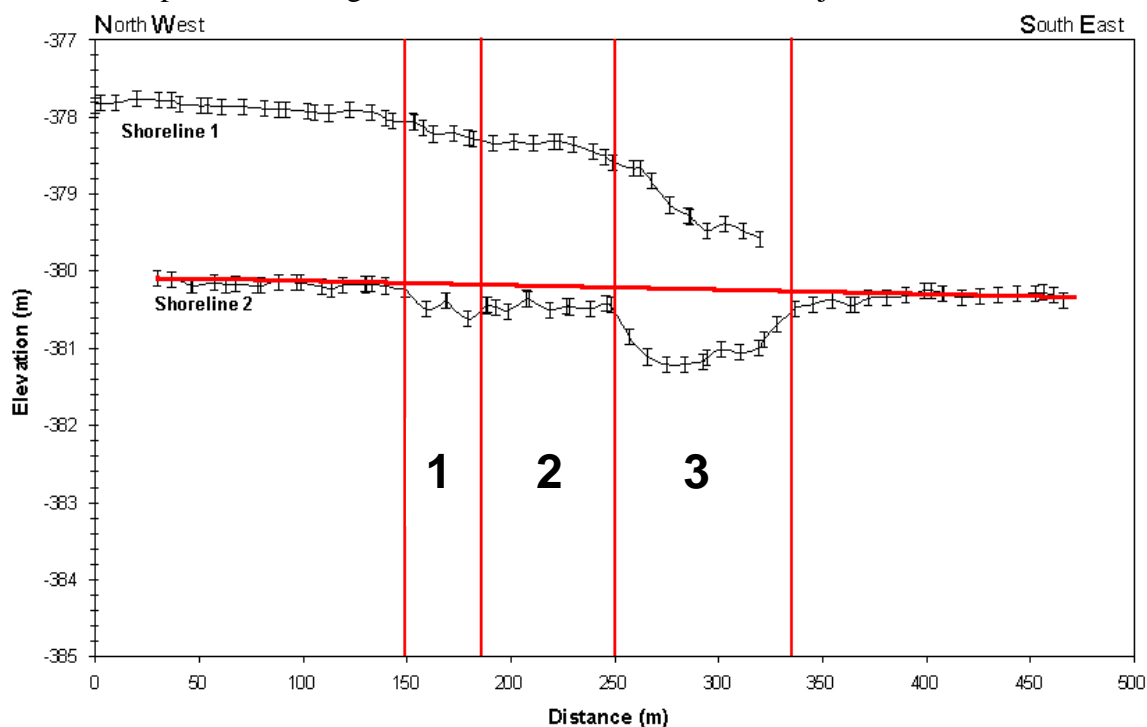
Figure 6.14 – Profiles of shorelines 1 (upper) and 2 (lower), according to the 17/1/2000 measurements. Vertical error bars are marked on the sampled points (+-10cm). The profiles are divided into three segments. Segments 1 and 3 represent the western two and the eastern groups of sinkholes respectively. Segment 2 is the area between the sinkhole groups. The sub horizontal red line, tangent to shoreline 1, marks the slope of shoreline 1 (0.3°) in the areas beyond the sinkholed (it is not a trendline).
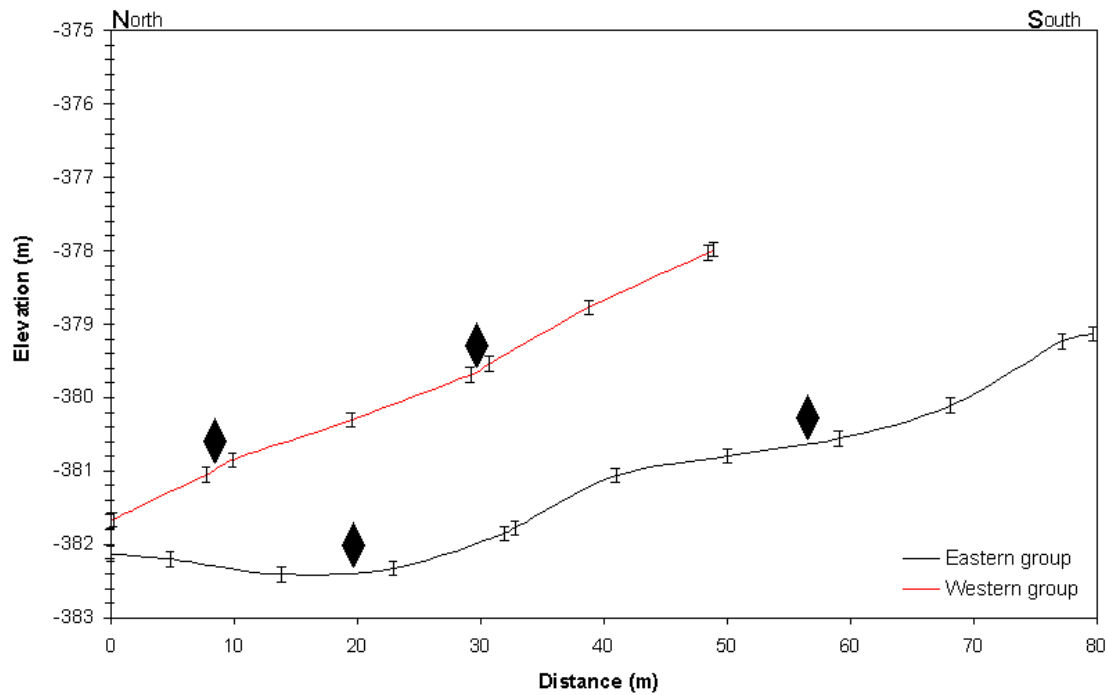
Figure 6.15 – Topographic profile of the north trending cross-sections through the two groups of sinkholes. Vertical error bars are marked on the sampled points (+-10cm). The eastern cross-section is marked in black, and the western in red. Black stars mark the location of sinkholes.

6.2.4 26/6/2000 measurement session

Figure 6.16 shows the distribution of the 355 points measured on 26/6/2000 overlay the elevation map (drawn on the basis of this session measurements). 355 of the 6768 locations were measured manually, and the rest 6413 were measured automatically, while roving between the manual measurements. The measurements were carried on in a similar distribution of the measured locations, both around the sinkholes, between them, on ancient shorelines, and exceeding the sinkholed area (westwards and eastwards). As can be seen in the elevation map, the pattern of different slopes and surface depressions that appeared in the former measurement sessions does not appear here. Moreover, the range of the topographic highest and their values are different from the other four sessions of measurements. Therefore I choose not to focus on this session, due to its low reliability in the vertical dimension.

6.2.5 Subtracting the 17/1/2000 measurements from the 26/6/2000

The surface relief of northern Hever sinkhole site differs between the different measurement sessions by elevation range and patterns. These elevation changes originate from vertical displacements at the surface, yet, some of the elevation differences (e.g. different ranges of elevation) may arise from technical reasons. A more quantitative perspective is given in the subtraction between two GPS session measurements over a period of 6 months, between 26/6/2000 and 17/1/2000 (Figure 6.17). Despite a relatively large number of measured points in the 26/6/2000 session (6768 points), the result range of the points' vertical component beyond the reasonable (15 m). The range of the vertical component in the 17/1/2000 measurement session (454 points measured) is 2 m. In order to compare these two measurement session by subtraction the vertical component of the 26/6/2000 was scaled to fit the 17/1/2000 vertical range.
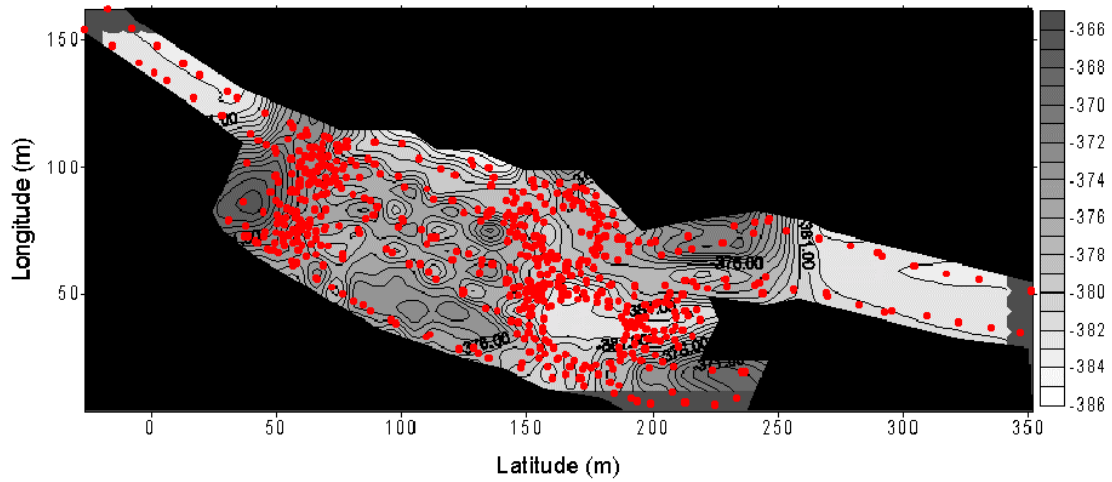
Figure 6.16 - Elevation map, based on the measurements from 26/6/2000, with red dots marking the manually measured locations.
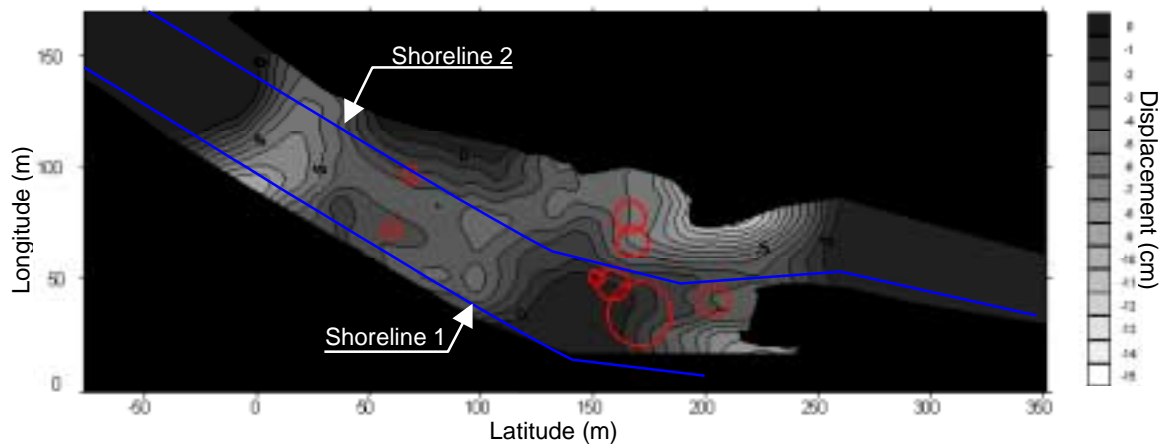
Figure 6.17 – Map showing the subtraction result between the 26/6/2000 and 17/1/2000 GPS measurement sessions. The displacement contours are given in centimeters. Red circles mark the location of the sinkholes. Blue lines mark the ancient shorelines 1 and 2.

6.3 EDM results

Two sessions of EDM measurements were carried out through the two-year period, between 1999 and 2000, at the northern Hever sinkhole site. The measurement sessions were carried out on 27/2/1999 and 19/3/2000. The results of the 19/3/2000 session are presented here (Figure 6.17). These measurements were used only as calibration for the GPS measurements. The calibration was done in two levels – in the field and while producing the results: in the field, the 28 fixed locations of the EDM served as anchor locations while roving with the GPS. These fixed locations served again in the data processing stage to overlap maps of different measurements sessions correctly. And last, the comparison between the two EDM measurements (Figure 6.17) helped to verify the vertical displacement of the surface in the GPS measurements.
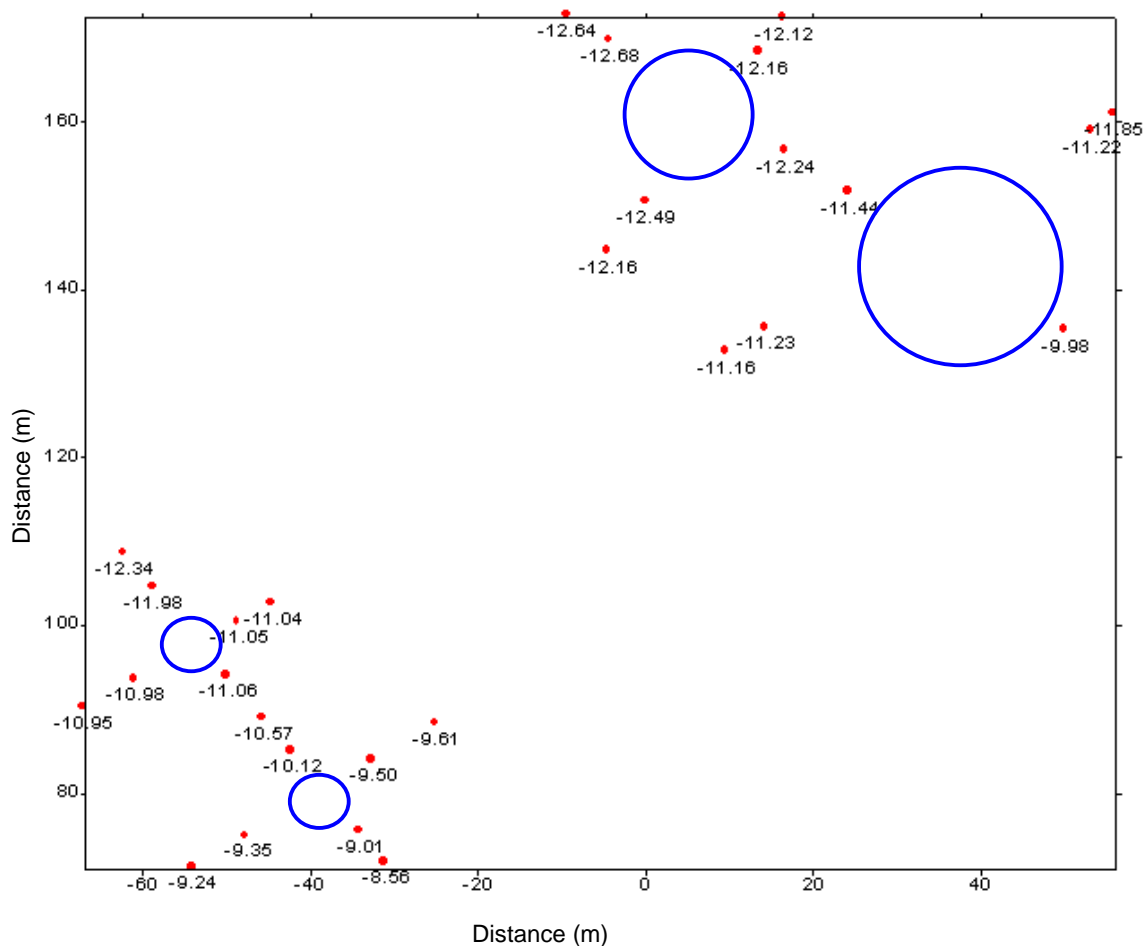
Figure 6.17 - Results of the 19/3/2000 measurement session, on a local coordinate system. The distances are related to the devise itself, which was located on the (0,0) coordinate. The measured locations are marked red and labeled with their relative height (relative to the EDM devise). Blue circles mark the location of the major sinkholes.

7. Discussion and conclusions

This research monitored surface deformations on the western shores of the Dead Sea along a period of two years (1998-2000). The main surface deformation observed features were sinkholes, areas undergoing wide scale surface subsidence and tilt of ancient shorelines. Secondary surface deformation observed features were localized surface subsidence and concentric cracks accompanying sinkhole development. The following sections discuss first the work techniques and methodologies, then the mechanisms that underlie the various surface deformation phenomena, the results of the measurements, and finally the spatial interactions between the surface subsidence and sinkholes.

Five different methods were used for monitoring sinkhole development and surface subsidence, of at various scales. **Field observations** were conducted during a two two-year period (1998-2000) in the studied area, along the shores of the Mezada plain, focussing on the northern part of Hever alluvial fan. A systematic **analysis of air photos** covering the western shores of the Dead Sea, which span over a nine years period (1990-1999), was used to trace the development in the northern Hever sinkhole site. Considerable vertical deformation was identified in the surface behavior, reflecting development of sinkholes and surface subsidence.

The current study focused on two main space-based geodetic techniques: GPS and InSAR. We conducted six sessions of kinematic **GPS measurements** in the northern Hever sinkhole site during a two-year period (1998-2000). Two of the sessions were not successful. The results of the measurements were used for mapping the surface of the sinkhole site, and for monitoring the changes in its elevation. The GPS measurements showed vertical displacement of the ancient shorelines. **InSAR measurements** were used for obtaining the spatial information of the topographic changes in the Mezada plain and the rate of the changes. Thirteen scenes were acquired during a period of 7 years (1992-1999) using the 2979 frame (descending orbit). The calculated interferograms cover span periods of 2 to 64 months. The different interferograms showed round, elongated and amorphous features. The changes of the Dead Sea water level were seen as a strip of deceleration in the different interferograms.

EDM measurements were conducted in the northern Hever sinkhole site. The results of these measurements are accurate and show elevation changes over a period of one year. The EDM measurements are accurate (centimeter level) but less effective when measuring a large number of locations. The relatively small number of measured locations in each of the two sessions (28 locations) is not enough for drawing a credible elevation map and reaching substantial conclusions. Yet, all locations of the EDM measured points were fixed in the ground (section 6.3), and were therefore used as calibration points for GPS measurements. The 28 fixed locations were measured during the GPS sessions, along with the other locations. In the data processing stage these fixed locations served as `anchors` for comparing the elevation maps of the different measurement sessions.

The large-scale surface subsidences are not easy to detect on field observations, as are sinkholes. These surface subsidences occupy hundreds of square meters, consequently mapping their surface with the GPS technique demands a large number of measured locations (for creating a credible elevation map). The InSAR technique was used for identifying sub-centimeter vertical changes of the surface over large area (hundreds of square kilometers) (Massonnet and Feigl, 1998). On the other hand, the horizontal accuracy of the InSAR technique is limited to the size of the pixel

on the surface of the earth (20X5m). This resolution is not high enough for monitoring the sinkholes on the Mezada plain because of their size (about the size of a pixel). Therefore we measured the northern Hever sinkhole site topography using the kinematic GPS. The combined data obtained by the five monitoring methods above enables us to give a comprehensive evaluation of the Mezada plain surface topography.

Sinkholes

The formation of sinkholes is related to the lowering of the Dead Sea water level during the last few decades. The lowering of the Dead Sea water level induces changes in the configuration of the groundwater level and the fresh-saline water interface (Wachs et al., 2000). The general mechanism for the formation of sinkholes suggests that cavities are formed in salt layers in the subsurface. The cavities are formed in the salt in places where unsaturated water (with respect to salt) reaches the layer and dissolves the salt from underneath it. The failure of the roof of such a cavity initiates a series of subsurface collapses. Eventually the collapses reach the surface and sinkholes are formed (GSI, 1998).

The current research focused on the sinkhole formation in the northern Hever sinkhole site. According to this research and Itamar and Reizmann (2000), sinkholes tend to develop in clusters (Uvala). Field observation indicates that each sinkhole affects its surrounding area in the form of surface sinking and concentric cracks. The GPS measurements had shown that the deformed area around sinkholes extends up to 5 times the sinkhole diameter (70m in the northern Hever sinkhole site) (section 6.2.5). Another field observation was the deformation rings around sinkholes. Sinkholes and their deformation rings appear circular in plain view (section 4.5.2.3). The amount of vertical deformation (surface sinking) increases closer to the margins of a sinkhole. In places where two sinkholes were formed close to one another, the deformation rings partly overlap. The overlapping complicates the deformation and forms uplifted zones within sinking areas. This surface feature was measured in the different GPS sessions, i.e. the 17/1/2000 session (Figure 7.1).
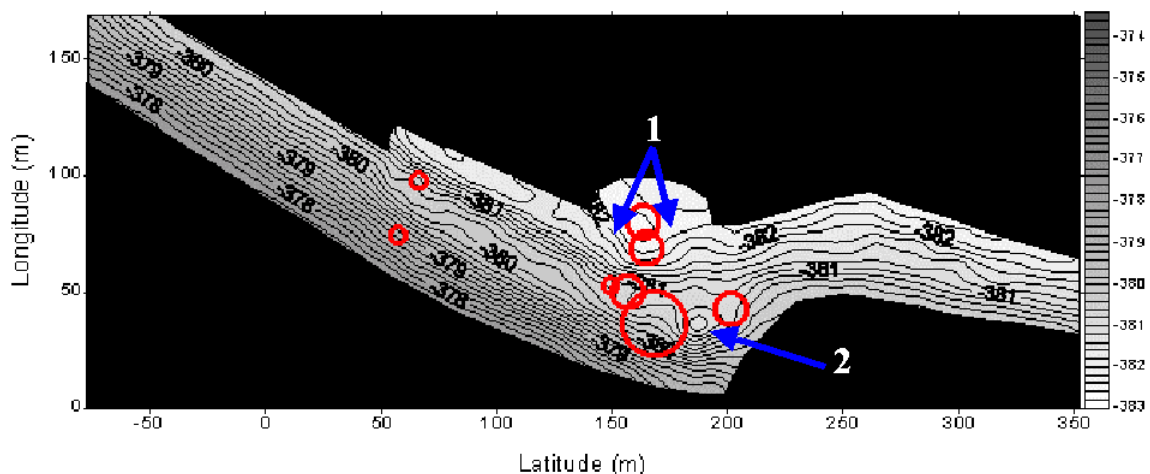

Figure 7.1 – Elevation map, based of the GPS measurements from 17/1/2000, with eight circles marking the sinkholes' position. The blue arrows (1) mark area that slope and sink towards the sinkholes; and the blue arrow (2) marks an uplifted zone within a sinking area between two sinkholes.

An additional feature, in the study area, that indicates vertical displacement at the surface is the ancient shorelines. The ancient shorelines are assumed to be horizontal as they were formed by the energy of the lake waves; therefore they were chosen as surface elevation changes markers. Two of the ancient shorelines of the northern Hever sinkhole site underwent vertical displacement. Figure 6.17 shows that the vertical displacement of the ancient shorelines extends only over the area of the sinkholes, hence related to the sinkhole formation. A larger scale vertical displacement of the ancient shorelines is presented in Figure 6.14 (the shoreline profiles). In Figure 6.14 the ancient shorelines slope 0.3^o southeastward over a 500 m distance. This topographic gradient was identified by GPS observations during the 1998-2000 measurement span. Interestingly the GPS-determined gradient change is perpendicular to the one identified in the same area by InSAR measurements between 7-11/1995 (section 6.1.1). The subsiding area in the northern Hever sinkhole site is very active showing development from a general subsiding area in 1995 to sinkhole-oriented subsidence.

Land subsidence

Land subsidence (gradual settling of the ground) is induced by the combination of ground water level changes and the degree of soil cohesion in the shallow subsurface. The ground water level changes stimulate fluctuations in the pore pressure, and as a result small breakdowns of the granular structure in the subsurface (Figure 2.4). On the surface the resulting vertical displacement is of few centimeters while the area of the land subsidence may cover a few square kilometers. The reversibility of the granular structure deformation depends upon the amplitude the ground water changes, as well as the ground combination. Unconsolidated rocks are more vulnerable for changes in the pore pressure (USGS, 2000).

Vertical displacements, which were identified in the interferograms of four sites - Hever north, Hever delta, Asa'el and Ze'elim – can be examined in the light of the changes in Dead Sea water level and three drill-holes. We can see that following

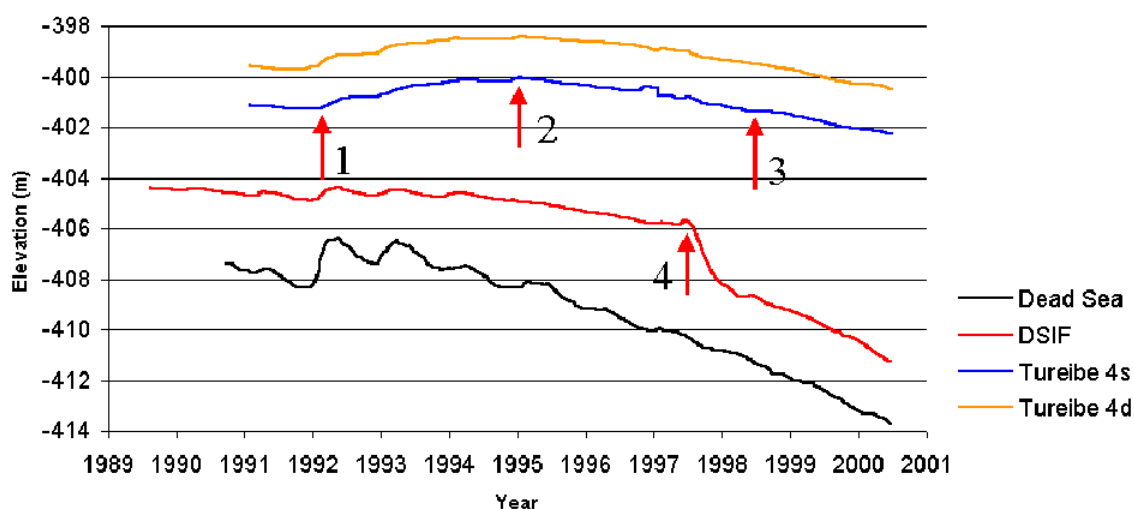**Figure 7.2 –** Water level of the Dead Sea (black), ground water in three drill holes (red, yellow and blue), over a 12 years period (after GSI, 2001). Four critical dates are marked: (1) the ground water level rise start point, February 1992; (2) the top of the rise, February 1995; (3) the ground water level are back in the February 1992 level, June 1998; and (4) the DSIF starts a major drop of 3m over 6 months, June 1997.

the two consecutive rainy winters, 1991-92 and 1992-93, the ground water level on the western Dead Sea shores climbed by 1.24m (Figure 7.2). This climb started on February 1992 (marked as '1' on Figure 7.2) after a long period in which the Dead Sea level lowered in a rate of about a meter per year (Figure 1.2). The anomalous rainy winters affected the ground water level for 6.5 years. On February 1995 the ground water reached its highest level and started falling. By the end of June 1998 the ground water level reached the same elevation as on February 1992, and continued to fall. These three critical dates (February 1992, February 1995, and June 1998) are marked on figures 7.2 and 7.3.

The vertical movements measured in the above four sites, using the InSAR technique, represent the net vertical change of the surface elevation between the two images of each interferogram. Therefore we expect that the longer the interferogram's time spans, the larger the vertical deformation will be. Unfortunately, this is not the picture. For example, the vertical deformation measured in the 04732_12958 interferogram in Asa'el site (Figure 7.3), which covers a period of 64.09 months, is 2cm. Nevertheless, 3cm of vertical deformation were measured in the 13960_20473 and 22611_09451 interferograms, which span 14.96 and 15 months respectively. The answer is probably the timing of the interferogram. The 22611_09451 interferogram spans from November 1995 till February 1997. During this period the ground water level drops continuously. However, the 04732_12958 interferogram spans from June 1992 till October 1997. This period can be divided into two parts, in terms of the ground water level: June 1992-February 1995 rise of the ground water level, and February 1995-October 1997, ground water level drop. If the interferogram shows the net vertical deformation of the surface, and this deformation is induced by the ground water level changes, then the land subsidence was not continuous in time. According to the current set of data it is not possible to tell what was the degree of ground settling before February 1995. Yet, comparing with the shorter spanning interferograms mentioned above we conclude that some of the surface subsidence that occurred after February 1995 were compensated by none or negative (uplift) surface subsidence that probably occurred before February 1995.

Surface subsidence in the study area and beyond (on the western shores of the Dead Sea) did not developed continuously with time. The rate of subsidence changed in an unpredictable manner over time. This may be partly explained by the changes in the Dead Sea water level, which dropped by about 6 m during the period covered by the interferograms. This drop in the water level affected the hydrological settings in the subsurface of the shore region by (1) changing ground water level, (2) the arrangement of ground water horizons, and (3) the shape of the fresh-saline water interface. All the changes assumed here were expressed in the rate and spatial distribution of the surface subsidences. The InSAR measurements show that surface subsidence occupy considerably wider areas than sinkholes (hundreds of square meters relative to few tens). There are sites where both sinkholes as well as surface subsidences occurred.

Sinkholes and surface subsidences

Sinkholes and wide regions of surface subsidence are probably the surface reflections of changes in the Dead Sea water configuration and its surroundings over the years (Wachs et al., 2000). Sinkhole formation is affected mostly by the shape and location of the fresh-saline water interface, that determine the relations between underground salt layers and unsaturated water. On the other hand, surface subsidences are affected by the changes in the ground water level and the degree of consolidation in subsurface layers. February 1995 was a critical date for the development of surface subsidence and sinkholes on the western shores of the Dead Sea. From this date on, the ground water level started to drop continuously, after a 3- year period of ascending resulting sinkholes and surface subsidences development accelerated (Schattner et al., 2000).
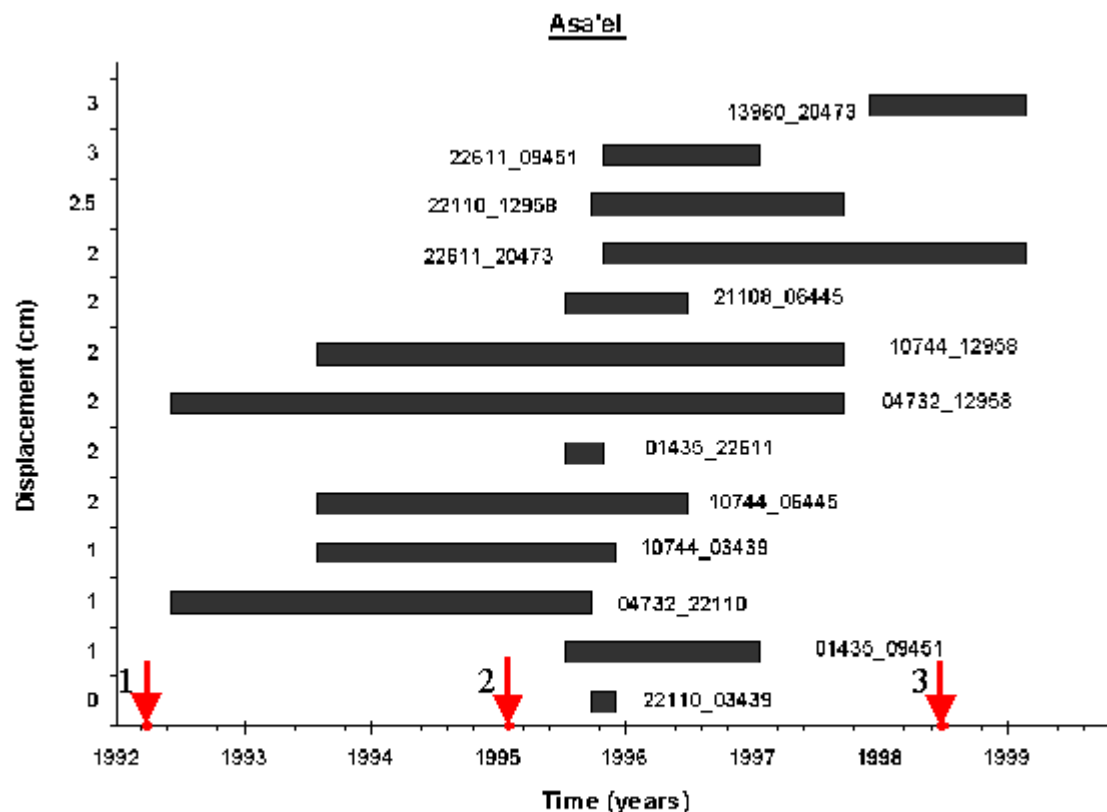
Figure 7.3 – Diagram of the vertical displacement measured in 13 interferograms on the Asa'el surface subsidence site. The black bars represent the span of the different interferograms. The red arrows 1, 2, and 3 mark the three critical dates of the ground water level changes (Figure 7.1): (1) the ground water level rise start point, February 1992; (2) the top of the rise, February 1995; and (3) the ground water level are back in the February 1992 level, June 1998.

Anderson et al. (1998) investigated a case study of surface subsidence and sinkholes in central Kansas. Using seismic reflection and refraction a salt layer was found in the shallow subsurface, with its top at depth of about 100 m. The researchers expected that the salt layer would be thin where maximum surface subsidence and sinkhole development had occurred, and thicker elsewhere. Contrary to expectations, the salt layer was found to be relatively thick below areas of significant surface subsidences and sinkhole concentration. If the salt layer in the shallow subsurface of the western shores of the Dead Sea (section 1.1.3) behave in the same manner, it might explain the rate, scale and spatial distribution of the surface subsidences and sinkholes at the surface.

Seismic refraction studies overviewed in section 1.2.2 draw a connection between the relief of the salt layer topography, and the layout of the dry creeks on the shores of the Dead Sea (Shtivelman, 2000a; Ronen, 1997; Shtivelman, 1998; Shtivelman et al., 1994; Beck and Ronen, 1994; Ronen and Ezersky, 1998; Ronen et al., 1992; Shtivelman, 2000a; Shtivelman, 2000b; Shtivelman et al., 1999; Ronen and Beck, 1997; Ronen and Ezersky, 1997). The salt layer top, inferred by the seismic refraction studies mentioned above, is deeper beneath the creek and shallower towards the margins of the alluvial fan (Figure 7.4). The connection between the surface subsidence and sinkhole sites layout (surveyed in this work), the salt top and the creek layout suggested here give a three-dimensional picture of the vertical displacements formation. A systematic seismic investigation, mapping the salt layer top along the Dead Sea shores, may clarify the subsurface picture and help us predict where sinkholes and surface subsidences are more likely to develop.

The Dead Sea shores are very vulnerable and easily affected by the changes in water level of the Dead Sea. Sinkholes and the surface subsidences develop along the shores as an indirect consequences of anthropogenic interference in the natural water management of the Dead Sea basin (stopping the water flow into the Dead Sea, and pumping water from it). This emphasizes the environmental influences of every change caused by man.
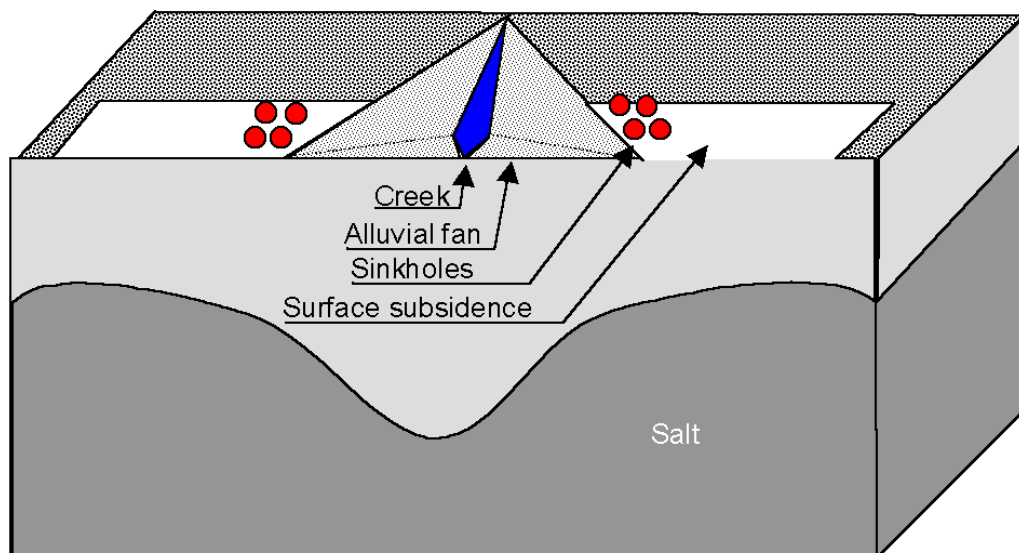

Figure 7.4 – Scheme of the layout of a creek and its alluvial fan, with surface subsidences and sinkholes adjacent to the fan margins. At depth, the relief of a salt layer, with its picks beneath the surface subsidences.

7.1 Conclusions

Surface subsidence

1) Surface subsidences develop differently in different time periods, and in irregular shapes.
2) February 1995 was a critical date for the development of surface subsidences on the western shores of the Dead Sea.

Sinkholes

The development of a sinkhole affects the surface topography that surround it:
3) Surface deformation extends up to 5 times the diameter of the sinkhole.
4) Sinkhole formation induces topography changes of the surface within and beyond the sinkhole site. Two ancient shorelines, which served as markers in the northern Hever sinkhole site, were measured sloping 0.3o towards southeast over a 500m distance.
5) The subsiding area in the northern Hever sinkhole site shows development over time – from a general northeast trending subsiding area (InSAR measurements from 1995) to sinkhole-oriented subsidence trending southeast (GPS measurements from 2000).
6) Sinkhole sites develop outside the boundaries of alluvial fans. Sinkholes and

Surface subsidence

7) Surface subsidence develops in each of the sinkhole sites, but the opposite is not necessarily true. Therefore the subsidences cannot serve as precursors for the development of sinkholes.

References

Anati, D. A., and Shasha, S., 1989, Dead Sea surface level changes: Isr. J. of Earth Sci., v. 38, p. 29-32.

Anderson, N.L., and Knapp, R., 1993, An overview of some of the large scale mechanisms of salt dissolution in west Canada. Geophysics, v. 58, p. 1375-1387.

Anderson, N.L., Martinez, A., Hopkins, J.F., and Carr, T.R., 1998, Case history - Salt dissolution and surface subsidence in central Kansas: A seismic investigation of anthropogenic and natural origin models. Geophysics, v. 63, p. 366-378.

Arkin, Y., 1993, "Karstic" sinkholes in alluvial fans, Isr. Geol. Soc. an. meet.. Field trips guidebook, p. 71-80.

Arkin, Y., Gilat, A., and Kofman, L., 2000, Developing Dead Sea sinkholes revealed by ground penetrating radar. Geol. Surv. Isr. Cur. Rep., v. 12.

Arkin, Y., and Michaeli, L., 1995, Sinkholes in the Nahal Arugot alluvial fan. Jerusalem, Geol. Surv. of Isr., Rep. No. p. 17.

Baer, G., 1999, SAR Interferometry measurements of surface deformation in the Dead Sea area as a possible clue for the development of sinkholes: a feasibility study, Geol. Surv. of Isr., Rep.

Baer, G., Sandwell, D., Williams, S., Bock, Y., and Shmir, G., 1999, Coseismic deformation associated with the November 1995, Mw=7.1 Nuweiba earthquake, Gulf of Elat (Aqaba), detected by synthetic aperture radar Interferometry: J. of Geophys. Res., v. 104, p. 25221-25232.

Baer, G., Schattner, U., Wachs, D., Sandwell, D., Wdowinski, S., and Friedman, S., 2000, The lowest place on earth is subsiding - InSAR perspective, Geol. Surv. of Isr.

Bechor, N., 1998, Measurements of Current Tectonic Movements in the Sinai Subplate Using GPS Observations: M.Sc. Thesis, Tel-Aviv University, Tel Aviv.

Beck, A., and Ronen, A., 1994, Ground Penetrating Radar survey for detecting subsurface voids at the Paradise hotel site, Dead Sea: Lod, The Geophys. Inst. of Isr., Rep. No. K36/66/94.

Beck, B.F., 1984, Sinkhole terminology, in Beck, B.F., ed., Sinkholes: their geology, engineering and environmental impact: Proceedings of the first multidisciplinary conference on sinkholes: Orlando, Florida, p. 9-10.

Bennett, P., 1997, The Global Positioning System FAQ, http://www.gpsy.com/gps info/gps-faq.txt.

Bögli, A., 1980, Karst hydrology and physical speleology: New York, Springer-Verlag Berlin Heidelberg, pp.

Curlander, J.C., and McDonought, R.N., 1985, Synthetic aperture radar systems and signal processing: New York, Wily-interscience, 70 p.

Dana, P.H., 1999, Global Positioning System Overview, http://www.utexas.edu/depts/ grg/gcraft/notes/gps/gps.html.

Dias, W., C., 1999, IBM Geographic information systems, GPS, http://giswww .pok. ibm.com/gps.

Ezersky, M., and Goldman, M., 1999, Detection of potentially dangerous subsurface karstic zones using electrical and electromagnetic methods in the Mishor Rotem area: Lod, The Geophys. Inst. of Isr., Rep. No. 906/69/98, p. 21.

Fairbridge, R.W., 1968, The encyclopedia of geomorphology: New York, Reinhold Book Corp., 295 p.

Frumkin, A., 1997, The Holocene history of Dead Sea levels, in Niemi, T.M., Ben-Avraham Z., and Gat, J., (eds.), <u>THE DEAD SEA the Lake and its Setting</u>: New York, Oxford University Press, p. 237-248.

Garfunkel, Z., 1997, The history and formation of the Dead Sea, in Niemi, T.M., Ben-Avraham Z., and Gat, J., (eds.), <u>THE DEAD SEA the Lake and its Setting</u>: New York, Oxford University Press, p. 3-7.

Genrich, J., F., and Bock, Y., 1992, Rapid resolution of crustal motion at short ranges with the Global Positioning System: Journal of Geophysical Research, v. 97, p. 3261-3269.

GSI, 1998, Sinkholes in the Dead Sea shores - a framework for the geologic and geophysics work, Geol. Surv. of Isr., Jerusalem, 11 p.

Hager, B.H., King, R.W., and Murray, M.H., 1991, Measurements of crustal deformation using the Global Positioning System: Annu. Rev. Earth Planet. Sci., v. 19, p. 351-382.

Itamar, A., and Raizman, U., 2000, Sinkholes on the Dead Sea shores - Development survey through air photos, The Geol. Surv. of Isr.,

Kafri, U., Goldman, M., and Lang, B., 1997, Detection of subsurface brines, freshwater bodies and the interface configuration in-between by the time domain electromagnetic method in the Dead Sea Rift, Israel: Environmental Geology, v. 31, p. 42-49.

Kaufman, A., Yechieli, Y., and Gardosh, M., 1992, A reevaluation of the lake sediment chronology in the Dead Sea Basin, Israel, based on new -230Th/U Dates: Quaternary Research, v. 38, p. 292-304.

Klein, C., 1985, Fluctuations of the levels of the Dead Sea and climatic fluctuation in the country during historical times, International Symposium of Scientific Basis for Water Resources Management: Jerusalem.

Leick, A., 1995, GPS Satellite Surveying New York, John Wiley & sons, INC., 560 p.

Massonnet, D., and Feigl, K., L., 1998, Radar Interferometry and its application to changes in the earth's surface: Reviews of geophysics, v. 36, p. 441-500.

Monroe, W.H., 1970, A glossary of Karst terminology, United States Geological Survey, p. 26.

MSU, 2000, Glossary of GPS Terms, http://www.montana.edu/places/gps/glossary.html, Montana, State University.

Myers, A.J., 1962, A fossil sinkhole: Oklahoma Geology Notes, v. 22, p. 13-15.

Naor, H., Katz, D., and Harash, Y., 1987, Hydrogeological study to locate production wells in Wadi Zohar area, TAHAL.

Neev, D., and Emery, K.O., 1967, The Dead Sea: depositional processes and environmental of evaporites: Israel Geological Survey Bulletin, v. 41, p. 147.

Nelson, A.N., 2000, Subsidence: Dissolution & Human Related Causes, Annu. Rev. Earth Planet. Sci., Tulane University, p. 301-336.

Newton, J.G., 1984, Review of induced sinkholes development, in Beck, B.F., ed., Sinkholes: their geology, engineering and environmental impact: Proceedings of the first multidisciplinary conference on sinkholes: Orlando, Florida, p. 3-9.

Niemi, T.M., Ben-Avraham Z., and Gat, J., 1997, Dead Sea Research - an introduction, in Niemi, T.M., Ben-Avraham Z., and Gat, J., (eds.), THE DEAD SEA the Lake and its Setting: New York, Oxford University Press, p. 3-7.

NSWU, 1999, A Glossary of GPS Terms, http://www.gmat.unsw.edu.au/snap/gps/glossary_r-z.Htm, The University of New South Wales, School of Geodetic Engineering, Australia.

Ogden, E.A., 1984, Methods for describing and predicting the occurrence of sinkholes, in Beck, B.F., ed., Sinkholes: their geology, engineering and environmental impact: Proceedings of the first multidisciplinary conference on sinkholes: Orlando, Florida, p. 177-182.

Perrodon, A., 1983, Dynamics of oil and gas accumulation: Elf Aquitaine, France.

Raz, E., 1999a, Land survey, report for work period 15/11/98-22/2/99, Dead Sea Sinkholes Project, p. 6.

Raz, E., 1999b, A study about the formation of sinkholes along the Dead Sea shores, summation of field reports: En Gedi, Dead Sea Sinkholes Project, p. 24.

Ronen, A., 1997, Ground Penetrating Radar survey and electric conductivity measurements for detecting subsurface voids between kilometers 206-208 of Route #90, Newe Zohar, Dead Sea: Lod, The Geophys. Inst. of Isr..

Ronen, A., and Beck, A., 1997, Ground Penetrating Radar and FDEM surveys between kilometers 243-245 of Route #90, En Gedi, Dead Sea: Lod, The Geophys. Inst. of Isr..

Ronen, A., and Ezersky, M., 1997, Combined geophysical survey for studying feasibility of detecting subsurface voids and sinkholes development at the En Gedi camping site: Lod, The Geophys. Inst. of Isr..

Ronen, A., and Ezersky, M., 1998, Ground Penetrating Radar survey for detecting subsurface voids at the Novotel Hotel site, En Boqeq: Lod, The Geophys. Inst. of Isr..

Ronen, A., Rabinovich, M., and Rabinovich, B., 1992, Electromagnetic survey using the FDEM method for detecting subsurface voids at the David Hoter site, En Boqeq: Lod, The Geophys. Inst. of Isr..

Rosen, P.A., Henseley, S., Zebker, H.A., Webb, F.H., and Feilding, E., 1996, Surface deformation and coherence measurements of Kilauea Volcano, Hawaii, from SIR-C radar Interferometry: J. of Geophys. Res., v. 101, p. 23109-23125.

Rybakov, M., and Goldshmidt, V., 1999, Microgravity monitoring along highway No.90 (stage 1): Lod, The Geophys. Inst. of Isr., p. 9.

Rybakov, M., Goldshmidt, V., and Beck, A., 1999, Concealed sinkhole detection at the Dead Sea Works site using microgravity technique: Lod, The Geophys. Inst. of Isr., p. 8.

Rybakov, M., Goldshmidt, V., and Fleischer, L., 1998, The microgravity survey: A method for sinkhole detection in the Dead Sea area: Lod, The Geophys. Inst. of Isr., p. 5.

Schattner, U., Wdowinski, S., Wachs, D., and Wust-Bloch, H., 2000, GPS Geodetic monitoring of surface deformation caused by the developement of sinkholes along the Dead Sea shores, preliminary results, in Baer, G., and Avni, Y., eds., Isr. Geol. Soc. an. meet.: Ma'alot, p. 111.

Segall, P., and Davis, J.L., 1997, GPS Applications for geodynamics earthquake studies: Annu. Rev. Earth Planet. Sci., v. 25, p. 301-336.

Shtivelman, V., 1998, High-resolution seismic reflection survey in the Newe Zohar area: Lod, The Geophys. Inst. of Isr. Rep. No. 836/17/98.

Shtivelman, V., 2000a, Shallow refraction surveys in the northern part of the Dead Sea coast: Lod, The Geophys. Inst. of Isr., Rep. No. 841/94/1998 p. 4.

Shtivelman, V., 2000b, Shallow refraction surveys in the Nahal Hever area: Lod, The Geophys. Inst. of Isr. Rep. No. 841/92/1998.

Shtivelman, V., Goldman, M., Rabinovitz, M., Ronen, A., and Beck, A., 1994, Combined geophysical survey in the area of sinkhole development in the Newe Zohar region: Lod, The Geophys. Inst. of Isr..

Shtivelman, V., Goldman, M., Ronen, A., and Ezersky, M., 1999, Shallow geophysical surveys in the sinkhole development area at the Nahal Hever site: Lod, The Geophys. Inst. of Isr., Rep. No. 823/87/98, p. 15.

SNDC, 1997, Satellites, http://www.satellites.spacesim.org/english/main.html, SchoolNet Digital Collections program, Industry Canada.

Sneh, A., 1979, Late Pleistocene fan deltas along the Dead Sea Rift: Journal of Sedimentary Petrology, v. 49, p. 541-552.

Sowers, G.F., 1996, Building on sinkholes, design and construction of foundation in Karst terrain: New York, American society of civil engineers press, 208 p.

StarNine, T.a., 1996, Global Positioning System, http://hyperphysics.phy-astr.gsu. edu/hbase/gpsrec.html.

Sweeting, M.M., 1973, Karst landforms, Columbia University Press, 352 p.

Terzaghi, 1913, Principles of soil mechanics.

Terzaghi, K., 1925, Principles of soil mechanics, IV - settlement and consolidation of clay: Engineering news record, v. 95, p. 874-878.

USCG, 2000, U. S. Coastal Guard, http://www.navcen.uscg.mil/faq/gpsfaq1.htm.

USGS, 2000, Land Subsidence in the United States, USGS, p. 17.

Wachs, D., 1999, A midterm report of the Dead Sea sinkhole project, submitted to the steering Committee: Jerusalem, The Geol. Surv. of Isr., p. 16.

Wachs, D., Raz, E., and Shtivelman, V., 1999, A study of the sinkhole's formation along the Dead Sea shores, The Geol. Surv. of Isr., p. 23.

Wachs, D., Yechieli, Y., Shtivelman, V., Baer, G., Raz, E., Rybakov, M., and Schattner, U., 2000, Formation of sinkholes along the Dead Sea shores, Summary of findings from the first stage of research: Jerusalem, The Geol. Surv. of Isr., p. 52.

Wilson, W.L., 1995, Sinkhole and buried sinkhole densities and new sinkhole frequencies in Karst of northwest peninsular Florida, in Beck, B.F., ed., Proceedings of the fifth multidisciplinary conference on sinkholes and the engineering and environmental impacts of Karst: Karst Geohazards - engineering and environmental problems in Karst terrane: Galtinburg, Tennessee, p. 79-91.

Yechieli, Y., and Gat, J., 1997, Geochemical and hydrological processes in the coastal environment of the Dead Sea, in Niemi, T.M., Ben-Avraham Z., and Gat, J., (eds.), THE DEAD SEA the Lake and its Setting: New York, Oxford University Press, p. 253-264.

Yechieli, Y., and Gavrieli, I., 1999, Geohydrology of the Dead Sea area, in Shimon, I., Harlavan, Y., and Shirav, M., (eds.), Isr. Geol. Soc. an. meet.: Dead Sea.

Yechieli, Y., Gavrieli, I., Berkowitz, B., and Ronen, D., 1998, Will the Dead Sea die?: Geology, v. 26, p. 755-758.

Yechieli, Y., Magaritz, M., Levy, Y., Weber, U., Kafri, U., Woelfli, W., and Bonani, G., 1993, Late Quaternary geological history of the Dead Sea area: Israel: Quaternary Research, v. 39, p. 59-67.

Yechieli, Y., Ronen, D., Berkowitz, B., Dershowitz, W.S., and A., H., 1995, Aquifer characteristics derived from the interaction between water levels of a terminal lake (Dead Sea) and an adjacent aquifer: Water Resources Research, v. 31, p. 893-902.

תקציר

במהלך שלושים השנים האחרונות נצפו לאורך חופי ים המלח תופעות של שקיעות (subsurface subsidence) ואף התמוטטויות (sinkholes) בפני השטח. תופעות אלו קיבלו תאוצה במהלך העשור האחרון במספר ובממדים. כיום קיימים לאורך חופו המערבי של ים המלח כמה אלפי מטרים רבועים של שקיעות קרקע וכ- 600 בורות. בורות אלו מהווים סיכון לחיי אדם, פוגעים ברכוש ומונעים מימוש תוכניות לפיתוח האזור. יש הקושרים, ולו נסיבתית, את ירידת מפלס ים המלח המתמשכת להתפתחות הבורות בחופיו המערביים והמזרחיים. לפי מחקרים הנערכים עתה שקיעות מקומיות בפני השטח נגרמות מהידחסות (קומפקציה) בלתי הפיכה של המארג התת-קרקעי, בעוד התמוטטות פני השטח ליצירת בור נגרמת עקב המצאות חלל תת-קרקעי הנוצר עקב המסת מלח. אופי העיוות בפני השטח משקף בחלקו את התכונות המכאניות של הקרקע בה הוא נוצר (לרוב אלוביום). עם זאת עדיין קיים קושי לחזות מיקום של בור חדש ולהעריך את קצב התפתחותו.

מחקר זה נערך בשני בשני רמות – אזורית, לאורך חופו מערבי של ים המלח (בין נחל צרויה לנחל צאלים) , ומקומית, בצפון מניפת הסחף של נחל חבר. מטרת המחקר העיקרית היתה ניטור ואפיון כמותי של המעוות האנכי בפני השטח המלווה את התפתחות הבורות, על ידי שימוש בשלוש שיטות גיאודטיות: Global Positioning System (GPS), Interferometric synthetic aperture radar (InSAR), Electronic Distance Measurement (EDM). מטרה נוספת של המחקר היתה לפתח שיטה למעקב אחרי העיוותים בפני השטח שתשלב בין שלוש השיטות הגיאודטיות הנ״ל, שתהווה כלי למחקרים עתידיים. בעזרת שיטת ה- GPS נמדד מיקום של נקודות בפני השטח בדיוק גבוה. רוב המדידות המקומיות נערכו בעזרת GPS קינמטי משני סוגים: Real Time Kinematics (RTK), ו- Post process. המידע הנרכש על-ידי מערכות אלו הוא מיקום 4 ממדי של נקודות יחסית לרשת הייחוס העולמית. שתי שיטות אלו מנפקות מיקום בדיוק של סנטימטר ברכיבים האופקים, ושלושה ברכיב האנכי. מכל סידרת מדידות גיאודטיות הופקה מפת גבהים של שטח המיפוי, ונעשה מעקב אחר שינויים אנכיים בפני השטח. שיטת ה-InSAR שימשה למדידת שינויים טופוגרפיים על פני שטחים נרחבים. במהלך עיבוד הנתונים נסרקו 17 הדמיות לוויין מהשנים 1992-1999, במרווחי זמן של 2 עד 71 חודשים בין ההדמיות, על מנת לאפיין את השקיעות בפני שטח המיפוי ברמה האזורית. מכשיר ה- EDM מודד מרחקי נקודות ביחס אליו (אופקי, אנכי וזוויות). מדידות ה-EDM שימשו כשיטה משלימה למדידות ה-GPS ברמה המקומית, ולכן לתוצאות ה-EDM יש תרומה מועטה למחקר.

תוצאות המדידות של שלוש השיטות הגיאודטיות הנ״ל, ובנוסף סריקת תצלומי אוויר ותצפיות שטח, מאפשרות לנו לאפיין את העיוות בפני השטח ברמה המקומית וברמה האזורית. ברמה המקומית - במהלך שנתיים של מדידות שטח (GPS, EDM) בצפון מניפת הסחף של נחל חבר, חלק מהבורות אשר בשטח המיפוי גדלו ומספרם עלה מארבעה לשבעה. כמו כן, התפתחו שקיעות קרקע בפני השטח ובהן מערכות סידוק קונצנטריות סביב הבורות. ברמה האזורית - בהדמיות לוויין (InSAR) זוהו שקיעות קרקע נוספות, בשטח שבין נחל צרויה לנחל צאלים, בחפיפה חלקית למיקום אתרי בורות. שקיעות אלו פרוסות על שטח נרחב (מאות מטרים רבועים) ומתפתחות בקצב של עד 4 סנטימטרים בשנה.

ניטור גיאודטי של עיוותים בפני השטח לאורך חופי ים המלח המערביים באמצעות תצפיות GPS ו- InSAR

אורי שטנר